

A Prestress Based Approach to Rotor Whirl

A Thesis
Submitted for the Degree of
Doctor of Philosophy
in the Faculty of Engineering

By
M. Pradeep



Department of Mechanical Engineering
Indian Institute of Science
Bangalore - 560 012
India

September 2008

Dedicated to

My Parents

Abstract

Rotordynamics is an important area in mechanical engineering. Many machines contain rotating parts. It is well known that rotating components can develop large amplitude lateral vibrations near certain speeds called critical speeds. This large amplitude vibration is called rotor whirl. This thesis is about rotor whirl.

Conventional treatments in rotordynamics use what are called gyroscopic terms and treat the rotor as a one-dimensional structure (Euler-Bernoulli or Timoshenko) with or without rigid masses added to them. Gyroscopic terms are macroscopic inertial terms that arise due to tilting of spinning cross-sections. This approach, while applicable to a large class of industrially important rotors, is not applicable to a general rotor geometry.

In this thesis we develop a genuine continuum level three dimensional formulation for rotordynamics that can be used for many arbitrarily shaped rotors. The key insight that guides our formulation is that gyroscopic terms are macroscopic manifestations of the prestress induced due to spin of the rotor. Using this insight, we develop two modal projection techniques for calculating the critical speed of arbitrarily shaped rotors. These techniques along with our prestress based formulation are the primary contributions of the thesis. In addition, we also present two different nonlinear finite element based implementations of our formulation. One is a laborious load-stepping based calculation performed using ANSYS (a commercially available finite element package). The other uses our nonlinear finite element code. The latter two techniques are primarily developed to provide us with

an accurate answer for comparison with the results obtained using the modal projection methods.

Having developed our formulation and the subsequent modal projection approximations, we proceed to validation. First, we analytically study several examples whose solutions can be easily obtained using routine methods. Second, we consider the problem of a rotating cylinder under axial loads. We use a semi-analytical approach for this problem and offer some insights into the role played by the chosen kinematics for our virtual work calculations. The excellent match with known results obtained using Timoshenko theory validates the accuracy of our formulation. Third, we consider several rotors of arbitrary shape in numerical examples and show that our modal projection methods accurately estimate the critical speeds of these rotors.

After validation, we consider efficiency. For axisymmetric rotor geometries, we implement our formulation using harmonic elements. This reduces the dimension of our problem from three to two and considerable savings in time are obtained.

Finally, we apply our formulation to describe asynchronous whirl and internal viscous damping phenomena in rotors.

Acknowledgements

Mata, Pita, Guru and *Deva* goes the descending order of importance in our tradition. The role of *Guru* in the life of a person cannot be overemphasised. It has been a privilege to work under a *Guru* like Prof. Anindya Chatterjee. This thesis is an outcome of his constant motivation, guidance and deep insights. I thank my *Guru* for everything he has given me.

I next thank my teacher Prof. C. S. Jog for helping me with the nonlinear finite element formulation presented in this thesis and for lending me his code for my use.

I thank my friends from Dynamics lab. I have enjoyed their company and learnt a lot about life from them. I thank Amol, Nandakumar, Pankaj, Pradipta, Satwinder, Umesh, Vamshidhar, Navendu, Arjun, Dhananjay, Prateek, Rahul, Venkatesh, Anup, Rambabu and Ishita. I also thank Sandeep Goyal whose ME work gave me the direction for my PhD thesis.

I also thank my friends Abhijit, Arun, Ashok, Guptaaji, Krishnan, Nishikant, Premkumar, Ramkumar, Sachin, Sai and Venkatesh for all their help. Special thanks to my friends Manthram and Sandhya for all their encouragement and motivation. I also thank my friends Chandan and Arun Kumar for all their help.

I am indebted to my parents for their support and sacrifice without which I could have never pursued my PhD. It is because of my *Mata* and *Pita* that I met my *Guru*. I

thank *Deva* for making all this happen.

Contents

Abstract	i
Acknowledgements	iii
List of Figures	xi
List of Tables	xv
1 Introduction and literature survey	1
1.1 A brief account of the rotor literature	1
1.2 Some rotordynamics phenomena	3
1.2.1 Synchronous whirl	3
1.2.2 Campbell diagram	4
1.2.3 Gyroscopic terms	5
1.3 Contributions of this thesis	6
2 Laborious load-stepping	8

2.1	Load-stepping method using ANSYS	8
2.2	Results for two other geometries	10
2.2.1	A truncated cone	11
2.2.2	A bottle	11
2.3	Scope of the load-stepping calculation	12
3	An incorrect but instructive modal projection	14
3.1	Dynamic equilibrium	15
3.2	Virtual work	16
4	A new prestress based formulation	19
4.1	Why explicit gyroscopic terms are not needed	19
4.2	Simplifying insights	20
4.3	The prestress based formulation	21
5	Modal projection methods for our formulation	23
5.1	Modal projection method 1	24
5.2	Multi-mode projections (method 1)	25
5.3	Modal projection method 2	26
5.4	Comparisons with other formulations	27
5.4.1	Comparison with Nandi and Neogy's method	27
5.4.2	Comparison with Stephenson and Rouch	29
5.5	Concluding remarks	30

6	Analytical examples	31
6.1	Some classical buckling problems	32
6.1.1	The basic equation of Euler-Bernoulli buckling	32
6.1.2	Columns with Other Loading	35
6.1.2.1	A simply supported column under axial load and with elastic lateral support	36
6.1.2.2	A simply supported column under axial load and self weight	36
6.1.3	Buckling of a Ring	38
6.2	Ewins's rotor	41
6.2.1	Ewins's solution (including explicit gyroscopic terms)	42
6.2.2	Our formulation (no explicit gyroscopic terms)	43
6.2.2.1	Calculation of critical speed	44
6.2.2.2	Equations of motion at a general speed	45
6.3	Beam plus rigid body models	48
6.4	A spinning torque free cylinder	53
6.4.1	Governing equations	53
6.4.2	Torque free cylinder: prestress based formulation	54
6.5	Foreshortening	56
6.6	Concluding remarks	60
7	Axially loaded cylindrical rotors	61
7.1	Nominal Timoshenko kinematics: no warping	62

7.2	Kinematics from a 3D elasticity solution	63
7.2.1	Cylinder under a transverse end load	63
7.2.2	3D kinematics for ϕ	63
7.2.3	Connection with Cowper's shear factor K	65
7.3	Results for lateral vibrations and buckling	65
7.3.1	Lateral vibrations	66
7.3.2	Buckling load of a simply supported cylinder	68
7.4	Critical speed of a simply supported, axially loaded, cylinder	69
7.5	Concluding remarks	70
8	Numerical examples	73
8.1	Results for axisymmetric geometries	73
8.2	An asymmetric rotor example	78
8.3	Concluding remarks	79
9	Nonlinear finite element calculation	80
9.1	Isoparametric nonlinear finite element solution	80
9.2	Concluding remarks	86
10	Harmonic elements	87
10.1	Introduction	87
10.2	General formulation	88
10.3	Axisymmetric harmonic elements	88

10.4 Analytical integration with respect to θ in the volume integrals	90
10.4.1 $\int_V \mathbf{S}_0 : \nabla \phi^T \nabla \phi dV$	90
10.4.2 $\int_V \rho \phi \cdot \phi dV$	91
10.4.3 $\int_V \rho (\hat{\mathbf{n}} \times \hat{\mathbf{n}} \times \phi) \cdot \phi dV$	92
10.5 Results	92
10.6 Concluding remarks	93
11 Asynchronous whirl	96
11.1 Modal projections	96
11.2 Axisymmetric rotor example	100
11.3 A non-axisymmetric rotor example	105
11.4 Concluding remarks	110
12 Internal viscous damping	111
12.1 Formulation	111
12.2 Results for a cylindrical rotor	113
13 Conclusions	115
A Direct nonlinear finite element analysis	118
B Some relevant formulae	122
B.1 Grad and Div in Cylindrical Coordinates	122
B.2 The Function g in Eq. (6.10)	122

C Numerical integration in MATLAB	124
D Circular motion of non-axisymmetric rotors	128
References	131

List of Figures

1.1	Three rotor geometries.	2
1.2	Synchronous (forward) whirl and backward whirl (adapted from [1]).	4
1.3	A typical Campbell diagram.	4
1.4	Gyroscopic moments arise due to tilting of spinning cross-sections.	5
1.5	Three possible discretizations of rotor.	6
2.1	Central displacement vs. spinning speed of a perfect and imperfect rotor.	9
2.2	Left: mesh. Right: fundamental lateral vibration mode.	9
2.3	Left: central displacement a vs. speed ω . Right: slope $da/d\omega$ vs. ω	10
2.4	Mesh of the truncated cone.	11
2.5	Left: central displacement a vs. speed ω . Right: slope $da/d\omega$ vs. ω	12
2.6	Mesh of the bottle geometry.	12
2.7	Left: central displacement a vs. speed ω . Right: slope $da/d\omega$ vs. ω	13

3.1	A heavy disk rigidly attached to a massless shaft and supported by two springs at the end. The shaft and disk system spins at a speed of Ω . The unloaded end of the shaft is constrained in a ball and socket joint.	17
6.1	Buckling of columns: Case (a) pinned-pinned (b) fixed-fixed.	32
6.2	(a) Buckling of a pinned-pinned column with lateral elastic support. (b) Buckling of a pinned-pinned column under its own weight.	35
6.3	A uniformly loaded thin ring.	38
6.4	Force and displacement.	39
6.5	A heavy disk rigidly attached to a massless shaft and supported by two springs at the end. The shaft and disk system spins at a speed of Ω . The unloaded end of the shaft is constrained in a ball and socket joint.	42
6.6	Lateral vibration mode of the system.	44
6.7	Beam cylinder model.	48
6.8	Spinning cylinder.	53
6.9	A rotating cantilever beam.	56
7.1	A solid circular rotor under axial load.	62
7.2	Nominal kinematics of a Timoshenko beam.	62
7.3	Nondimensionalized natural frequency ($\omega_n/\bar{\Omega}$) of a simply supported cylinder, plotted against L/D . Here $\bar{\Omega} = 2\pi\sqrt{ER^2/\rho L^4}$. For Timoshenko theory, we used $K = (6 + 6\nu)/(7 + 6\nu)$ [2]. For numerical calculation, we used $R = 0.25$ m, $E = 210$ GPa, $\nu = 0.25$ and $\rho = 7800$ Kg/m ³	67
7.4	Nondimensionalized buckling load P/P_e of a cylinder plotted against L/D . Here $P_e = \frac{\pi^2 EI}{L^2}$. For Timoshenko theory we used $K = (6 + 6\nu)/(7 + 6\nu)$. For numerical calculations we used $R = 0.25$ m, $E = 210$ GPa, $\nu = 0.25$ and $\rho = 7800$ Kg/m ³	69

7.5	Nondimensionalized critical speed ($\Omega_c/\bar{\Omega}$) of a simply supported cylinder plotted against L/D . The axial load applied is $P = 0.7\frac{\pi^2 EI}{L^2}$ in each case. $\bar{\Omega} = 2\pi\sqrt{ER^2/\rho L^4}$. $K = (6 + 6\nu)/(7 + 6\nu)$. For numerical calculations we used $R = 0.25$ m, $E = 210$ GPa, $\nu = 0.25$ and $\rho = 7800$ Kg/m ³	71
8.1	Rotor geometries considered.	74
8.2	Meshes for beam-rigid-body models (10 noded tetrahedral elements). . . .	76
8.3	Left: mesh of the scalene triangular cylinder. Right: first mode shape. . . .	78
9.1	Zoomed plot of reciprocal of condition number (MATLAB's RCOND) against speed for the cylinder geometry of chapter 8.	85
10.1	Rotor geometries considered.	93
11.1	The frame $X'-Y'$ rotates about the bearing centerline at the rate Ω . A typical point on the centerline of the shaft moves along an arbitrary curve.	97
11.2	Ewins's rotor with asymmetric springs on supports that rotate with the disc.	99
11.3	Campbell diagram of the cylindrical rotor. The eigenvalue plotted is $\lambda + i\Omega$ which is purely imaginary at all speeds for this rotor geometry. Note that the horizontal and vertical scales are unequal.	101
11.4	Orbital paths of a point on the axis of the cylinder for $\Omega = 900$ rad/s. There are four eigenvalues ($\lambda = \pm 626.18i$ and $\lambda = \pm 2370.17i$) describing the motion in the rotating coordinate system. Figures (a), (c) and (e) are the paths seen in the rotating frame while (b), (d) and (f) correspond to those in the inertial frame. Displacements are arbitrarily scaled.	104
11.5	The mesh of the non-axisymmetric rotor geometry considered.	105
11.6	Real part of the instability causing eigenvalue λ as a function of spin speed. The region where this is positive is the instability region. The edges of the instability region are the synchronous whirl speeds.	106

11.7	Orbital path of a point on the axis of the rotor for $\Omega = 300$ rad/s. There are four eigenvalues ($\lambda = \pm 202.80 i$ and $\lambda = \pm 1768.51 i$) describing the motion in the rotating coordinate system. Figures (a), (c) and (e) are the paths seen in the rotating frame while (b), (d) and (f) correspond to those in the inertial frame. Displacements are arbitrarily scaled.	108
11.8	Variation of imaginary part of λ_1 with shaft spin speed Ω	109
11.9	Periodic orbits in the inertial frame. Black dot indicates the bearing centerline.	110
12.1	Left: plot of imaginary part of λ against spin speed Ω . Right: plot of real part of λ against spin speed Ω	114
A.1	Zoomed plot of reciprocal of condition number (RCOND) against speed.	121
C.1	Ten noded tetrahedral element. ξ_1 , ξ_2 , ξ_3 and ξ_4 are the local volume coordinates.	124

List of Tables

8.1 Comparison of critical speeds from various methods. All speeds in rad/s. Note that the difference between bending and whirling frequencies is relatively small (e.g., about 3% for the cylinder). Nevertheless, this small *difference* is captured to within about 4%. 75

8.2 Comparison of critical speeds from various methods. All speeds in rad/s. Modal projections performed with two modes. The geometric properties of the rotor (mass moment of inertia matrix, center of mass), required for the analytical evaluation of the critical speed using the method discussed in section 6.3, were obtained using ANSYS. 77

8.3 Triangular cross-sectioned rotor: comparison of critical speeds obtained using different methods. All speeds in rad/s. 79

10.1 Comparison of critical speeds from various methods. All speeds and frequencies in rad/s. Note that the difference between bending and whirling frequencies is relatively small (e.g., about 3% for the cylinder). Nevertheless, this small *difference* is captured to within about 1.4%. 94

10.2 Comparison of critical speeds from various methods. All speeds and frequencies in rad/s. Modal projections performed with two modes. The imaginary values represent conceivable whirling motions that are actually suppressed by gyroscopic terms. 94

C.1 Gauss points and weights. 126

Chapter 1

Introduction and literature survey

Rotordynamics is an important area in mechanical engineering. Many machines contain rotating parts. It is well known that rotating components develop large amplitude lateral vibrations near certain speeds called critical speeds. This large amplitude vibration is called rotor whirl. This thesis is about rotor whirl. Most of the thesis will deal with synchronous whirl, but towards the end we will consider asynchronous whirl as well.

1.1 A brief account of the rotor literature

The rotordynamics literature is vast. A good summary of early rotordynamics history is given in [3] and a good account of the development in modeling procedures is given in [4].

To motivate this thesis, we consider three possible scenarios in rotordynamics analysis. In the first case, the rotor geometry consists of several heavy, nearly rigid discs attached to slender shafts, as shown in figure 1.1 (a). In this case one can get very good results by treating the shaft as a slender beam (Euler-Bernoulli or Timoshenko) without considering its mass (or considering its mass in any reasonable approximate sense) and by treating the discs as rigid masses attached to the shafts. Many standard techniques in rotordynamics like the transfer matrix method (developed by Prohl [5]; used for rotordynamics analysis in, e.g., Flack and Rooke [6], Sakate *et al.* [7] and Hsieh *et al.* [8]) or the finite element method using beam elements can then be used to describe the dynamics of the rotor. Several pa-

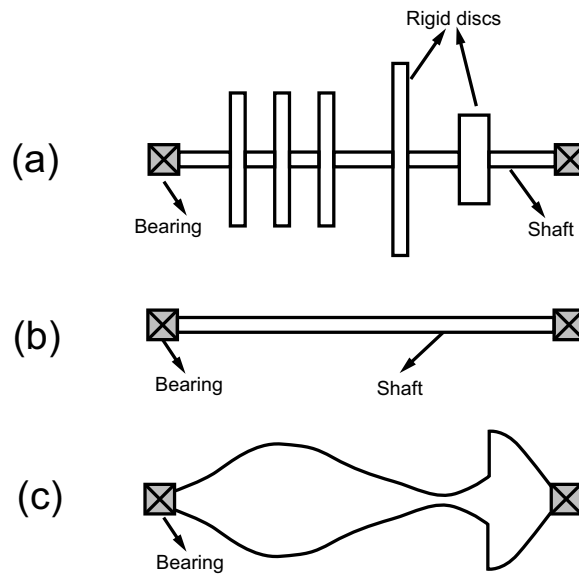


Figure 1.1: Three rotor geometries.

pers on rotors have concentrated on finite beam elements of various kinds (e.g., conical or tapered). These include Rouch and Kao [9], Nelson [10], Greenhill *et al.* [11], Genta [12, 13], Edney *et al.* [14] and Gmür and Rodrigues [15].

In the second case, figure 1.1 (b), the mass of the shaft is no longer negligible. The mass and gyroscopic effects of each cross section need to be taken into account. Timoshenko theory is good for this case [16].

In the final case, figure 1.1 (c), the rotor geometry is complicated and the usual approximations of beam theory and treatment of the shaft as massless are no longer appropriate. We need a genuine three dimensional treatment of the rotor. Very few papers in the literature consider genuine three dimensional treatment of rotors. Among them, Stephenson and Rouch [17] use harmonic elements to analyse arbitrary axisymmetric rotors. Their approach, while applicable to any axisymmetric rotor, is based upon separately deriving and adding a gyroscopic matrix to the usual modal analysis.

However, to write equations at the continuum level, one must abandon the gyroscopic term based approach (as will be discussed in detail later) and look for alternatives. One such alternate approach is presented by Nandi and Neogy [18]. They present a gen-

uine three dimensional approach for analysis of rotors whose cross sections have two axes of symmetry. However, their method is not derived from continuum level equations. Rather, a crucial step in their method is an *ad hoc* addition of an inertia term. Thus, even though their method goes one step beyond the usual analysis, it is not derived from a continuum formulation.

While presently available rotordynamics analyses are capable of handling most common rotor geometries, there is still the need for a method based on genuine three dimensional continuum level treatment of rotors. It is this need that we address in this thesis.

We develop a new prestress based formulation for analysing rotors of arbitrary shape. Our formulation is different from conventional treatments in that we do not use any explicit gyroscopic term. Instead, we begin with continuum level equations, account for the spin-induced prestress, and implicitly capture all the gyroscopic effects. Our formulation applies to rotors of non-axisymmetric shape and we will consider one such case in chapter 8. However, most of our other examples will be axisymmetric for simplicity and greatest relevance.

1.2 Some rotordynamics phenomena

1.2.1 Synchronous whirl

In this thesis we will mostly deal with synchronous forward whirl which is a special motion at a special speed. Viewed in a rotating coordinate system that spins about the undeformed axis at that special speed, synchronous forward whirl gives a static, bent configuration. Figure 1.2 illustrates the synchronous forward and backward whirling motion. In engineering practice, the synchronous forward whirl speed is usually the most important among the rotor's critical speeds.

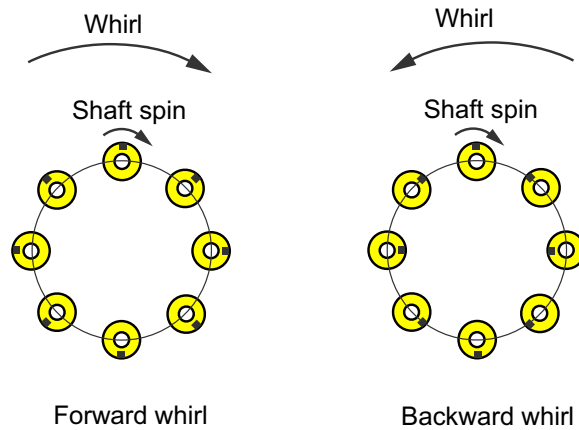


Figure 1.2: Synchronous (forward) whirl and backward whirl (adapted from [1]).

1.2.2 Campbell diagram

An important way to look at rotordynamics is through the Campbell diagram illustrated in figure 1.3 [16]. This is a plot of variation of the natural frequency of the rotor as a function of the spin speed. The natural frequency is, for many rotors, a slowly increasing function of the spin speed. The critical speed is defined as that speed of rotation at which

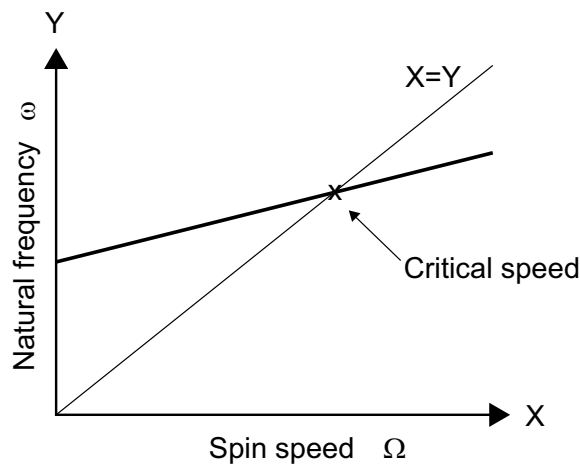


Figure 1.3: A typical Campbell diagram.

the natural frequency of the rotor is numerically equal to the spin speed. This point is

located by drawing a line at 45 degrees, as shown in figure 1.3, and the intersection point is the critical speed. At this speed any disturbance through unbalance gets excited at the natural frequency and causes large amplitude motions or whirling.

1.2.3 Gyroscopic terms

Gyroscopic terms arise due to tilting of spinning cross-sections. Conventional methods in rotordynamics incorporate gyroscopic moments (i.e., terms of the form $\boldsymbol{\Omega} \times \mathbf{I} \cdot \boldsymbol{\Omega}$), which are macroscopic *inertial* terms (disk-elementwise or ring-elementwise as opposed to continuum pointwise).

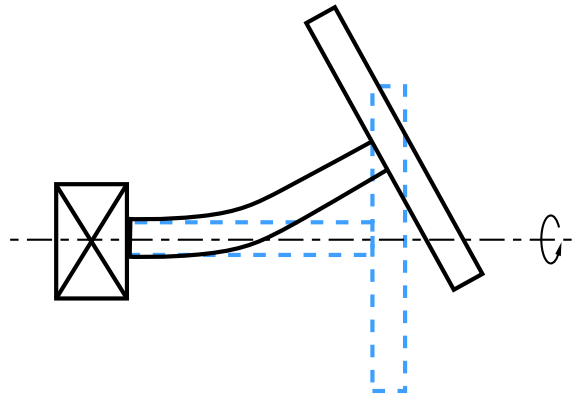


Figure 1.4: Gyroscopic moments arise due to tilting of spinning cross-sections.

However, a continuum element level treatment cannot incorporate gyroscopic terms since these are macroscopic effects. Figure 1.5 shows three different rotor elements; a disc, a ring and an infinitesimal cuboidal element. We will compare the order of magnitude of inertia and gyroscopic terms for each of these elements. The net inertia force is of the order of $\approx \int_V \rho \mathbf{a} dV = \int_V \mathbf{a} dm = m_{tot} \mathbf{a}$ in all cases, where \mathbf{a} is the acceleration. The gyroscopic terms are of the form $\boldsymbol{\Omega} \times \mathbf{I} \cdot \boldsymbol{\Omega}$ and their magnitude is of the order of $\Omega^2 \|\mathbf{I}_{cm}\|$. For disc and ring elements this term is proportional to $\int_V r^2 dm \propto m_{tot} r^2$. However, for the infinitesimal element, this term becomes $\int_V |\Delta x|^2 dm \rightarrow 0$ as the element size goes to zero, i.e., the gyroscopic terms vanish at the continuum level.

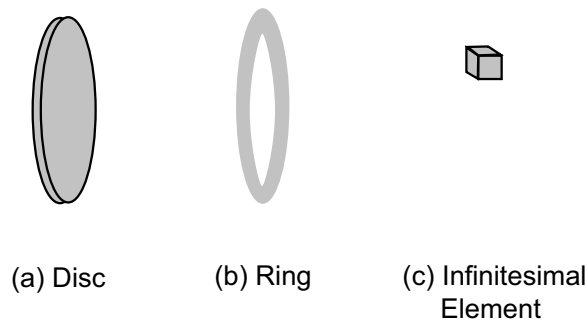


Figure 1.5: Three possible discretizations of rotor.

The question then is, what is the continuum level equivalent of the macroscopic gyroscopic terms? The answer to this question is the key insight that motivates this thesis: commonly used macroscopic gyroscopic terms arise due to the effect of the spin-induced *prestress* at the continuum level in the rotor. We will show that by incorporating the effect of this prestress at the continuum level we can obtain the correct equations of motion governing the rotor.

1.3 Contributions of this thesis

In this thesis we develop a new prestress based formulation for describing rotor whirl. Our formulation, developed from a continuum level, offers a genuine three dimensional treatment of rotors. This three dimensional formulation can be directly implemented using finite elements; but can also be implemented more simply using modal projections. Here, we do both. The direct finite element implementation of the formulation is done using a commercially available finite element package (ANSYS) as described in chapter 2 as well as with our own nonlinear finite element code (described in chapter 9 using isoparametric elements and in appendix A using hybrid elements). However, these laborious methods, perhaps novel in rotor applications, are developed merely to provide accurate answers for comparison for arbitrarily shaped rotor geometries.

Our main contribution in this thesis is our formulation, developed in chapter 4, and its implementation using modal projections, described in chapter 5. We develop two modal

projection techniques for finding the forward synchronous whirl speed of arbitrarily shaped rotors. The validity of these methods is established with a number of analytical (chapters 6,7) and numerical (chapter 8) examples.

Having established methods for computing critical speeds of arbitrary rotors, we consider ways of exploiting symmetry. For axisymmetric rotors, we apply our formulation with harmonic elements in chapter 10. These essentially two dimensional elements are capable of describing deformation of an axisymmetric structure under non-axisymmetric loading. With these elements our formulation, applied to arbitrary axisymmetric rotors, reduces to two dimensions with significant savings in computational effort.

Although much of the thesis focuses on finding the synchronous whirl speed, we consider asynchronous whirl in chapter 11. Finally, we consider the effects of internal viscous damping in chapter 12.

It is mentioned here that the work presented in chapter 3, 4, 5, 6 and 8 has already been published in *Proceedings of the Royal Society A* [19]. The buckling calculations in chapter 7 have been presented in NaCoMM 2007 [20]. The problem of axially loaded cylindrical rotor, presented in chapter 7 using three dimensional elasticity solution based kinematics has been submitted to a journal.

Chapter 2

Laborious load-stepping

Before we move to the main contribution of the thesis, we present a simpler but more laborious calculation in rotordynamics. The primary goal of this thesis is to develop a three dimensional continuum level method for calculating the critical speeds of arbitrary rotors. For simple rotor geometries, the validity of our approach can be checked against analytical formulas; for complex rotor geometries, where an analytical solution is not available, we need alternative methods to provide reliable answers for comparison. To this end, we now present a load-stepping based method for computing the critical speed using ANSYS. This method in itself is perhaps new in rotor applications in that we have not seen it reported elsewhere. However, it is laborious and computationally expensive and is presented only for cross checking the results obtained using our main method.

2.1 Load-stepping method using ANSYS

ANSYS can compute geometrically nonlinear static solutions for objects in steadily rotating frames of reference. Analysing a perfect rotor in this way gives only the radial expansions associated with the centrifugal loading. However, on putting a small imperfection in the rotor, the whirling speed can be estimated indirectly. The idea is illustrated in figure 2.1. The imperfection destroys the bifurcation, and there may be other solutions as well; but these issues are not relevant here. Note that continuum equations of nonlinear elastodynamics are solved directly by ANSYS; there is no need for explicitly and separately incorporating

gyroscopic effects.

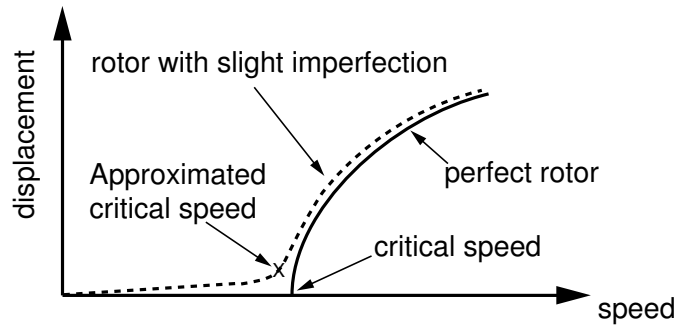


Figure 2.1: Central displacement vs. spinning speed of a perfect and imperfect rotor.

We illustrate the procedure for a cylinder (length 2 m, radius 0.25 m). The material properties for all geometries considered here are Young's modulus $E = 210$ Gpa, Poisson's ratio $\nu = 0.25$ and density $\rho = 7800$ kg/m³. The actual analysis proceeds as follows. The rotor is meshed, at an adequate level of refinement, using 10 noded tetrahedral elements as shown in figure 2.2. A simple support condition is approximately enforced by constraining all nodes on either endface to have axial displacements only; and furthermore constraining axial motions of the central node of the rotor.

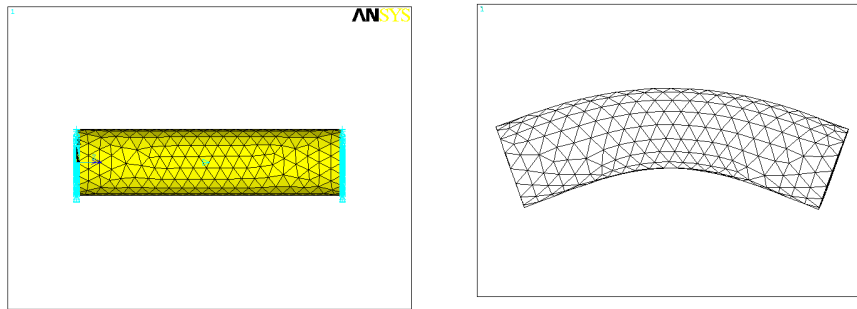


Figure 2.2: Left: mesh. Right: fundamental lateral vibration mode.

Routine modal analysis gives the fundamental mode shape ϕ (see figure 2.2, right) and the natural frequency $\omega_f = 1498.7$ rad/s.

Next, each node in the mesh is displaced by some small number b times the vector

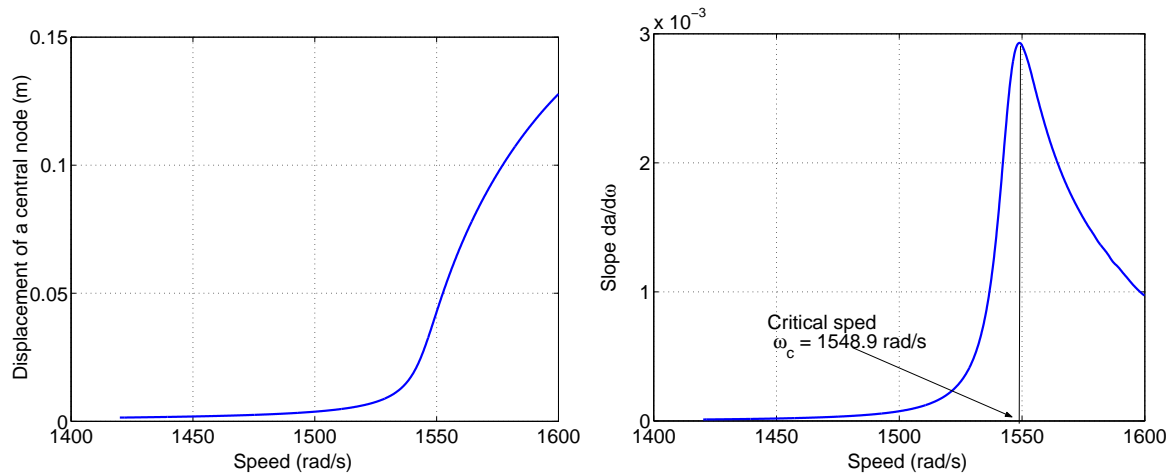


Figure 2.3: Left: central displacement a vs. speed ω . Right: slope $da/d\omega$ vs. ω .

value of the mass-normalized mode shape at that node (we arbitrarily used $b = 0.03$). The new mesh represents a slightly bent, or imperfect, rotor.

To this new finite element model we apply an inertial loading corresponding to a spin speed of $\omega = 1420$ rad/s (sufficiently low, but otherwise arbitrary). The statics problem is solved with full nonlinear options in ANSYS. Using the results as an initial guess, we then obtain the solution at a slightly higher speed ω (using the “restart” option in ANSYS). In this way, we proceed until $\omega = 1600$ rad/s.

The displacement a of a surface node near the midplane of the rotor is plotted against ω in figure 2.3 (left). In the absence of imperfection, the upward bend in the curve would be a kink. With this thought, the speed at which the slope $da/d\omega$ is greatest is taken as the critical speed ω_c of the shaft, giving $\omega_c = 1548.9$ rad/s. The slope is numerically estimated via cubic spline interpolation of the displacements.

2.2 Results for two other geometries

We now present results for two other geometries analysed with the above method. These geometries will be considered again later and the results obtained below will be used for

comparison.

2.2.1 A truncated cone

The cone considered is 2 m long with the radius varying from 0.5 m at one end to 0.2 m at the other end. Ten noded tetrahedral elements are again used for the mesh (see figure 2.4). A simple support condition is approximately enforced by constraining all nodes on either endface to have axial displacements only; and furthermore constraining axial motions of a node on the left face of the rotor. The critical speed is calculated as described above.

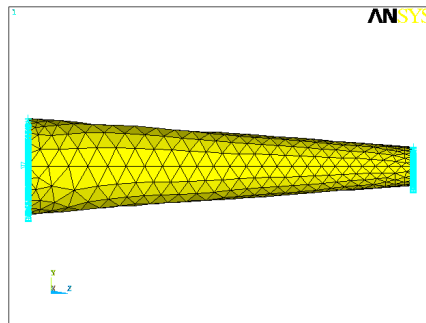


Figure 2.4: Mesh of the truncated cone.

The fundamental frequency of lateral vibration of the cone is $\omega_f = 969.13$ rad/s. For the nonlinear load-stepping calculation the speed is varied from 950 rad/s to 1030 rad/s. The results are plotted in figure 2.5. The critical speed of the truncated cone geometry is estimated as 990.7 rad/s.

2.2.2 A bottle

We now consider a bottle like geometry. The exact details of the geometry are given in chapter 8 where this rotor is considered again. Here, we just mention the results obtained using the load-stepping calculation. The mesh of the geometry is shown in figure 2.6. The end face of the neck of the bottle is constrained (held fixed) in all three directions. The

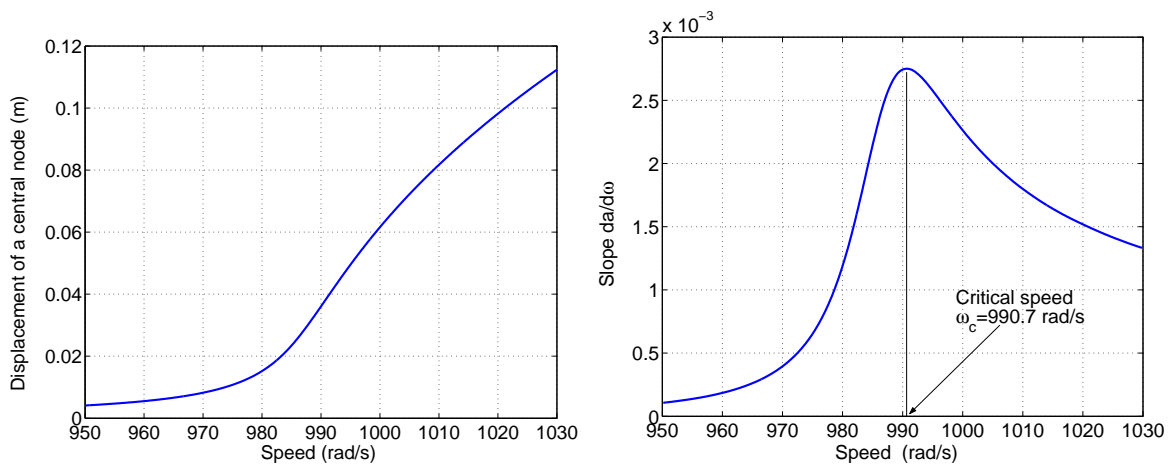


Figure 2.5: Left: central displacement a vs. speed ω . Right: slope $da/d\omega$ vs. ω .

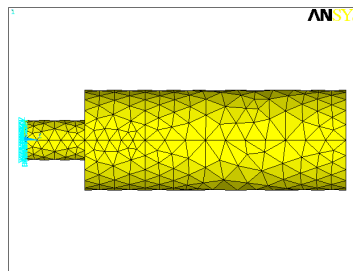


Figure 2.6: Mesh of the bottle geometry.

fundamental frequency of lateral vibration of the bottle is $\omega_f = 362.97$ rad/s. For this case, the speed for the load-stepping calculation is varied from 332 rad/s to 390 rad/s. The results are plotted in figure 2.7 where the critical speed is estimated as 381.18 rad/s.

2.3 Scope of the load-stepping calculation

The laborious load-stepping method presented in this chapter provides a way to calculate the synchronous forward whirl speed of any arbitrarily shaped rotor. However, we emphasize that this calculation is devised and described *only for cross checking* the results

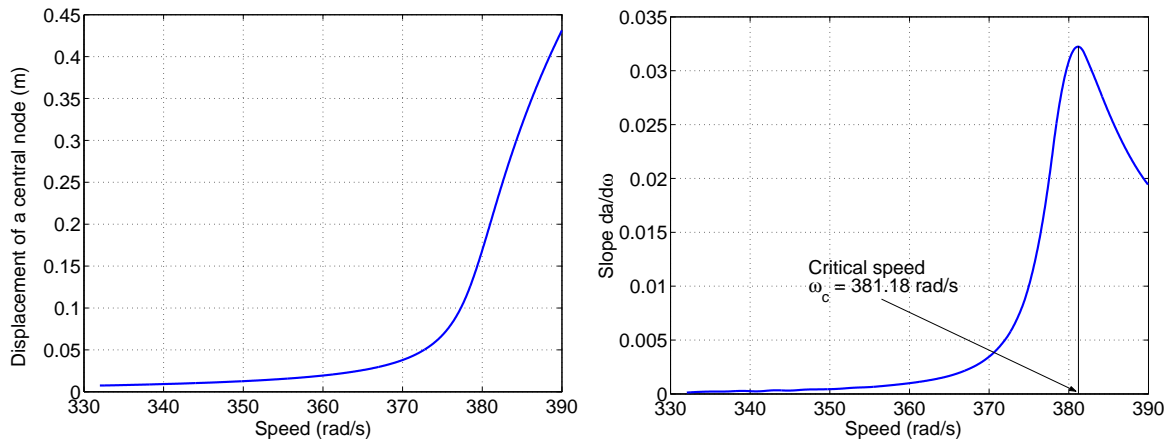


Figure 2.7: Left: central displacement a vs. speed ω . Right: slope $da/d\omega$ vs. ω .

obtained using our main method to be described in chapter 5. The load-stepping calculation is not our recommended method for finding the critical speed. Also, the load-stepping method uses a finite size imperfection and consequently the critical speeds obtained using this method only serve as a good approximation and are not an accurate estimate. A more accurate estimate using ‘proper’ nonlinear finite elasticity calculation using the finite element method were also done as a part of this work (with the help of Prof. C. S. Jog) and have been reported in our paper [19] and is also presented in appendix A. Finally, avoiding the hybrid elements of that approach we present an isoparametric element based nonlinear finite element calculation in chapter 9. The load-stepping method described in this chapter is the easiest to implement for an engineer with access to a nonlinear finite element package like ANSYS.

Chapter 3

An incorrect but instructive modal projection

Whirling is, in a sense, like buckling. In Euler buckling of columns [21], a linear eigenvalue problem is used to determine the buckling load. Nevertheless, the problem is nonlinear. The deformed and undeformed configurations are distinguished (unlike in linear elasticity); the equilibrium equation includes a term that is the product of load and displacement (equivalent to stress times strain, which would be treated as second order in linear elasticity); even past the buckling load, the unbuckled solution continues to coexist with the buckled solution (uniqueness results of linear elasticity preclude such solutions). In the same way, one can expect the whirling speed to be determined by some sort of linear eigenvalue problem. Nevertheless, we will distinguish between the whirling and non-whirling solutions; we will retain terms linear in the whirling-associated displacements but quadratic in the rotation speed (displacement times velocity squared is technically a third order term); and even past the whirling speed, the whirling and nonwhirling solutions will coexist. Papers on whirling rotors typically do not discuss this nonlinearity (a good discussion in the limited context of Timoshenko rotors is given by Choi *et al.* [22]). To clarify some aspects of this nonlinearity, we begin with a naive modal projection. Much of the discussion will carry over to the subsequent, correct, calculation.

We assume that the deformed configuration (or shape) of the shaft can be expressed as a linear combination of a few of its lateral vibration mode shapes, and illustrate the calculation by taking only one mode ϕ (the fundamental).

The key advantage of describing the deformed whirling shape in terms of vibration mode shapes is that if the displacement is given by a vibration mode shape ϕ , then it involves a stress state τ such that

$$\nabla \cdot \tau = -\rho \omega_f^2 \phi, \quad (3.1)$$

where ρ is the material density and ω_f the natural angular frequency of vibration in that mode. We will use this below, except that in place of τ we will use the second Piola-Kirchhoff stress \mathbf{S} because \mathbf{S} and τ are the same up to first order in displacements, and we will retain first order terms only.

3.1 Dynamic equilibrium

We start with the dynamic equilibrium equation in reference coordinates (see, e.g., [23], [24]),

$$\nabla \cdot (\mathbf{F}\mathbf{S}) = \rho_0 \frac{\partial^2 \chi}{\partial t^2}.$$

Here, \mathbf{F} is the deformation gradient, \mathbf{S} is the second Piola-Kirchhoff stress, ρ_0 is the undeformed density, and χ is the position vector of the material point of interest. We will project this equation on to a single mode, linearize the resulting equation, and obtain the incorrect answer that will lead to the correct method. Also note that this naive modal projection method will be used later in one of our modal projection methods, in conjunction with an ANSYS based calculation, to give the correct critical speeds.

Consider a material point initially at position vector \mathbf{X} in a rotating frame that spins at the rotor speed. The displacement of this point is taken as

$$\mathbf{u} = a\phi,$$

where a is an infinitesimal coefficient and ϕ is the mass-normalized eigenvector.

We adopt the St. Venant-Kirchhoff stress-strain relation for nonlinear calculations, although here we will linearize immediately:

$$\mathbf{S} = \lambda (\text{tr } \mathbf{E}) \mathbf{I} + 2\mu \mathbf{E},$$

where λ and μ are Lamé constants and \mathbf{E} is the Green strain tensor given by

$$\mathbf{E} = \frac{1}{2} (\nabla \mathbf{u} + \nabla \mathbf{u}^T + \nabla \mathbf{u}^T \nabla \mathbf{u}) = a \frac{1}{2} (\nabla \phi + \nabla \phi^T) + O(a^2).$$

The deformation gradient is

$$\mathbf{F} = \mathbf{I} + \nabla \mathbf{u} = \mathbf{I} + a \nabla \phi.$$

3.2 Virtual work

Considering a virtual displacement of $\delta a \phi$, we have for synchronous whirl

$$\delta a \int_V (\nabla \cdot (\mathbf{F}\mathbf{S})) \cdot \phi dV = \delta a \int_V \rho_0 (\boldsymbol{\Omega} \times \boldsymbol{\Omega} \times (\mathbf{X} + \mathbf{u})) \cdot \phi dV,$$

where V is the volume in the reference configuration and the angular velocity $\boldsymbol{\Omega}$ is directed along the undeformed centerline of the rotor.

The δa 's cancel out; we get a linear equation in a ; and nonuniqueness of the whirling solution requires the coefficient of a to be zero (in a multi-mode projection, we would look for a singular coefficient-matrix). Setting $\boldsymbol{\Omega} = \boldsymbol{\Omega}_c$ in the zero-coefficient condition, we get

$$\int_V (\nabla \cdot \mathbf{S}) \cdot \phi dV = \int_V \rho_0 (\boldsymbol{\Omega}_c \times \boldsymbol{\Omega}_c \times \phi) \cdot \phi dV. \quad (3.2)$$

The term on the left hand side, by Eq. 3.1, gives

$$\int_V (\nabla \cdot \mathbf{S}) \cdot \phi dV = -\omega_f^2 \int_V \rho_0 \phi \cdot \phi dV = -\omega_f^2,$$

because the eigenvector is mass-normalized. Substituting this in Eq. 3.2 we get

$$-\omega_f^2 = \int_V \rho_0 (\boldsymbol{\Omega}_c \times \boldsymbol{\Omega}_c \times \phi) \cdot \phi dV. \quad (3.3)$$

The predicted critical speed then is

$$\Omega_c^2 = \frac{-\omega_f^2}{\int_V \rho_0 (\hat{\mathbf{n}} \times \hat{\mathbf{n}} \times \phi) \cdot \phi dV}, \quad (3.4)$$

where the unit vector $\hat{\mathbf{n}}$ is along the undeformed rotor centerline.

In Eq. 3.4 the natural frequency ω_f and mode shape ϕ can be determined using solid elements in a commercial finite element package (we used 10 noded tetrahedral elements in ANSYS). The integral is evaluated separately in MATLAB.

It turns out Eq. 3.4 is incorrect. We will illustrate this using a simple example from Ewins [25] shown in figure 3.1. This rotor is considered in greater detail using our formulation in chapter 6. Here, we will just reproduce some results to show that our naive modal projection method is wrong.

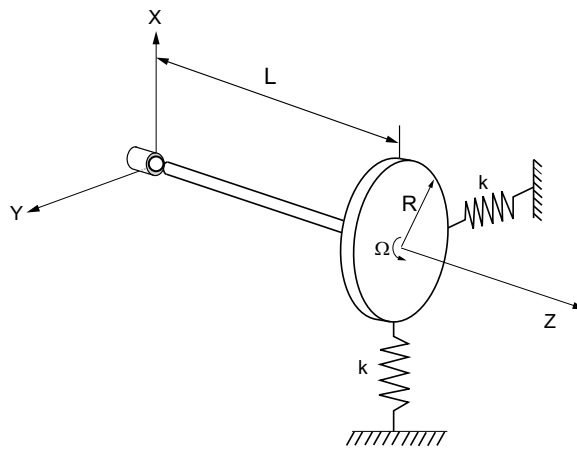


Figure 3.1: A heavy disk rigidly attached to a massless shaft and supported by two springs at the end. The shaft and disk system spins at a speed of Ω . The unloaded end of the shaft is constrained in a ball and socket joint.

The critical speed of this rotor calculated using routine methods (details in chapter 6) is

$$\Omega_c = \sqrt{\frac{k}{M(1 - R^2/4L^2)}},$$

where M is the mass of the disc. The natural frequency of the non-spinning rotor is $\omega_f = \sqrt{(kL^2/I_0)}$ ($I_0 = MR^2/4 + ML^2$, is the mass moment of inertia of the disc about the X or Y axis) and the corresponding mass normalized mode shape is

$$\phi = \begin{bmatrix} \frac{L}{\sqrt{I_0}} & 0 & -\frac{x}{\sqrt{I_0}} \end{bmatrix}^T.$$

Substituting these values into Eq. 3.4 the critical speed from our naive modal projection method is

$$\Omega_c = \sqrt{\frac{k}{M}},$$

which is wrong. The reason for this error is that we have not included a key term in our formulation. In the next chapter, we will present the correct formulation that includes this key term.

Chapter 4

A new prestress based formulation

In this chapter we derive the central formulation of this thesis. We show that, by considering the effect of prestress due to spin, the correct governing equations of motion of a rotor can be derived from the continuum level. Explicit gyroscopic terms need not be added. The spin-induced stress is the key term that was missing in chapter 3.

We mention that the main premise of this chapter is sufficiently novel and surprising to at least some members of the rotordynamics community that our paper [19] got two strongly and rigidly negative reviews and went to an adjudicator before eventual acceptance!

4.1 Why explicit gyroscopic terms are not needed

Conventional formulations of rotor dynamics use gyroscopic terms as discussed in chapter 1. A key aspect of our formulation is that it does not involve explicit incorporation of these gyroscopic terms, but still obtains correct results, as explained below.

The general governing equation for nonlinear elastodynamics of an arbitrarily moving body must remain true whether or not the body is a spinning rotor. Therefore, a correct three dimensional continuum formulation for a spinning elastic rotor must implicitly capture any and all effects of the so called gyroscopic terms commonly encountered in rotor-specific formulations. Such a continuum formulation is presented here. It will be clear that gyroscopic *effects* are duly and correctly accounted for.

4.2 Simplifying insights

We observe that Timoshenko rotor theory incorporates gyroscopic moments (i.e., terms of the form $\boldsymbol{\Omega} \times \mathbf{I} \cdot \boldsymbol{\Omega}$), which are macroscopic *inertial* terms (disk-elementwise as opposed to continuum pointwise). It is possible to model the same whirling rotor in ANSYS, and we have also modeled it using our own nonlinear finite element code. Both ANSYS (see chapter 2) and our own code, as described in our paper [19] and appendix A, however, use continuum equations and nonlinear displacement and stress terms, but not macroscopic inertial terms. Yet, all three approaches, as we shall see later, agree on results.

In our search for the bifurcation point (see discussion in chapter 2), since incipient whirling involves truly infinitesimal bending displacements, terms quadratic in them may be rigorously dropped. Moreover, terms nonlinear purely in the spin-induced displacements are likely to have a negligible physical effect, if the spin-induced geometry changes are small (at any rate, no radial expansion is considered in the Timoshenko theory). Note that this is a genuine physical approximation appropriate for the specific physical problem, although these terms are technically of order unity, i.e., finite and nonzero. Finally, terms that couple the spin-induced displacements with the bending displacements are technically of first order in infinitesimals and some of them may play a crucial role in determining the whirling speed.

The spin-induced displacements appear to be important not because they are significant compared to the physical dimensions of the rotor, but because they are associated with a significant *stress* state that is in dynamic equilibrium when the rotor is straight. On infinitesimal bending, this stress state is infinitesimally disturbed from dynamic equilibrium and plays an infinitesimal but non-negligible role in the infinitesimal bending dynamics.

Incidentally, since the divergence of the spin-induced stress field is simply a centripetal body force field (countering an inertial force), it is intuitively if not explicitly seen how the inertial-gyroscopic terms of Timoshenko rotor theory might be captured in our nonlinear displacement and stress based formulation. Moreover, for those using commercial code, the spin-induced stress field is easy to find by a single axisymmetric analysis; and the effects of this stress field can be largely incorporated by retaining it as a prestress while finding bending modes and frequencies.

These thoughts will be used to develop our formulation below.

4.3 The prestress based formulation

We start again with dynamic equilibrium in reference coordinates,

$$\nabla \cdot (\mathbf{FS}) = \rho_0 \frac{\partial^2 \boldsymbol{\chi}}{\partial t^2}. \quad (4.1)$$

As before, \mathbf{F} is the deformation gradient, \mathbf{S} is the second Piola-Kirchhoff stress, ρ_0 is the density in the undeformed configuration and $\boldsymbol{\chi}$ is the absolute displacement vector of the material point of interest.

Unlike in chapter 3 we now include spin-induced displacements (call them \mathbf{u}_0), and the displacement of a material point \mathbf{X} in the rotating frame is taken as

$$\mathbf{u} = \epsilon \mathbf{u}_0 + a \boldsymbol{\phi}, \quad (4.2)$$

where ϵ and a are bookkeeping coefficients and $\boldsymbol{\phi}$ is the displacement of the rotor due to bending.

As mentioned in chapter 3, we are interested in the coefficient matrix of terms linear in a (when that coefficient matrix is singular, infinitesimal whirling displacements are possible). This thought will guide our simplifications below.

Starting again with the St. Venant-Kirchhoff stress strain relation, the second Piola-Kirchhoff stress is written as

$$\mathbf{S} = \lambda (\text{tr } \mathbf{E}) \mathbf{I} + 2\mu \mathbf{E},$$

where λ and μ are Lamé constants and \mathbf{E} is the Green strain tensor given by

$$\mathbf{E} = \frac{1}{2} (\nabla \mathbf{u} + \nabla \mathbf{u}^T + \nabla \mathbf{u}^T \nabla \mathbf{u}).$$

However, as discussed in section 4.2, the key nonlinear physical effect that contributes to the whirling speed is that of an infinitesimal disturbance (bending) of a pre-existing significant stress state (spin-induced). This disturbance is accounted for by \mathbf{F} in

Eq. 4.1. Strain terms that are nonlinear in the displacement, in our opinion, play an insignificant role; and so \mathbf{S} in Eq. 4.1 is here approximated using linear terms only¹. Accordingly, we take $\mathbf{E} = \mathbf{E}_0 + \mathbf{E}_1$ where

$$\mathbf{E}_0 = \frac{\epsilon}{2} (\nabla \mathbf{u}_0 + \nabla \mathbf{u}_0^T), \quad \text{and} \quad \mathbf{E}_1 = \frac{a}{2} (\nabla \phi + \nabla \phi^T).$$

We can then split \mathbf{S} , the second Piola-Kirchhoff stress, into bending and spinning components. The spinning component is given by

$$\mathbf{S}_0 = \lambda (\text{tr } \mathbf{E}_0) \mathbf{I} + 2\mu \mathbf{E}_0,$$

the bending component is given by

$$\mathbf{S}_1 = \lambda (\text{tr } \mathbf{E}_1) \mathbf{I} + 2\mu \mathbf{E}_1,$$

and

$$\mathbf{S} = \mathbf{S}_0 + \mathbf{S}_1. \quad (4.3)$$

We now turn to the deformation gradient

$$\mathbf{F} = \mathbf{I} + \nabla \mathbf{u} = \mathbf{I} + \epsilon \nabla \mathbf{u}_0 + a \nabla \phi.$$

As discussed in section 4.2, the key term of interest involves the bending-induced disturbance of the spin-induced stress state \mathbf{S}_0 . This, consistent with neglect of spin-induced changes in geometry, lets us ignore \mathbf{u}_0 and write

$$\mathbf{F} = \mathbf{I} + a \nabla \phi. \quad (4.4)$$

Thus the governing equation, retaining terms only till $\mathcal{O}(a)$ and dropping the bookkeeping parameters ϵ and a , is

$$\nabla \cdot \mathbf{S}_0 + \nabla \cdot \mathbf{S}_1 + \nabla \cdot (\nabla \phi \mathbf{S}_0) = \rho_0 \frac{\partial^2 \chi}{\partial t^2}. \quad (4.5)$$

Equation 4.5 is the central formulation of the thesis. Derivation of this equation for rotor applications is novel; rotor problems have not been viewed from the angle of prestress caused by spin. However, Bolotin derives a similar equation (Eq. 1.34 pp. 46 of [26]) from a different perspective in his book on elastic stability where he considers buckling.

¹ Interestingly, the dropped strain terms nonlinear in the displacements turn out to be *identical* to terms representing the effect of spin-induced configuration changes, which we also drop in Eq. 4.4, in line with section 4.2.

Chapter 5

Modal projection methods for our formulation

In the previous chapter we described the central formulation of this thesis and derived the governing equations of a rotor at the continuum level. However, to find the critical speed of a given rotor, we need to solve the governing equations over the rotor geometry. There are several ways of achieving this. We first develop the simple method of modal projections to solve the problem. Modal projections are widely used in several approximation methods in structural mechanics. Here, the lateral vibrating mode shapes of the non-spinning rotor serve as a good approximation to the whirling configuration and reasonably accurate answers can be obtained with only a few modes (Bolotin [26] does the same for buckling problems). In this chapter, we show how the modal projection method can be used along with our formulation to solve for the critical speeds of arbitrary rotors. We will finally present two different modal projection methods. One is non-iterative and involves computing two volume integrals in addition to conducting modal analysis (e.g., in ANSYS). The other is iterative, needs computation of one volume integral along with a prestressed modal analysis (e.g., in ANSYS). We end this chapter by comparing our method with two other formulations for arbitrary axisymmetric rotors (Stephenson and Rouch [17], and Nandi and Neogy [18]).

5.1 Modal projection method 1

We begin with Eq. 4.5, reproduced below

$$\nabla \cdot \mathbf{S}_0 + \nabla \cdot \mathbf{S}_1 + \nabla \cdot (\nabla \phi \mathbf{S}_0) = \rho_0 \frac{\partial^2 \mathbf{X}}{\partial t^2}.$$

We now apply the principle of virtual work to the above equation. Considering a virtual displacement $\delta \mathbf{v} = \delta a \phi$, we have

$$\delta a \int_V (\nabla \cdot \mathbf{S}_0 + \nabla \cdot \mathbf{S}_1 + \nabla \cdot (\nabla \phi \mathbf{S}_0)) \cdot \phi dV = \delta a \int_V \rho_0 (\boldsymbol{\Omega} \times \boldsymbol{\Omega} \times (\mathbf{X} + \mathbf{u})) \cdot \phi dV,$$

where the acceleration is written, in a rotating coordinate system, for a rotor performing synchronous whirl; \mathbf{X} is the position vector of the point in the reference configuration and \mathbf{u} is its displacement given by Eq. 4.2. The δa 's cancel out; and retaining terms only linear in a we get our modal projection

$$\underbrace{\int_V (\nabla \cdot (\nabla \phi \mathbf{S}_0)) \cdot \phi dV}_A + \underbrace{\int_V (\nabla \cdot \mathbf{S}_1) \cdot \phi dV}_B = \Omega_c^2 \int_V \rho_0 (\hat{\mathbf{n}} \times \hat{\mathbf{n}} \times \phi) \cdot \phi dV, \quad (5.1)$$

where Ω_c is the critical speed and $\hat{\mathbf{n}}$ is along the undeformed rotor axis.

Term B in Eq. 5.1, by Eq. 3.1, is known in terms of the natural frequency of vibration, as in chapter 3:

$$B = \int_V (\nabla \cdot \mathbf{S}_1) \cdot \phi dV = -\omega_f^2 \int_V \rho_0 \phi \cdot \phi dV = -\omega_f^2.$$

Finally, we consider term A in Eq. 5.1. This term, consistent with the qualitative discussion of section 4.2, constitutes the only difference between Eq. 5.1 and the incorrect prediction of Eq. 3.4.

Term A involves derivatives of second order, and so direct evaluation would be possible if we used finite elements of sufficiently high order shape functions (e.g., 20 noded brick). Here, we transform the term for easier evaluation. For any second order tensor field \mathbf{T} , and any vector field \mathbf{v} , we have the identity

$$\nabla \cdot (\mathbf{T}^T \mathbf{v}) = \mathbf{T} : \nabla \mathbf{v} + \mathbf{v} \cdot (\nabla \cdot \mathbf{T}).$$

Using this and the divergence theorem, we have A as

$$\begin{aligned} \int_V \nabla \cdot (\nabla \phi \mathbf{S}_0) \cdot \phi dV &= \int_V \nabla \cdot [(\nabla \phi \mathbf{S}_0)^T \phi] dV - \int_V \nabla \phi \mathbf{S}_0 : \nabla \phi dV \\ &= \int_S [(\nabla \phi \mathbf{S}_0)^T \phi] \cdot \mathbf{n} dS - \int_V \nabla \phi \mathbf{S}_0 : \nabla \phi dV, \end{aligned} \quad (5.2)$$

where the unit vector \mathbf{n} (distinct from $\hat{\mathbf{n}}$ used previously) is normal to the surface of the rotor.

The surface S bounding the domain V can in some problems be split into a displacement specified surface S_u and a traction specified S_t . On S_u , ϕ is zero and hence the surface integral term corresponding to S_u is zero. On the traction free surface S_t , we have

$$[(\nabla \phi \mathbf{S}_0)^T \phi] \cdot \mathbf{n} = \phi \cdot (\nabla \phi \mathbf{S}_0) \mathbf{n} = \phi \cdot \nabla \phi (\mathbf{S}_0 \mathbf{n}) = 0,$$

because $\mathbf{S}_0 \mathbf{n}$ is zero there.

Under more general restraints on the rotor, this surface term may turn out to be important, and need accurate evaluation.

Now that all the terms in our modal projection (Eq. 5.1) are known, Ω_c can be found. The validity of this equation will be demonstrated with several analytical examples in chapter 6. The numerical application of this method will be demonstrated with seven different rotor geometries in chapter 8.

5.2 Multi-mode projections (method 1)

The previous calculations involved a single mode projection. However, the method can be easily extended to multiple modes. We write the displacement of the rotor as (corresponding to Eq. 4.2)

$$\mathbf{u} = \epsilon \mathbf{u}_0 + \sum_{k=1}^m a_k \phi_k.$$

Here ϕ_k is the k^{th} retained mode of vibration (lateral or otherwise) and a_k is an undetermined coefficient. Using m different virtual displacements, $\delta a_k \phi_k$, we would get m equations. Mass orthogonality of the mode shapes would give some simplifications. Eventually, the critical speed Ω_c would be found by solving an m -dimensional eigenvalue problem.

For example, consider a two mode projection involving modes ϕ_1 and ϕ_2 . Taking virtual displacements $\delta a_1 \phi_1$ and $\delta a_2 \phi_2$, the virtual work equations are

$$a_1 \int_V (\nabla \cdot (\nabla \phi_1 \mathbf{S}_0)) \cdot \phi_1 dV + a_2 \int_V (\nabla \cdot (\nabla \phi_2 \mathbf{S}_0)) \cdot \phi_1 dV + a_1 \int_V (\nabla \cdot \mathbf{S}_1) \cdot \phi_1 dV +$$

$$\cancel{a_2 \int_V (\nabla \cdot \mathbf{S}_2) \cdot \phi_1 dV} \overset{0}{=} \Omega_c^2 a_1 \int_V \rho_0 (\hat{\mathbf{n}} \times \hat{\mathbf{n}} \times \phi_1) \cdot \phi_1 dV + \Omega_c^2 a_2 \int_V \rho_0 (\hat{\mathbf{n}} \times \hat{\mathbf{n}} \times \phi_2) \cdot \phi_1 dV,$$

and

$$a_1 \int_V (\nabla \cdot (\nabla \phi_1 \mathbf{S}_0)) \cdot \phi_2 dV + a_2 \int_V (\nabla \cdot (\nabla \phi_2 \mathbf{S}_0)) \cdot \phi_2 dV + a_1 \int_V (\nabla \cdot \mathbf{S}_1) \cdot \phi_2 dV +$$

$$a_2 \int_V (\nabla \cdot \mathbf{S}_2) \cdot \phi_2 dV = \Omega_c^2 a_1 \int_V \rho_0 (\hat{\mathbf{n}} \times \hat{\mathbf{n}} \times \phi_1) \cdot \phi_2 dV + \Omega_c^2 a_2 \int_V \rho_0 (\hat{\mathbf{n}} \times \hat{\mathbf{n}} \times \phi_2) \cdot \phi_2 dV,$$

where the terms crossed out are zero from the mass orthogonality of the chosen mode shapes, since $\nabla \cdot \mathbf{S}_1 = -\rho \omega_1^2 \phi_1$ and similarly for ϕ_2 . Writing in matrix notation we get the following eigenvalue problem for calculating the critical speed

$$\mathbf{A} \mathbf{x} = \Omega_c^2 \mathbf{B} \mathbf{x},$$

where $\mathbf{x} = [a_1 \ a_2]^T$, and \mathbf{A} and \mathbf{B} are coefficient matrices obtained from the above equations. For a modal projection involving m modes, we get m equations and the square matrices \mathbf{A} and \mathbf{B} are of size $m \times m$.

5.3 Modal projection method 2

The foregoing discussion allows us to present an alternative, iterative technique suitable for working with commercial codes like ANSYS. We start with an initial guess for the critical speed. We might, for example, start with $\Omega_{c,0}$ equal to the fundamental frequency of lateral vibrations of the non-spinning rotor. At the k^{th} iteration, let the working guess be $\Omega_{c,k}$. The iteration proceeds as follows.

1. We do an axisymmetric and linear elastic calculation for the rotor in pure spin at a speed $\Omega_{c,k}$. This gives a stress state which we call $\boldsymbol{\tau}_k$.
2. We specify $\boldsymbol{\tau}_k$ as a prestress (this step finds wide industrial use) in the non-spinning rotor, and find new bending frequencies ω_f and mode shapes ϕ .

3. Using these, we conduct the modal projection of chapter 3 (i.e., Eq. 3.4) to obtain a new estimate of the whirling speed, $\Omega_{c,k+1}$.
4. We stop when $\Omega_{c,k+1}$ is acceptably close to $\Omega_{c,k}$.

Note that inclusion of the prestress makes this calculation different from that in chapter 3, although the steps in the calculation are similar. It can be shown that this iterative procedure is in principle equivalent to carrying out the modal projection of the previous section, except that the boundary term of Eq. 5.2 is not retained; and that in this case the mode shapes correspond to a prestressed (though stationary) rotor, and may differ from those of the unstressed rotor. An interesting point is that this iterative solution will only find real whirling speeds, while the modal projection of section 4.3 finds some imaginary whirling speeds as well (which correspond to imaginable whirling modes that are in fact suppressed due to the gyroscopic effects). For example, in Ewins's rotor described in chapter 3, the critical speed is given by

$$\Omega_c = \sqrt{\frac{k}{M(1 - R^2/4L^2)}},$$

and this is imaginary if $R^2/4L^2 > 1$.

5.4 Comparisons with other formulations

5.4.1 Comparison with Nandi and Neogy's method

Nandi and Neogy [18] initially presented governing equations (their Eq. 4) which in principle match our own initially attempted (incorrect) modal projection method of chapter 3. However, they subsequently added on an inertial term which we believe can give good results, but which is *ad hoc* in that it is not derived from underlying continuum equations. Our incorrect modal projection method's predicted critical speed is (from Eq. 3.4)

$$\Omega_c^2 = \frac{-\omega_f^2}{\int_V \rho_0 (\hat{\mathbf{n}} \times \hat{\mathbf{n}} \times \boldsymbol{\phi}) \cdot \boldsymbol{\phi} dV}.$$

Assuming that the rotor is spinning about the Z axis, the angular velocity is $\Omega_c \hat{\mathbf{k}}$. In this case the denominator of the above expression becomes (dropping the inconsequential 0 subscript in ρ)

$$\int_V \rho (\hat{\mathbf{k}} \times \hat{\mathbf{k}} \times \boldsymbol{\phi}) \cdot \boldsymbol{\phi} dV.$$

Writing $\boldsymbol{\phi} = \phi_x \hat{\mathbf{i}} + \phi_y \hat{\mathbf{j}} + \phi_z \hat{\mathbf{k}}$, the above equation becomes

$$- \int_V \rho (\phi_x^2 + \phi_y^2) dV.$$

It can be shown that Nandi and Neogy's method is equivalent to adding a correction term to the above expression. Their equation for critical speed after incorporating the correction term is

$$\Omega_c^2 = \frac{-\omega_f^2}{-\int_V \rho (\phi_x^2 + \phi_y^2 - \phi_z^2) dV}.$$

The critical speed as predicted by our modal projection method 1 (from Eq. 5.1) can be written as

$$\Omega_c^2 = \frac{-\omega_f^2}{-\int_V \rho (\phi_x^2 + \phi_y^2) dV - \int_V \boldsymbol{\nabla} \cdot (\boldsymbol{\nabla} \boldsymbol{\phi} \tilde{\mathbf{S}}_0) \cdot \boldsymbol{\phi} dV},$$

where $\tilde{\mathbf{S}}_0$ is the stress induced due to a spin of 1 rad/s. Thus Nandi and Neogy's method is equivalent to our modal projection method 1 if

$$\int_V \rho \phi_z^2 dV = - \int_V \boldsymbol{\nabla} \cdot (\boldsymbol{\nabla} \boldsymbol{\phi} \tilde{\mathbf{S}}_0) \cdot \boldsymbol{\phi} dV. \quad (5.3)$$

As far as we know, the above condition does not always hold. However, for a long uniform isotropic elastic cylinder, with the assumption that plane sections remain plane with no in-plane deformation, the displacement of a point located at (x, y, z) on the cross section is

$$\boldsymbol{\phi} = \left\{ \begin{array}{c} u(z) \\ v(z) \\ -x\psi_1(z) + y\psi_2(z) \end{array} \right\},$$

where ψ_1 and ψ_2 are rotations of the cross section about the Y and X axis respectively. Substituting this $\boldsymbol{\phi}$ in Eq. 5.3 and taking $\tilde{\mathbf{S}}_0$ from the expression for stress in a rotating elastic cylinder (spin speed = 1 rad/s) in plane strain:

$$\tilde{\mathbf{S}}_0 = \begin{bmatrix} \frac{\rho}{8}(-y^2 - 3x^2 + 3R^2) & -\frac{\rho}{4}xy & 0 \\ -\frac{\rho}{4}xy & \frac{\rho}{8}(-3y^2 - x^2 + 3R^2) & 0 \\ 0 & 0 & 0 \end{bmatrix},$$

where R is the radius of the cylinder, and (x, y) are points on the cylinder measured in the rotating coordinate system, we finally get

$$-\int_V \nabla \cdot (\nabla \phi \tilde{\mathbf{S}}_0) \cdot \phi dV = \int_V \rho (-x\psi_1(z) + y\psi_2(z)) \cdot (-x\psi_1(z) + y\psi_2(z)) dV = \int_V \rho \phi_z^2 dV.$$

Thus our method is equivalent to Nandi and Neogy's method under these assumptions. However, for a general case it is difficult to make a legitimate comparison. We conclude that Nandi and Neogy's *ad hoc* method may often give accurate results. However, our method, derived from a continuum based formulation, continues to hold true even for arbitrary rotors with more general deformation.

5.4.2 Comparison with Stephenson and Rouch

Stephenson and Rouch [27], [17], who used axisymmetric harmonic elements, added a separately calculated matrix of gyroscopic terms (much in the spirit of the Timoshenko rotor analysis of Choi *et al.* [22]). Our approach differs from that of adding on element-level gyroscopic terms (as in the work of Stephenson and Rouch) in several significant ways. The idea of adding on such gyroscopic (inertial) terms is shown to be correct using a verifying finite-strain calculation for Timoshenko rotors by Choi *et al.* [22]. However, as far as we know, such terms have not been derived starting from continuum level formulations; rather, these terms are added on based on engineering insights, and lead to specialized finite element formulations that are not included with typical commercial finite element packages. Here, in contrast with Stephenson and Rouch, we have offered a continuum point-level, stress based treatment that both keeps track of all terms dropped or retained, as well as provides some fresh physical insights. Moreover, while they adopt a matrix reduction technique based on explicit choice of master and slave degrees of freedom, we have adopted the simpler strategy of projecting the governing equations directly on to a small number of lateral vibration modes. While they present a single approach for solution and compare their results with known formulas for cylindrical shafts, we will consider several non-cylindrical geometries and cross-check our results using several different methods of solution. Lastly, while they further compare their calculations with experimental results for a particular rotor with bearing compliance and damping effects, we will restrict our attention to computations for the ideal case but present more detailed analytical and numerical comparisons.

5.5 Concluding remarks

Whirling speeds of arbitrary rotors have been considered in this chapter. The aim has been to estimate these speeds accurately using modal projections that can be used with routinely available commercial finite element packages. Two such modal projection methods have been presented, both based on a single and simple new insight, which is that the gyroscopic terms commonly used in rotor dynamics analyses may be viewed as arising out of a state of prestress caused by the nonzero spin rate. Having developed the methods, we now proceed to validate them with some analytical examples in the next chapter.

Chapter 6

Analytical examples

In this chapter we validate our formulation using several analytical examples. We emphasize that all of the problems considered here can be solved using conventional methods. These examples have been included here just to demonstrate the validity of our formulation.

Before considering rotor examples, we briefly revisit some classical buckling problems. Solving buckling problems with a prestress based formulation is not novel. Bolotin [26] has considered such problems. Nevertheless these examples serve to illustrate the fundamental similarity between rotor whirl and buckling.

We then return to rotors and consider a detailed analytical example of a rigid spinning disc attached to a massless rod and supported by springs (Ewins's rotor). We consider both synchronous and asynchronous whirl. Results from our method will match those obtained using the conventional gyroscopic matrix based approach, providing an analytical verification of our formulation.

We then derive the equations of a spinning torque free rigid cylinder using our formulation and derive the classical equations of motion with gyroscopic terms. This provides further analytical validation of the equivalence between the prestress based approach and the gyroscopic term based approach.

We end this chapter by solving a different type of rotor problem; a rotating cantilever beam (like a helicopter blade). The most basic model of foreshortening encountered in such systems is recovered from our formulation

6.1 Some classical buckling problems

6.1.1 The basic equation of Euler-Bernoulli buckling

We now consider an Euler-Bernoulli column of rigidity modulus EI and subjected to an axial compressive load P . We start with Eq. 4.5 derived in chapter 4, choose a virtual displacement $\delta\mathbf{w}$ and perform virtual work to get

$$\int_V (\nabla \cdot \nabla \phi \mathbf{S}_0) \cdot \delta\mathbf{w} dV + \int_V (\nabla \cdot \mathbf{S}_1) \cdot \delta\mathbf{w} dV = 0, \quad (6.1)$$

where ϕ and \mathbf{S}_1 have their usual meaning and \mathbf{S}_0 is now the prestress due to the axially applied compressive load on the column. Note that, since there is no motion involved in a buckling calculation, the acceleration is zero. Let the displacement of the column, bending

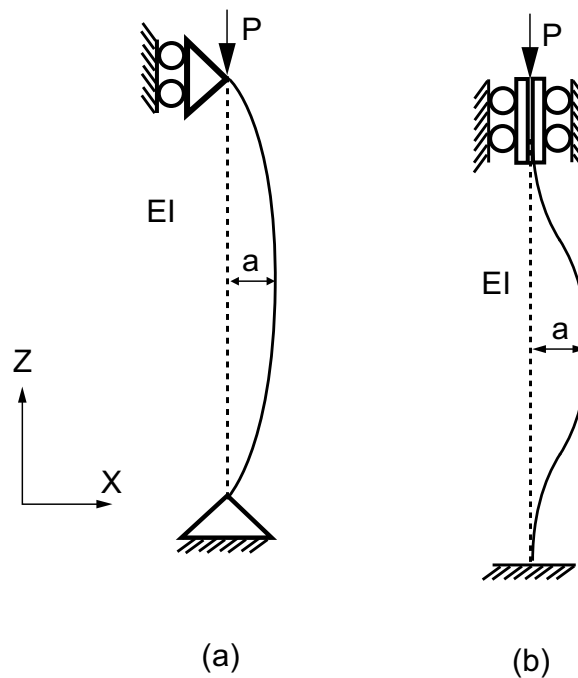


Figure 6.1: Buckling of columns: Case (a) pinned-pinned (b) fixed-fixed.

in the X - Z plane, be ϕ . Under Euler-Bernoulli assumptions

$$\phi = \begin{bmatrix} u \\ 0 \\ -x \frac{du}{dz} \end{bmatrix}, \quad (6.2)$$

where u is the displacement in the X direction. Ignoring Poisson's effects the displacement in the Y direction is taken as zero. The prestress \mathbf{S}_0 in the column arises from the axial load P and the components of this stress are

$$\mathbf{S}_0 = \begin{bmatrix} 0 & 0 & 0 \\ 0 & 0 & 0 \\ 0 & 0 & -P/A \end{bmatrix}, \quad (6.3)$$

where A is the cross sectional area. The stress \mathbf{S}_1 is due to infinitesimal bending and the components of this stress are given by

$$\mathbf{S}_1 = \begin{bmatrix} 0 & 0 & 0 \\ 0 & 0 & 0 \\ 0 & 0 & -Ex \frac{d^2u}{dz^2} \end{bmatrix}, \quad (6.4)$$

where E is the Young's modulus of the material. Substituting these values in Eq. 6.1 and taking the virtual displacement as

$$\delta \mathbf{w} = \begin{bmatrix} \delta w \\ 0 \\ -x \frac{d(\delta w)}{dz} \end{bmatrix}, \quad (6.5)$$

we get

$$\int_V \left(-\frac{P}{A} \frac{d^2u}{dz^2} \cdot \delta w + \left(E - \frac{P}{A} \right) x^2 \frac{d^3u}{dz^3} \cdot \frac{d(\delta w)}{dz} \right) dV = 0,$$

or

$$\int_0^l \int_{\bar{A}} \left(-\frac{P}{A} \frac{d^2u}{dz^2} \cdot \delta w + \left(E - \frac{P}{A} \right) x^2 \frac{d^3u}{dz^3} \cdot \frac{d(\delta w)}{dz} \right) d\bar{A} dz = 0.$$

where \bar{A} represents the cross sectional area as a domain of integration, distinct from A , which we use to denote the numerical value of the total cross sectional area. Since none of the variables u , z and w vary across the cross section, the above integral becomes

$$\int_0^l \left(-P \frac{d^2u}{dz^2} \cdot \delta w + \left(E - \frac{P}{A} \right) I \frac{d^3u}{dz^3} \cdot \frac{d(\delta w)}{dz} \right) dz = 0,$$

where I is the area moment of inertia of the cross section. Integrating by parts the second term in the above integrand, imposing boundary conditions, and noting specifically that for free ends we require $\left. \frac{d^3 u}{dz^3} \right|_l = 0$, we obtain with no further restrictions:

$$\int_0^l \left(-P \frac{d^2 u}{dz^2} + \left(\frac{P}{A} - E \right) I \frac{d^4 u}{dz^4} \right) \delta w dz = 0. \quad (6.6)$$

Now since δw is arbitrary, the term in the brackets in the above integrand must be identically zero, giving the governing equation for buckling of a beam subjected to an axial compressive load P . Since the Young's modulus $E \gg P/A$ for the problems of interest¹, the above equation reduces to

$$EI \frac{d^4 u}{dz^4} + P \frac{d^2 u}{dz^2} = 0,$$

which is the familiar equation governing buckling of Euler-Bernoulli beams. We emphasize that the above equation can be obtained using the classical strength of materials approach; the interesting thing here is merely that, starting from nonlinear elasticity, a continuum formulation, and an intuitive interpretation that lets us simplify the continuum formulation, we have in fact obtained the same equation.

Although we were able to obtain the governing differential equation for buckling of Euler-Bernoulli columns, in this thesis we are strongly interested in modal projections. Accordingly, we will use modal projections to solve the problem, i.e., we will assume a functional form for the displacement function $u = af(z)$, set the virtual displacement $\delta w = \delta a f(z)$, and use Eq. 6.6 to obtain the buckling load. We consider two sets of boundary conditions.

- (a) A pinned-pinned beam.

For this case, shown in figure 6.1a, we take

$$u = a \sin \left(\frac{\pi z}{l} \right),$$

where l is the length of the beam and a is the maximum displacement occurring at the center of the beam. Substituting this into Eq. 6.6 and letting $\delta w = \delta a \sin \left(\frac{\pi z}{l} \right)$,

¹In all subsequent buckling calculations in this chapter, P/A has consistently been dropped in comparison with E .

integrating and solving for P we get

$$P_{cr} = \frac{\pi^2 EI}{l^2}.$$

This matches the classical result.

(b) A fixed-fixed column.

For this case, shown in figure 6.1c, we let

$$u = a \left(1 - \cos \left(\frac{2\pi z}{l} \right) \right).$$

This satisfies the essential boundary conditions at the fixed ends. Now a is the displacement of the center. Again proceeding as before, we obtain

$$P_{cr} = \frac{4\pi^2 EI}{l^2},$$

matching the classical result.

6.1.2 Columns with Other Loading

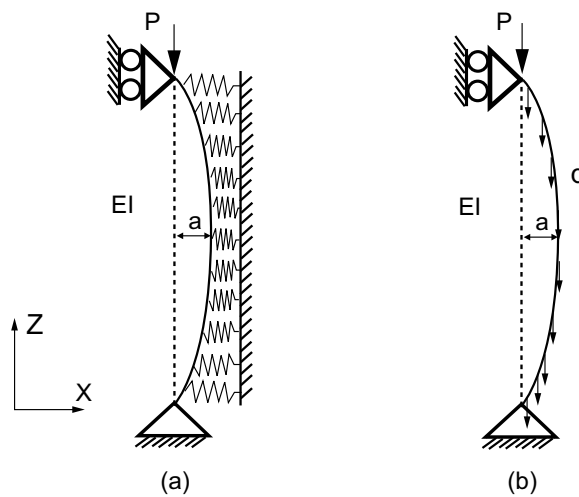


Figure 6.2: (a) Buckling of a pinned-pinned column with lateral elastic support. (b) Buckling of a pinned-pinned column under its own weight.

6.1.2.1 A simply supported column under axial load and with elastic lateral support

Consider a pinned-pinned beam with an elastic lateral support (as in [28]) of stiffness k , as shown in figure 6.2 a, and subjected to an axial compressive force P . In this case, in addition to the axial stresses due to infinitesimal bending, there will be compressive stresses due to elastic forces from the side. For this problem, there is non-zero traction on the lateral surface which will contribute to the virtual work. Hence Eq. 6.1, modified to take into account the work done by traction forces, is

$$\int_V (\nabla \cdot (\nabla \phi \mathbf{S}_0)) \cdot \delta \mathbf{w} dV + \int_V (\nabla \cdot \mathbf{S}_1) \cdot \delta \mathbf{w} dV + \int_S \mathbf{t} \cdot \delta \mathbf{w} dS = 0.$$

The traction force per unit length is $\mathbf{t} = ku \mathbf{i}$, where \mathbf{i} is the unit vector along the X direction. Adding the work done by this term we get the governing equation for buckling of a column with elastic lateral supports as

$$\int_V (\nabla \cdot (\nabla \phi \mathbf{S}_0)) \cdot \delta \mathbf{w} dV + \int_V (\nabla \cdot \mathbf{S}_1) \cdot \delta \mathbf{w} dV - \int_0^l ku \mathbf{i} \cdot \delta \mathbf{w} dz = 0. \quad (6.7)$$

Assuming the displacement along the X direction to be

$$u = a \sin\left(\frac{\pi z}{l}\right),$$

ϕ is obtained from Eq. 6.2. The virtual displacement is taken as $\delta \mathbf{w} = (\delta a/a)\phi$. Substituting $\delta \mathbf{w}$, ϕ , Eq. 6.3 and Eq. 6.4 into Eq. 6.7, the critical buckling load P is obtained as

$$P_{cr} = \frac{\pi^2 EI}{l^2} \left(1 + \frac{kl^4}{EI\pi^4}\right).$$

This again matches the classical result (see [28], equation 2-37, with $m = 1$).

6.1.2.2 A simply supported column under axial load and self weight

Let the column have a mass density of q/g per unit length, where g is the acceleration due to gravity; in other words, the self weight per unit length is q . In this section we derive the critical value of axial load P for a given q (see figure 6.2 b). Including the effects of axial

load as well as self weight, the prestress \mathbf{S}_0 in this case is given by

$$\mathbf{S}_0 = \begin{bmatrix} 0 & 0 & 0 \\ 0 & 0 & 0 \\ 0 & 0 & -\frac{P}{A} + \frac{q}{A}(z-l) \end{bmatrix}.$$

Using this, Eq. 6.5 and taking \mathbf{S}_1 and ϕ from Eq. 6.2 and Eq. 6.4 respectively and substituting in Eq. 6.1 we get the following equation

$$\int_0^l \left(EI \frac{d^4 u}{dz^4} \right) \cdot \delta w + \left(P \frac{d^2 u}{dz^2} - q(z-l) \frac{d^2 u}{dz^2} - q \frac{du}{dz} \right) \delta w dz = 0. \quad (6.8)$$

Now, for easy comparison with the results in [28], we take $q = \frac{\pi^2 EI}{l^3}$ and calculate P_{cr} , for comparison with the classical result,

$$P_{cr} = \frac{4.77EI}{l^2}.$$

Using as a first approximation $u = a \sin\left(\frac{\pi z}{l}\right)$, we use Eq. 6.8 and obtain

$$P_{cr} = \frac{4.93EI}{l^2}.$$

The small mismatch is due to the fact that the actual buckled shape does not coincide with our assumed u . We can improve the accuracy by taking two terms,

$$u = a \sin\left(\frac{\pi z}{l}\right) + b \sin\left(\frac{2\pi z}{l}\right).$$

In this case we obtain two equations by letting δw in Eq. 6.8 to be $\delta a \sin\left(\frac{\pi z}{l}\right)$ and $\delta b \sin\left(\frac{2\pi z}{l}\right)$ respectively. The critical load is obtained by setting the determinant of the resulting matrix of coefficients to zero so that buckling solutions are possible. The matrix obtained is

$$\begin{bmatrix} \frac{\pi^2(18Pl^2 + 9ql^3 - 18EI\pi^2)}{36l^3} & \frac{20q}{9} \\ \frac{20q}{9} & \frac{\pi^2(18Pl^2 + 9ql^3 - 72EI\pi^2)}{9l^3} \end{bmatrix}.$$

Substituting $q = \frac{\pi^2 EI}{l^3}$ and setting the determinant of the above matrix to zero, we calculate the critical load as

$$P_{cr} = \frac{4.77EI}{l^2},$$

which matches the classical result to the number of significant digits shown. Alternatively, by setting $P = 0$ we can calculate the critical q at which the column will buckle as

$$q_{cr} = \frac{1.88EI}{l^3},$$

which again matches the classical result (an interpolation is required between discrete values given in table 2.8 of [28]).

6.1.3 Buckling of a Ring

In this section we derive the critical buckling load for a thin ring subjected to a uniform external radial loading (or external “pressure”; see figure 6.3). The classical solution is [28, 29]

$$q = \frac{3EI}{R^3},$$

where E is the Young’s Modulus of the material, I is the area moment of inertia of the cross section and R is the radius of the ring.

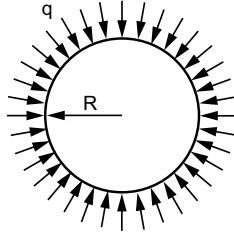


Figure 6.3: A uniformly loaded thin ring.

As in the case of the example of a column with lateral elastic support, the externally applied pressure will do work in a virtual displacement. We modify Eq. 6.1 to account for this work and obtain

$$\int_V (\nabla \cdot \nabla \phi \mathbf{S}_0) \cdot \delta \mathbf{w} dV + \int_V (\nabla \cdot \mathbf{S}_1) \cdot \delta \mathbf{w} dV + \delta W_q = 0, \quad (6.9)$$

where ϕ is the displacement of a point on the ring, \mathbf{S}_0 is the prestress due to the uniform pressure loading, \mathbf{S}_1 is the stress due to infinitesimal bending from the original configuration, δW_q is the virtual work done by the externally applied pressure q and $\delta \mathbf{w}$ is a virtual displacement.

The displacement of the ring contains a radial component w as shown on the right of figure 6.4. Cross sections rotate, and there is a tangential displacement as well (to preserve inextensibility along the neutral axis). No displacement is taken in the z direction, perpendicular to the plane of the ring (Poisson's ratio $\nu = 0$). The radial displacement of the ring is taken as $w = a \cos(2\theta)$. Using this, the displacement ϕ of a point on the ring in a cylindrical coordinate system is given by

$$\phi = a \cos(2\theta) \hat{e}_r + 2a \left(\frac{r}{R} - 1 \right) \sin(2\theta) \hat{e}_\theta,$$

where \hat{e}_r and \hat{e}_θ are unit vectors along the radial and tangential directions respectively. Rewriting using matrix notation, we have

$$\phi = \begin{bmatrix} a \cos(2\theta) \\ 2a \left(\frac{r}{R} - 1 \right) \sin(2\theta) \\ 0 \end{bmatrix}.$$

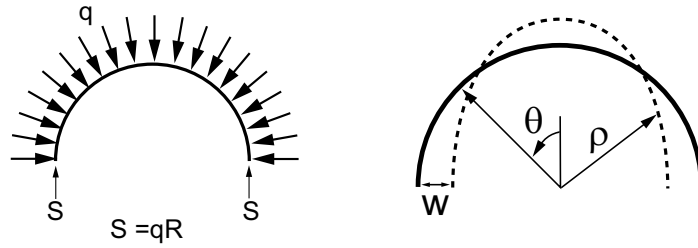


Figure 6.4: Force and displacement.

Next we calculate the prestress \mathbf{S}_0 due to the uniformly applied pressure q . Due to the uniform pressure q a compressive force S develops in the ring. This force is assumed to be uniform along the cross section. From a free body diagram of half the ring (see figure 6.4 left) the magnitude of the force S can be calculated as

$$S = qR.$$

Thus the prestress expressed in cylindrical coordinates is

$$\mathbf{S}_0 = \begin{bmatrix} 0 & 0 & 0 \\ 0 & -\frac{qR}{A} & 0 \\ 0 & 0 & 0 \end{bmatrix},$$

where A is the cross sectional area of the ring and the negative sign indicates compressive stress.

Next, we calculate the stress induced due to the infinitesimal bending of the ring. We consider a small fiber along the neutral axis of the ring of length $Rd\theta$. After bending the radius of curvature changes to ρ and the subtended angle changes to $d\psi$. Since the fiber along the neutral axis does not change in length

$$Rd\theta = \rho d\psi.$$

For a typical fiber away from the neutral axis, the change in length can be calculated as follows. Let the fiber be at a distance $y = r - R$ from the neutral axis. Then its original length is

$$L_0 = (R + y)d\theta,$$

and the length after bending is

$$L = (\rho + y)d\psi.$$

The elongation strain in the fiber is

$$\epsilon_\theta = \frac{L - L_0}{L_0} = y \left(\frac{1}{\rho} - \frac{1}{R} \right).$$

The tangential stress therefore is

$$\sigma_\theta = E\epsilon_\theta = Ey \left(\frac{1}{\rho} - \frac{1}{R} \right).$$

Using the well known relation between change in curvature and radial displacement w (see [28]) and using $y = r - R$ we get

$$\sigma_\theta = E(r - R) \left(\frac{1}{R^2} \frac{d^2w}{d\theta^2} + \frac{w}{R^2} \right).$$

We will use ϕ corresponding to $w = a \cos(2\theta)$ as indicated above. The bending stress components in cylindrical coordinates is

$$\mathbf{S}_1 = \begin{bmatrix} 0 & 0 & 0 \\ 0 & \sigma_\theta & 0 \\ 0 & 0 & 0 \end{bmatrix}.$$

The virtual displacement is taken as

$$\delta \mathbf{w} = \begin{bmatrix} \delta a \cos(2\theta) \\ \delta a 2 \left(\frac{r}{R} - 1 \right) \sin(2\theta) \\ 0 \end{bmatrix}.$$

For this choice of virtual displacement, the virtual work done by the externally applied radial pressure q (assuming thickness of the ring is accounted in q) becomes

$$\delta W_q = \int_0^{2\pi} q R \delta a \cos 2\theta d\theta = 0.$$

Substituting the above expressions for \mathbf{S}_1 , \mathbf{S}_0 and $\boldsymbol{\phi}$ along with the formulas for calculating gradient of vectors and divergence of a second order tensor in cylindrical coordinates as given in Appendix B.1 into Eq. 6.9 we get

$$\int_0^{2\pi} \int_{R-c_1}^{R+c_2} g(R, q, E, \theta, r) r dr d\theta = 0, \quad (6.10)$$

where the function g is given in the appendix B.2 and, c_1 and c_2 are the distances of the extreme fibers from the neutral axis. Upon performing the integration and assuming $R \gg c_1, c_2$ we get for the critical load

$$q_{cr} = \frac{3EI}{R^3},$$

matching the classical result.

6.2 Ewins's rotor

We consider a rotor from Ewins [25], shown here in figure 6.5. Note that this simple system is easily treated using rigid body mechanics. We select Ewins's rotor because it is the simplest rotor system we know on which our ideas can be tested analytically.

The massless rigid shaft serves only to kinematically couple the disk's translation and tilt.

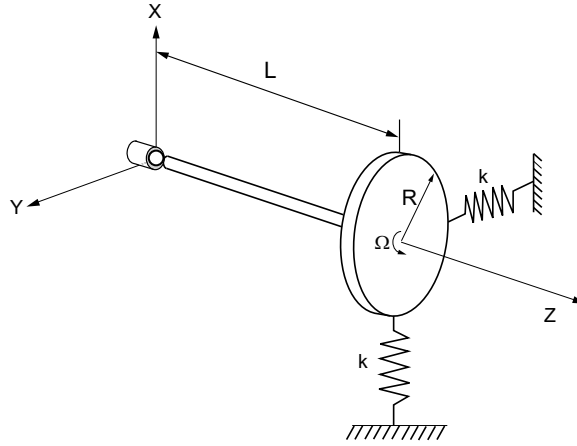


Figure 6.5: A heavy disk rigidly attached to a massless shaft and supported by two springs at the end. The shaft and disk system spins at a speed of Ω . The unloaded end of the shaft is constrained in a ball and socket joint.

6.2.1 Ewins's solution (including explicit gyroscopic terms)

The equations of motion in lab-fixed coordinates are [25]

$$\begin{bmatrix} I_0/L & 0 \\ 0 & I_0/L \end{bmatrix} \begin{Bmatrix} \ddot{X} \\ \ddot{Y} \end{Bmatrix} + \underbrace{\begin{bmatrix} 0 & J\Omega/L \\ -J\Omega/L & 0 \end{bmatrix}}_G \begin{Bmatrix} \dot{X} \\ \dot{Y} \end{Bmatrix} + \begin{bmatrix} kL & 0 \\ 0 & kL \end{bmatrix} \begin{Bmatrix} X \\ Y \end{Bmatrix} = \begin{Bmatrix} 0 \\ 0 \end{Bmatrix}, \quad (6.11)$$

where I_0 is the mass moment of inertia of the system about the X - or Y -axis, J is the polar mass moment of inertia of the disk-shaft system, and the mass of the disk is M . Matrix G above is the gyroscopic matrix. The natural frequencies of the system at any spin speed, Ω , are obtained by Ewins from Eq. 6.11 as

$$\omega_1 = \omega_\Omega - \frac{1}{2}\gamma\Omega,$$

$$\omega_2 = \omega_\Omega + \frac{1}{2}\gamma\Omega,$$

where

$$\gamma = \frac{J}{I_0}; \quad \omega_\Omega^2 = \frac{kL^2}{I_0} + \frac{1}{4}(\gamma\Omega)^2 = \omega_0^2 + \frac{1}{4}(\gamma\Omega)^2.$$

In particular the forward synchronous whirl speed is

$$\Omega_c = \frac{\omega_0}{\sqrt{(1-\gamma)}} = \sqrt{\frac{k}{M(1-R^2/4L^2)}}.$$

Note that for the case when $R > 4L$, the critical speed becomes imaginary indicating suppression of whirling by gyroscopic effects.

6.2.2 Our formulation (no explicit gyroscopic terms)

Our governing equation (Eq. 4.5) is

$$\nabla \cdot \mathbf{S}_0 + \nabla \cdot \mathbf{S}_1 + \nabla \cdot (\nabla \phi \mathbf{S}_0) = \rho_0 \frac{\partial^2 \boldsymbol{\chi}}{\partial t^2}. \quad (6.12)$$

From dynamic equilibrium of the rotor in pure spin we have (using linear elasticity)

$$\nabla \cdot \mathbf{S}_0 = \rho_0 (\boldsymbol{\Omega} \times \boldsymbol{\Omega} \times \mathbf{r}),$$

where \mathbf{r} is the reference position vector of the point under consideration.

Choosing any virtual displacement $\delta \mathbf{w}$, the virtual work equation is

$$\int_V \left\{ \nabla \cdot \mathbf{S}_0 + \nabla \cdot \mathbf{S}_1 + \nabla \cdot (\nabla \phi \mathbf{S}_0) - \rho \frac{\partial^2 \boldsymbol{\chi}}{\partial t^2} \right\} \cdot \delta \mathbf{w} dV = 0, \quad (6.13)$$

where the inconsequential zero subscript in ρ has been dropped.

Following our procedure, we first determine the natural frequency and mode shape of the non-spinning system. For vibrations in the X - Z plane, the governing equation is

$$(I_0/L)\ddot{x} + kLx = 0,$$

The natural frequency is $\omega_f = \sqrt{(kL^2/I_0)}$. The mode shape is shown in figure 6.6. The natural frequency and mode shape of vibration in the Y - Z plane is similar to that in the X - Z plane.

Next, we need the spin-induced stresses (\mathbf{S}_0) in the disk. The disk is treated as a stiff but isotropic elastic body with Young's modulus E and Poisson's ratio $\nu = 0$ (for

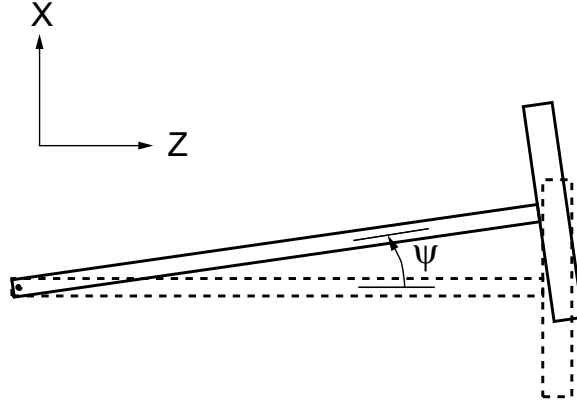


Figure 6.6: Lateral vibration mode of the system.

simplicity). The plane stress solution for a spinning disk is given in polar coordinates by Timoshenko and Goodier (1970, pp. 81) [30]. The stress components are rewritten in Cartesian coordinates using formulas given in the same book (pp. 67). At a point (x, y) on the disk, we have

$$\begin{aligned} S_{0,xx} &= \frac{\rho\Omega^2}{8}(3R^2 - 3x^2 - y^2), \\ S_{0,xy} &= -\frac{1}{4}\rho\Omega^2 xy, \\ S_{0,yy} &= \frac{\rho\Omega^2}{8}(3R^2 - x^2 - 3y^2), \\ S_{0,xz} &= S_{0,yz} = S_{0,zz} = 0. \end{aligned}$$

The displacements and stresses are uniform through the thickness of the disk, which for integration purposes may be taken as unity.

6.2.2.1 Calculation of critical speed

We now use Eq. 5.1 to calculate the critical speed. Since ϕ is itself a vibrational mode (being a linear combination of two modes with the same frequency), we have (as discussed in chapter 5, as also in [26])

$$\int_V (\nabla \cdot \mathbf{S}_1) \cdot \phi \, dV = -\omega_f^2 \int_V \rho \phi \cdot \phi \, dV,$$

as described. Taking

$$\boldsymbol{\phi} = \begin{Bmatrix} L/\sqrt{I_0} \\ 0 \\ x \\ -\frac{x}{\sqrt{I_0}} \end{Bmatrix}$$

as the displacement of a point (x, y) on the disk ensures that

$$\int_V \rho \boldsymbol{\phi} \cdot \boldsymbol{\phi} dV = 1.$$

Eq. 5.1 becomes

$$\underbrace{\int_V (\boldsymbol{\nabla} \cdot (\boldsymbol{\nabla} \boldsymbol{\phi} \mathbf{S}_0)) \cdot \boldsymbol{\phi} dV}_A - \omega_f^2 \underbrace{\int_V \rho \boldsymbol{\phi} \cdot \boldsymbol{\phi} dV}_{=1} = \Omega_c^2 \int_V \rho (\hat{\mathbf{k}} \times \hat{\mathbf{k}} \times \boldsymbol{\phi}) \cdot \boldsymbol{\phi} dV, \quad (6.14)$$

where $\hat{\mathbf{k}}$ is the unit vector along the Z -axis; and V is the volume of the disk only, since the contribution from the massless shaft is zero. The integral A in Eq. 6.14 becomes (taking the disk thickness as unity for purposes of integration)

$$\int_{-R}^R \int_{-\sqrt{R^2-y^2}}^{\sqrt{R^2-y^2}} (\boldsymbol{\nabla} \cdot (\boldsymbol{\nabla} \boldsymbol{\phi} \mathbf{S}_0)) \cdot \boldsymbol{\phi} dx dy = \int_{-R}^R \int_{-\sqrt{R^2-y^2}}^{\sqrt{R^2-y^2}} -\frac{\rho \Omega_c^2 x^2}{I_0} dx dy = -\frac{MR^2 \Omega_c^2}{4I_0}.$$

The integral on the right hand side of Eq. 6.14 becomes

$$\rho \Omega_c^2 \int_{-R}^R \int_{-\sqrt{R^2-y^2}}^{\sqrt{R^2-y^2}} (\hat{\mathbf{k}} \times \hat{\mathbf{k}} \times \boldsymbol{\phi}) \cdot \boldsymbol{\phi} dx dy = -\frac{\rho L^2 \Omega_c^2}{I_0} \int_{-R}^R \int_{-\sqrt{R^2-y^2}}^{\sqrt{R^2-y^2}} dx dy = -\frac{ML^2 \Omega_c^2}{I_0}.$$

Substituting these values in Eq. 6.14 we get the critical speed as

$$\Omega_c = \sqrt{\frac{k}{M(1 - R^2/4L^2)}},$$

which matches the result of Ewins.

6.2.2.2 Equations of motion at a general speed

At a general speed the special kinematics of synchronous whirl is lost and the whirling speed is different from the shaft spin speed. In this case, we take

$$\boldsymbol{\phi} = \begin{Bmatrix} \psi L \\ -\theta L \\ -\psi x + \theta y \end{Bmatrix} = \psi \begin{Bmatrix} L \\ 0 \\ -x \end{Bmatrix} + \theta \begin{Bmatrix} 0 \\ -L \\ y \end{Bmatrix}, \quad (6.15)$$

where θ and ψ are small rotations about the X and Y axis respectively (see figure 6.6). The acceleration $\frac{\partial^2 \boldsymbol{\chi}}{\partial t^2}$ of the material point under such conditions is given by [31]

$$\frac{\partial^2 \boldsymbol{\chi}}{\partial t^2} = \left. \frac{d^2 \boldsymbol{\phi}}{dt^2} \right|_{\text{r.f.}} + 2\boldsymbol{\Omega} \times \left. \frac{d\boldsymbol{\phi}}{dt} \right|_{\text{r.f.}} + \boldsymbol{\Omega} \times \boldsymbol{\Omega} \times (\mathbf{r} + \boldsymbol{\phi}),$$

where the subscript r.f. refers to the derivative taken in the rotating frame. The book keeping parameter a has been dropped from this equation because ψ and θ are understood to be small. The velocity and acceleration of the point as seen in the rotating frame are

$$\left. \frac{d\boldsymbol{\phi}}{dt} \right|_{\text{r.f.}} = \begin{Bmatrix} \frac{d\psi}{dt}L \\ -\frac{d\theta}{dt}L \\ -\frac{d\psi}{dt}x + \frac{d\theta}{dt}y \end{Bmatrix} \quad \text{and} \quad \left. \frac{d^2 \boldsymbol{\phi}}{dt^2} \right|_{\text{r.f.}} = \begin{Bmatrix} \frac{d^2 \psi}{dt^2}L \\ -\frac{d^2 \theta}{dt^2}L \\ -\frac{d^2 \psi}{dt^2}x + \frac{d^2 \theta}{dt^2}y \end{Bmatrix}.$$

Using the above expressions and substituting angular velocity $\boldsymbol{\Omega} = [0 \ 0 \ \Omega]^T$, we get

$$\frac{\partial^2 \boldsymbol{\chi}}{\partial t^2} = \begin{Bmatrix} \frac{d^2 \psi}{dt^2}L + 2\Omega L \frac{d\theta}{dt} - \Omega^2(x + \psi L) \\ -\frac{d^2 \theta}{dt^2}L + 2\Omega L \frac{d\psi}{dt} - \Omega^2(y - \theta L) \\ -\frac{d^2 \psi}{dt^2}x + \frac{d^2 \theta}{dt^2}y \end{Bmatrix}.$$

We consider two independent virtual displacements corresponding to variations $\delta\psi$ and $\delta\theta$. From Eq. 6.15 these virtual displacements are

$$\delta \mathbf{w}_1 = \delta\psi \begin{Bmatrix} L \\ 0 \\ -x \end{Bmatrix} \quad \text{and} \quad \delta \mathbf{w}_2 = \delta\theta \begin{Bmatrix} 0 \\ -L \\ y \end{Bmatrix}.$$

Substituting the above relations into Eq. 6.13, taking the two virtual displacements separately and carrying out the resulting two integrations, we get the following two equations (arranged in matrix form)

$$\begin{bmatrix} I_0 R^2 + 4L^2 I_0 & 0 \\ 0 & I_0 R^2 + 4L^2 I_0 \end{bmatrix} \begin{Bmatrix} \ddot{\psi} \\ \ddot{\theta} \end{Bmatrix} + \begin{bmatrix} 0 & 8L^2 I_0 \Omega \\ -8L^2 I_0 \Omega & 0 \end{bmatrix} \begin{Bmatrix} \dot{\psi} \\ \dot{\theta} \end{Bmatrix} +$$

$$\begin{bmatrix} \Omega^2 I_0 (R^2 - 4L^2) + kL^2 (R^2 + 4L^2) & 0 \\ 0 & \Omega^2 I_0 (R^2 - 4L^2) + kL^2 (R^2 + 4L^2) \end{bmatrix} \begin{Bmatrix} \psi \\ \theta \end{Bmatrix} = \begin{Bmatrix} 0 \\ 0 \end{Bmatrix}. \quad (6.16)$$

The above equations are written in a coordinate system rotating at the shaft spin rate. Substituting $\theta = -y/L$ and $\psi = x/L$, and transforming x and y to the stationary coordinates X and Y , measured in a lab-fixed frame, using

$$\begin{Bmatrix} X \\ Y \end{Bmatrix} = \begin{bmatrix} \cos(\Omega t) & -\sin(\Omega t) \\ \sin(\Omega t) & \cos(\Omega t) \end{bmatrix} \begin{Bmatrix} x \\ y \end{Bmatrix},$$

we get

$$\begin{aligned} & \begin{bmatrix} I_0 (R^2 + 4L^2) & 0 \\ 0 & I_0 (R^2 + 4L^2) \end{bmatrix} \begin{Bmatrix} \ddot{X} \\ \ddot{Y} \end{Bmatrix} + \begin{bmatrix} 0 & 2I_0 R^2 \Omega \\ -2I_0 R^2 \Omega & 0 \end{bmatrix} \begin{Bmatrix} \dot{X} \\ \dot{Y} \end{Bmatrix} \\ & + \begin{bmatrix} kL^2 R^2 + 4L^4 k & 0 \\ 0 & kL^2 R^2 + 4L^4 k \end{bmatrix} \begin{Bmatrix} X \\ Y \end{Bmatrix} = \begin{Bmatrix} 0 \\ 0 \end{Bmatrix}. \end{aligned}$$

Dividing each of the above two equations by the constant

$$(R^2 + 4L^2) L,$$

we obtain

$$\begin{aligned} & \begin{bmatrix} I_0/L & 0 \\ 0 & I_0/L \end{bmatrix} \begin{Bmatrix} \ddot{X} \\ \ddot{Y} \end{Bmatrix} + \begin{bmatrix} 0 & \left(\frac{2I_0 R^2}{R^2 + 4L^2}\right) \frac{\Omega}{L} \\ -\left(\frac{2I_0 R^2}{R^2 + 4L^2}\right) \frac{\Omega}{L} & 0 \end{bmatrix} \begin{Bmatrix} \dot{X} \\ \dot{Y} \end{Bmatrix} \\ & + \begin{bmatrix} kL & 0 \\ 0 & kL \end{bmatrix} \begin{Bmatrix} X \\ Y \end{Bmatrix} = \begin{Bmatrix} 0 \\ 0 \end{Bmatrix}. \quad (6.17) \end{aligned}$$

Finally, we note that $J = MR^2/2$, and $I_0 = MR^2/4 + ML^2$, whence

$$\frac{2I_0 R^2}{R^2 + 4L^2} = \frac{MR^2}{2} = J.$$

Substituting the above into Eq. 6.17, we get Eq. 6.11, showing analytically, for this example, that our formulation exactly captures any and all gyroscopic effects, at any and all speeds, and also describes asynchronous whirl and other related motions.

6.3 Beam plus rigid body models

So far we have considered examples for which analytical solutions exist for comparison with our formulation. We will now consider another example which is analytically tractable; similar examples will be revisited in chapter 8.

In this section we consider models which consist of a large rigid body connected to one end of a small beam which is fixed at its other end (see figure 6.7). The beam has no kinetic energy and the rigid body has no potential energy. We will illustrate the calculation with a beam-cylinder model. This model has six degrees of freedom: three coordinates (X, Y, Z) of the point O (see figure 6.7), and 1-2-3 Euler angles (θ, ϕ, ψ) describing the orientation of the cylinder.

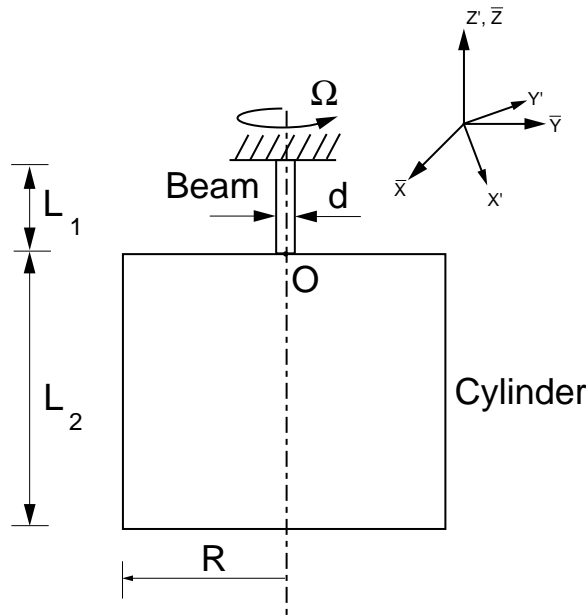


Figure 6.7: Beam cylinder model.

We first describe a general rotation matrix that will be used in the derivation. Consider a rigid body fixed at a point P . Let r be the vector from P to any other point on the rigid body. Upon rotation of the rigid body by an angle α about a unit vector n , the vector r is mapped to a new vector r' . The rotation matrix $R(n, \alpha)$ relates r and r' (r, r'

and all other vectors are taken as 3×1 column matrices of components) through

$$r' = R(n, \alpha) r. \quad (6.18)$$

The rotation matrix is defined² as (see, e.g., [33])

$$R(n, \alpha) = nn^T + \cos \alpha (I - nn^T) + \sin(\alpha) \cdot S(n),$$

where $S(n)$ is the skew-symmetric matrix defining cross products with n , i.e.,

$$n \times a = S(n) a,$$

where a is any vector.

We will use a rotating frame $(X'Y'Z')$ to write our equations. This frame spins about the inertial Z axis at the rate Ω . Viewed in this rotating frame, the point O at the tip of the cantilever beam attached to the rigid body has the coordinates (X, Y, Z) . Let e_1, e_2, e_3 be the unit vectors in the rotating frame along X', Y' and Z' directions respectively. We will define the orientation of the rigid body as seen in the rotating frame using the following rotation matrices.

$$R_1 = R(e_1, \theta)$$

defines the rotation about e_1 by an angle θ . Next, we define the rotation matrix R_2 that rotates the rigid body by an angle ϕ about the rotated e_2 axis

$$R_2 = R(R_1 e_2, \phi).$$

Similarly

$$R_3 = R(R_2 R_1 e_3, \psi)$$

defines the rotation about the twice rotated e_3 axis (once by R_2 and once by R_1) by an angle ψ .

Finally, the rotation matrix that takes the rigid body from its initial configuration, as seen in the rotating coordinate system, to the current configuration is given by

$$R_{net} = R_3 R_2 R_1.$$

²Goldstein uses a similar formula in his book [32]; but he holds the body to be fixed and the coordinate system to rotate in the opposite direction. His formula can be obtained by changing the sign of the angle in our formula 6.18 above.

These matrices will be used below in our derivation. Note that we will finally be using small deflection assumption and linearize the equations. Here, we have adopted a rotation matrix based approach due to its transparency and compactness.

Angular velocity of the rigid body with respect to the rotating frame is

$$\omega_{cylinder/rot} = [R_2 R_1 e_3 \quad R_1 e_2 \quad e_1] [\dot{\psi} \quad \dot{\phi} \quad \dot{\theta}]^T.$$

The total angular velocity of the rigid body, as seen in a fixed frame, is then

$$\omega = \omega_{cylinder/rot} + \omega_{rot/fixe d},$$

where $\omega_{rot/fixe d} = [0 \quad 0 \quad \Omega]^T$.

Now we consider the potential energy of the small beam. We will be considering only small deformations and hence the bending, stretching and twisting motions are all decoupled. Consider the in-plane X' - Z' bending of the small cantilever beam. The degrees of freedom of the point O (figure 6.7) consist of the displacement in the X' direction and rotation ϕ about the Y' axis. The stiffness matrix of the beam for in-plane bending is given by (see, e.g., [34])

$$[K] = \begin{bmatrix} 12 \frac{EI_y}{l^3} & -6 \frac{EI_y}{l^2} \\ -6 \frac{EI_y}{l^2} & 4 \frac{EI_y}{l} \end{bmatrix},$$

where E is the Young's modulus and I_y is the area moment of inertia of the cross section of the beam. Potential energy due to bending in the X' - Z' plane is, therefore,

$$PE_x = \frac{1}{2} [X \quad \phi] [K] [X \quad \phi]^T.$$

Since the beam is assumed axisymmetric and the in-plane bending in the two perpendicular planes are decoupled, the same stiffness matrix holds for bending in the Y' - Z' plane also. Hence the potential energy due to bending in the Y' - Z' plane is given by

$$PE_y = \frac{1}{2} [Y \quad \theta] [K] [Y \quad \theta]^T,$$

where the degrees of freedom are now the displacement in the Y' direction and rotation about the X' axis. Potential energy due to stretching and twisting are given by

$$PE_s = \frac{EA_c Z^2}{2l} \quad \text{and} \quad PE_t = \frac{GI_p \psi^2}{2l}$$

respectively, where I_p is the polar area moment of inertia of the beam cross section, A_c is the cross-sectional area of the beam and G is the shear modulus.

Now we consider the kinetic energy of the system. We define a reference configuration for the cylinder where its symmetry axis is aligned along the Z' axis as drawn in figure 6.7. The mass moment of inertia matrix about the center of mass, written in that reference configuration, is (using the symmetry of the cross section)

$$I_{cm-ref} = \begin{bmatrix} I_{XX} & 0 & 0 \\ 0 & I_{XX} & 0 \\ 0 & 0 & I_{ZZ} \end{bmatrix}.$$

The rotation matrix R_{net} maps the rigid body from the reference configuration to the current orientation. Thus, the mass moment of inertia matrix of the system about the center of mass, written in the current configuration after deformation, is

$$I_{cm} = [R_{net}][I_{cm-ref}][R_{net}]^T.$$

Similarly, the location of the center of mass in the reference configuration is

$$r_{cm-ref} = [0 \quad 0 \quad L/2]^T.$$

After deformation, the location of the center of mass (current configuration) is

$$r_{cm} = [X \quad Y \quad Z]^T + [R_3 R_2 R_1] r_{cm-ref}.$$

Using the formula for the derivative of a vector in a rotating frame [31]

$$v_{fixed} = \left(\frac{dr}{dt} \right)_{fixed} = \left(\frac{dr}{dt} \right)_{rotating} + \omega \times r$$

we get the velocity of the center of mass in the current configuration as

$$v_{cm} = \frac{d}{dt} r_{cm} + S(\Omega) r_{cm}.$$

Total kinetic energy of the system is then

$$KE = \frac{1}{2} M |v_{cm}|^2 + \frac{1}{2} \omega^T [I_{cm}] \omega.$$

Total potential energy of the system is

$$PE = PE_x + PE_y + PE_t + PE_s.$$

The Lagrangian of the system is $L = KE - PE$. Using Lagrange's equations, the linearized equations of motion for this system are obtained as

$$\ddot{\phi} = \frac{1}{I_{XX} l^3} \left(6 EI_y L X - 3 EI_y L l \phi - I_{XX} \Omega l^3 \dot{\theta} + I_{XX} \Omega^2 l^3 \phi - I_{ZZ} \Omega^2 l^3 \phi \right. \\ \left. + 6 EI_y l X - 4 EI_y l^2 \phi + I_{ZZ} \Omega^3 \dot{\theta} - I_{XX} \Omega l^3 \dot{\theta} \right), \quad (6.19)$$

$$\ddot{\theta} = -\frac{1}{I_{XX} l^3} \left(-I_{XX} \Omega l^3 \dot{\phi} - I_{XX} \Omega^2 l^3 \theta + I_{ZZ} \Omega l^3 \dot{\phi} + 4 EI_y l^2 \theta + I_{ZZ} \Omega^2 l^3 \theta \right. \\ \left. + 3 EI_y L l \theta - I_{XX} \Omega l^3 \dot{\phi} + 6 EI_y l Y + 6 EI_y L Y \right), \quad (6.20)$$

$$\ddot{X} = \frac{1}{2 I_{XX} M l^3} \left(2 I_{XX} M \Omega^2 l^3 X + 4 I_{XX} M \Omega l^3 \dot{Y} + I_{XX} M \Omega^2 L l^3 \phi + 12 I_{XX} EI_y l \phi \right. \\ \left. - 6 M L^2 EI_y X + 3 M L^2 EI_y l \phi - M L l^3 I_{XX} \Omega \dot{\theta} - 24 I_{XX} EI_y X - M L l^3 I_{XX} \Omega^2 \phi \right. \\ \left. + M L l^3 I_{ZZ} \Omega^2 \phi - 6 M L l EI_y X + 4 M L l^2 EI_y \phi - M L l^3 I_{ZZ} \Omega \dot{\theta} + M L l^3 I_{XX} \Omega \dot{\theta} \right), \quad (6.21)$$

$$\ddot{Y} = \frac{1}{2 M l^3 I_{XX}} \left(-24 EI_y I_{XX} Y - M \Omega L l^3 I_{XX} \dot{\phi} + M L I_{XX} \Omega^2 l^3 \theta - M L l^3 I_{ZZ} \Omega \dot{\phi} \right. \\ \left. - 4 M EI_y L l^2 \theta - M L I_{ZZ} \Omega^2 l^3 \theta - 3 M EI_y L^2 l \theta + M L I_{XX} \Omega l^3 \dot{\phi} - 6 M EI_y L l Y - 6 M EI_y L^2 Y \right. \\ \left. - 4 M I_{XX} \Omega l^3 \dot{X} + 2 M I_{XX} \Omega^2 l^3 Y - 12 I_{XX} EI_y l \theta - M I_{XX} \Omega^2 L l^3 \theta \right), \quad (6.22)$$

$$\ddot{\psi} = -\frac{G I_p \psi}{I_{ZZ} l}, \quad (6.23)$$

$$\ddot{Z} = -\frac{E A_c Z}{M l}. \quad (6.24)$$

Notice that the equations for ψ and Z are decoupled. Synchronous whirl, as seen in the rotating frame, involves no rates. Hence we set $\dot{\theta}$, $\dot{\phi}$, \dot{X} and \dot{Y} to zero in Eqs. 6.19 to 6.22. The determinant of the resulting coefficient matrix is set to zero to find the critical speed. This is the method used to solve for the critical speeds for beam-rigid-body examples considered in chapter 8. We will also use this method in our next analytical example.

6.4 A spinning torque free cylinder

6.4.1 Governing equations

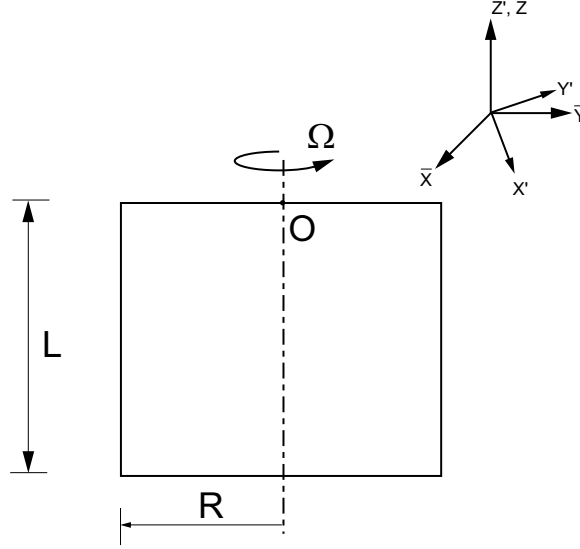


Figure 6.8: Spinning cylinder.

We now consider a rigid spinning cylinder. This is a simplified version of the beam cylinder model considered in section 6.3. There is no potential energy in this case. The equations of motion can be obtained by substituting $E = 0$ and taking $I_{XX} = \frac{MR^2}{4} + \frac{ML^2}{12}$ and $I_{ZZ} = \frac{MR^2}{2}$ in Eqs. 6.19 through 6.22 (we do not consider twist) as

$$\frac{d^2\theta}{dt^2} = \frac{\Omega \left(2L^2 \left(\frac{d\phi}{dt} \right) - 3\Omega R^2\theta + \Omega L^2\theta \right)}{3R^2 + L^2}, \quad (6.25)$$

$$\frac{d^2\phi}{dt^2} = -\frac{\Omega \left(3R^2\Omega\phi - \Omega L^2\phi + 2L^2 \left(\frac{d\theta}{dt} \right) \right)}{3R^2 + L^2}, \quad (6.26)$$

$$\frac{d^2X}{dt^2} = \frac{\Omega \left(-3LR^2 \left(\frac{d\theta}{dt} \right) + 3L\Omega R^2\phi + 2(3R^2 + L^2) \frac{dY}{dt} + \Omega(3R^2 + L^2)X \right)}{3R^2 + L^2}, \quad (6.27)$$

$$\frac{d^2 Y}{dt^2} = \frac{\Omega \left(-3 L R^2 \left(\frac{d\phi}{dt} \right) - 3 L \Omega R^2 \theta - 2 (3 R^2 + L^2) \frac{dX}{dt} + \Omega Y (3 R^2 + L^2) \right)}{3 R^2 + L^2}. \quad (6.28)$$

We will now obtain these equations using our formulation.

6.4.2 Torque free cylinder: prestress based formulation

We start with Eq. 4.5. We note that in this case the stress in the cylinder \mathbf{S}_1 is zero (rigid body mode). We will choose a rotating frame spinning at the rate Ω about the Z' axis and write the equations in this frame. \mathbf{S}_0 is taken to represent a rotating elastic cylinder in plane strain:

$$\mathbf{S}_0 = \begin{bmatrix} S_{0,xx} & S_{0,xy} & 0 \\ S_{0,xy} & S_{0,yy} & 0 \\ 0 & 0 & S_{0,zz} \end{bmatrix}, \quad (6.29)$$

where,

$$\begin{aligned} S_{0,xx} &= \frac{\rho \Omega^2 (y^2 + 2\nu y^2 - 3R^2 + 3x^2 + 2R^2\nu - 2\nu x^2)}{8(\nu - 1)}, \\ S_{0,yy} &= \frac{\rho \Omega^2 (3y^2 + 2\nu x^2 - 3R^2 + x^2 + 2R^2\nu - 2\nu y^2)}{8(\nu - 1)}, \\ S_{0,xy} &= \frac{-\rho \Omega^2 (2\nu - 1) xy}{4(\nu - 1)}, \\ S_{0,zz} &= \frac{\rho \Omega^2 \nu (-3R^2 + 2R^2\nu + 2x^2 + 2y^2)}{4(\nu - 1)}. \end{aligned}$$

Here ρ is the material density, ν is the Poisson's ration, R is the radius of the cylinder, and (x, y) are points on the cylinder measured in the rotating coordinate system. The displacement of a point on the cylinder is obtained by adding the displacements due to translation and rotation. We ignore the axial displacement and twist of the cylinder. Thus setting $Z = 0$ and $\psi = 0$ we get the displacement of a point (x, y, z) of the cylinder, viewed in the rotating coordinate system, as

$$\phi = \begin{Bmatrix} X \\ Y \\ 0 \end{Bmatrix} + R_2 R_1 \begin{Bmatrix} x \\ y \\ z \end{Bmatrix} - \begin{Bmatrix} x \\ y \\ z \end{Bmatrix},$$

where R_2 and R_1 are the rotation matrices as defined earlier in section 6.3. Since we are concerned with small motions about the equilibrium point we linearize immediately and obtain

$$\phi = \begin{Bmatrix} X + \phi z \\ Y - \theta z \\ -\phi x + \theta y \end{Bmatrix} \quad \text{and} \quad \nabla \phi = \begin{bmatrix} 0 & 0 & \phi \\ 0 & 0 & -\theta \\ -\phi & \theta & 0 \end{bmatrix}.$$

Choosing a virtual displacement $\delta \mathbf{w}$, virtual work gives

$$\int_V \left\{ \nabla \cdot \mathbf{S}_0 + \nabla \cdot (\nabla \phi \mathbf{S}_0) - \rho_0 \frac{\partial^2 \chi}{\partial t^2} \right\} \cdot \delta \mathbf{w} dV = 0. \quad (6.30)$$

The acceleration of a point (x, y, z) on the cylinder is given by

$$\frac{d^2 \chi}{dt^2} = \left. \frac{d^2 \phi}{dt^2} \right|_{\text{r.f.}} + 2\boldsymbol{\Omega} \times \left. \frac{d\phi}{dt} \right|_{\text{r.f.}} + \boldsymbol{\Omega} \times \boldsymbol{\Omega} \times (\mathbf{X} + \phi)$$

where \mathbf{X} is the position vector of the point under consideration and the subscript r.f. refers to the derivative taken in the rotating frame. The $\boldsymbol{\Omega} \times \boldsymbol{\Omega} \times \mathbf{X}$ part of the acceleration is balanced by $\nabla \cdot \mathbf{S}_0$ and these terms drop out of the equation. The remaining terms in acceleration simplify to

$$= \begin{Bmatrix} \frac{d^2 X}{dt^2} + z \frac{d^2 \phi}{dt^2} - 2\Omega \left(\frac{dY}{dt} - z \frac{d\theta}{dt} \right) - \Omega^2 (X + z\phi) \\ \frac{d^2 Y}{dt^2} - z \frac{d^2 \theta}{dt^2} + 2\Omega \left(\frac{dX}{dt} + z \frac{d\phi}{dt} \right) - \Omega^2 (Y - z\theta) \\ -x \frac{d^2 \phi}{dt^2} + y \frac{d^2 \theta}{dt^2} \end{Bmatrix}.$$

The virtual displacements are taken by choosing the variation of one generalized coordinate (out of X , Y , ϕ and θ) at a time and setting the remaining three variations to zero. For example, for variations in X , the virtual displacement is

$$\delta \mathbf{w} = [\delta X, 0, 0]^T.$$

Substituting this $\delta \mathbf{w}$ and the expressions for \mathbf{S}_0 , $\nabla \phi$ and $\frac{d^2 \chi}{dt^2}$ into Eq. 6.30, we get the following equation

$$\int_V \left(\rho \frac{d^2 X}{dt^2} + \rho \frac{d^2 \phi}{dt^2} - 2\Omega \rho \left(\frac{dY}{dt} - z \frac{d\theta}{dt} \right) - \rho \Omega^2 (X + z\phi) \right) \cdot \delta X dV = 0.$$

Carrying out the integration and using the arbitrariness of δX we get

$$L \frac{d^2 X}{dt^2} + L \frac{d^2 \phi}{dt^2} - 2\Omega \left(L \frac{dY}{dt} - \frac{L^2}{2} \frac{d\theta}{dt} \right) - \Omega^2 \left(XL + \frac{L^2}{2} \phi \right) = 0.$$

Similarly, substituting the other virtual displacements into Eq. 6.30 and carrying out the integration over the volume of the cylinder, we get four equations involving $\frac{d^2 X}{dt^2}$, $\frac{d^2 Y}{dt^2}$, $\frac{d^2 \theta}{dt^2}$ and $\frac{d^2 \phi}{dt^2}$. Solving these equations for the second derivatives we exactly recover Eqs. 6.25 to 6.28.

6.5 Foreshortening

A rod rotating like a helicopter blade, about an end point, shows an increase in its natural frequency due to a phenomenon called foreshortening. This has been treated, e.g., by Hodges [35]. Here we consider the same problem using our prestress based modal projection method and derive the governing differential equation.

A cantilever beam of length L is attached to a hub of radius R (see figure 6.9). It rotates about the center of the hub with an angular speed Ω . We are interested in the flapping mode of vibration, i.e., the lateral vibration in a plane perpendicular to the plane of rotation.

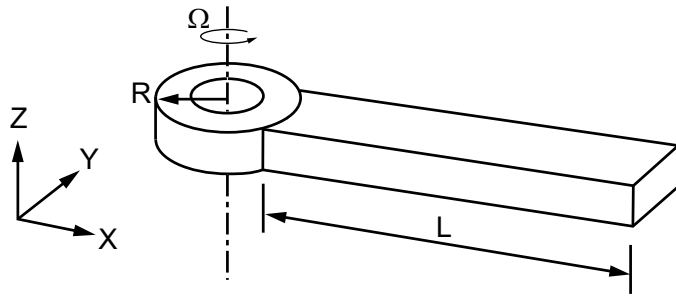


Figure 6.9: A rotating cantilever beam.

We again start with our governing equation, Eq. 4.5,

$$\nabla \cdot \mathbf{S}_0 + \nabla \cdot (\nabla \phi \mathbf{S}_0) + \nabla \cdot \mathbf{S}_1 = \rho \frac{\partial^2 \chi}{\partial t^2}.$$

We will write the equations in a frame rotating about the Z axis at the angular rate Ω . Choosing a coordinate system, attached to this rotating frame, as shown in figure 6.9, the prestress \mathbf{S}_0 due to rotation (about the Z axis) is

$$\mathbf{S}_0 = \begin{bmatrix} \frac{\rho \Omega^2 ((R+L)^2 - x^2)}{2} & 0 & 0 \\ 0 & 0 & 0 \\ 0 & 0 & 0 \end{bmatrix}.$$

Using Euler-Bernoulli assumptions, the displacement of a point at (x, y, z) is

$$\phi = \begin{Bmatrix} -z \frac{du}{dx} \\ 0 \\ u \end{Bmatrix} \quad \text{and hence} \quad \nabla \phi = \begin{bmatrix} -z \frac{d^2 u}{dx^2} & 0 & -\frac{du}{dx} \\ 0 & 0 & 0 \\ \frac{du}{dx} & 0 & 0 \end{bmatrix}.$$

The acceleration has two components: a centripetal component $\mathbf{a}_c = -\Omega^2 x$ along the X direction and the vibration component $\mathbf{a}_v = -\omega^2 u$ along the Z direction. The term $\nabla \cdot \mathbf{S}_0 = -\rho \Omega^2 x = -\rho \mathbf{a}_c$ and the two terms cancel out from the governing equation, which then reduces to

$$\nabla \cdot (\nabla \phi \mathbf{S}_0) + \nabla \cdot \mathbf{S}_1 = \rho \mathbf{a}_v.$$

Choosing a virtual displacement,

$$\delta \mathbf{w} = \begin{Bmatrix} -z \frac{d(\delta u)}{dx} \\ 0 \\ \delta u \end{Bmatrix},$$

virtual work gives

$$\int_V (\nabla \cdot (\nabla \phi \mathbf{S}_0) + \nabla \cdot \mathbf{S}_1 - \rho \mathbf{a}_v) \cdot \delta \mathbf{w} dV = 0. \quad (6.31)$$

Substituting the expressions for \mathbf{S}_0 , ϕ and $\nabla \phi$ into Eq. 6.31 we get

$$\begin{aligned} \int_V \left(\left(E + \frac{\rho \Omega^2}{2} ((R+L)^2 - x^2) \right) \frac{d^3 u}{dx^3} - \rho \Omega^2 x \frac{d^2 u}{dx^2} \right) z^2 \cdot \frac{d(\delta u)}{dx} \\ + \left(\frac{\rho \Omega^2}{2} ((R+L)^2 - x^2) \frac{d^2 u}{dx^2} - \rho \Omega^2 x \frac{du}{dx} + \rho \omega^2 u \right) \cdot \delta u dV = 0. \end{aligned}$$

The domain of the above integration is the volume V of the cantilever. This can be split into an integral over the area and an integral over the length. Thus the above integral becomes

$$\int_R^{R+L} \int_{\bar{A}} \left(\left(E + \frac{\rho \Omega^2}{2} ((R+L)^2 - x^2) \right) \frac{d^3 u}{dx^3} - \rho \Omega^2 x \frac{d^2 u}{dx^2} \right) z^2 \cdot \frac{d(\delta u)}{dx} \\ + \left(\frac{\rho \Omega^2}{2} ((R+L)^2 - x^2) \frac{d^2 u}{dx^2} - \rho \Omega^2 x \frac{du}{dx} + \rho \omega^2 u \right) \cdot \delta u d\bar{A} dx = 0,$$

where the integral over the length is taken from the base of the cantilever ($x = R$) to the tip ($x = R + L$). Taking A to be the area of cross section of the beam and using $\int_{\bar{A}} z^2 d\bar{A} = I_x$, the area moment of inertia of the cross section, the above integral simplifies to

$$\int_R^{R+L} \left(\left(E + \frac{\rho \Omega^2}{2} ((R+L)^2 - x^2) \right) \frac{d^3 u}{dx^3} - \rho \Omega^2 x \frac{d^2 u}{dx^2} \right) I_x \cdot \frac{d(\delta u)}{dx} \\ + \left(\frac{\rho \Omega^2}{2} ((R+L)^2 - x^2) \frac{d^2 u}{dx^2} - \rho \Omega^2 x \frac{du}{dx} + \rho \omega^2 u \right) A \cdot \delta u dx = 0.$$

Using integration by parts for the terms multiplying $\frac{d(\delta u)}{dx}$ and using the fact that at the boundaries either $\delta u = 0$ or $\frac{d^3 u}{dx^3} = \frac{d^2 u}{dx^2} = 0$ (no shear force or moment at the beam tip), the integral becomes

$$\int_R^{R+L} \left(- \left(E + \frac{\rho \Omega^2}{2} ((R+L)^2 - x^2) \right) I_x \frac{d^4 u}{dx^4} + 2\rho \Omega^2 I_x x \frac{d^3 u}{dx^3} + \rho \Omega^2 I_x \frac{d^2 u}{dx^2} \right. \\ \left. + \frac{\rho A \Omega^2}{2} ((R+L)^2 - x^2) \frac{d^2 u}{dx^2} - \rho A \Omega^2 x \frac{du}{dx} + \rho A \omega^2 u \right) \cdot \delta u dx = 0.$$

Now we make the following simplification. The coefficient of the term $I_x \frac{d^4 u}{dx^4}$ is

$$E + \underbrace{\frac{\rho \Omega^2}{2} ((R+L)^2 - x^2)}_A.$$

For typical materials, operating speeds and length of the cantilever beam, the Young's modulus $E \gg \rho \Omega^2 (R+L)^2$, hence we neglect the term marked A from the above expression.

Next, we compare the coefficients of the term $\frac{d^2 u}{dx^2}$:

$$\rho \Omega^2 I_x + \frac{\rho A \Omega^2}{2} ((R+L)^2 - x^2).$$

This can be written as

$$\rho \Omega^2 A (k^2 + (R + L)^2 - x^2),$$

where k is the radius of gyration of the cross section. Since $(R + L) \gg k$ for a beam geometry, we drop the term $\rho \Omega^2 I_x \frac{d^2 u}{dx^2}$ from our equation. Finally we consider the term $2\rho \Omega^2 I_x x \frac{d^3 u}{dx^3}$. Now since the displacement of the beam is usually a smooth and continuous function of the axial coordinate x , we have

$$\mathcal{O}\left(x \frac{d^3 u}{dx^3}\right) \approx \mathcal{O}\left(\frac{d^2 u}{dx^2}\right).$$

Thus the term $2\rho \Omega^2 I_x x \frac{d^3 u}{dx^3}$ is of the same order of magnitude as the term $\rho \Omega^2 I_x \frac{d^2 u}{dx^2}$ and hence we drop this term as well. Finally, we have

$$\int_R^{R+L} \left(-EI_x \frac{d^4 u}{dx^4} + \frac{\rho A \Omega^2}{2} ((R + L)^2 - x^2) \frac{d^2 u}{dx^2} - \rho A \Omega^2 x \frac{du}{dx} + \rho A \omega^2 u \right) \cdot \delta u dx = 0.$$

Since the variation δu is arbitrary, we get the governing equation of a rotating cantilever beam as

$$EI_x \frac{d^4 u}{dx^4} - \frac{\rho A \Omega^2}{2} ((R + L)^2 - x^2) \frac{d^2 u}{dx^2} + \rho A \Omega^2 x \frac{du}{dx} - \rho A \omega^2 u = 0. \quad (6.32)$$

In order to compare this equation with standard equations available in the literature, e.g., [35], we make a few change of variables. We define a nondimensionalized variable \bar{x} that is 0 at the root of the cantilever and 1 at its tip:

$$\bar{x} = \frac{x - R}{L},$$

Further we define

$$\bar{u} = \frac{u}{L}, \quad m = \rho A \quad \text{and} \quad \alpha = \frac{R}{L}.$$

Making these change of variables in Eq. 6.32 and rewriting we get

$$\frac{EI_x}{m\Omega^2 L^4} \bar{u}'''' - \frac{1}{2} (1 + 2\alpha - \bar{x}^2 - 2\alpha\bar{x}) \bar{u}'' + (\bar{x} + \alpha) \bar{u}' - \frac{\omega^2}{\Omega^2} \bar{u} = 0,$$

where (\prime) denotes differentiation with respect to \bar{x} . Using

$$\eta = \frac{EI_x}{m\Omega^2 L^4} \quad \text{and} \quad \mu = \frac{\omega^2}{\Omega^2},$$

and rewriting the above equation we finally get

$$\eta \bar{u}'''' - \left(\frac{1}{2} (1 - \bar{x}^2) \bar{u}' \right)' - \alpha ((1 - \bar{x}) \bar{u}') - \mu \bar{u} = 0,$$

which matches the governing equations as given by Eq. 1 in [35].

6.6 Concluding remarks

In this chapter we checked the validity of our formulation using different analytical examples. We initially solved some classical buckling problems using our formulation, which was originally derived for rotors. This showed the fundamental similarity between rotor whirl and buckling. Then, we solved two rotor whirl problems. The problems were chosen so that the gyroscopic effects were significant. The analytical match in each case proved that our formulation is correct and that the gyroscopic terms are indeed macroscopic manifestations of the effect of spin-induced prestress in the rotor. As a final example, and to show the versatility of our formulation, we derived the governing equation of a rotating cantilever. We now move on to another detailed analytical example; the problem of a spinning cylinder under axial load.

Chapter 7

Axially loaded cylindrical rotors

In this chapter we find the critical speed of a solid circular simply supported cylindrical rotor under axial load (see figure 7.1). It is a semi-analytical implementation of our approach in that we use analytical expressions for displacement fields in the virtual work calculation but solve the problem numerically. This problem has already been addressed by others using the one-dimensional Timoshenko approach [22].

Our formulation here has two key parts. One part is the spin-induced stress state in the non-whirling rotor, for which we use the elasticity solution for a long spinning circular rod, neglecting end effects. The other key part is the choice of the three dimensional displacement field in whirling, for applying the principle of virtual work. In this choice, nominal Timoshenko kinematics (wherein cross sections do not warp) gives incorrect results. An elasticity solution for a circular shaft under a transverse end load is, therefore, used to develop suitable expressions for three dimensional displacement fields.

Before we move on to the axially loaded rotor problem, we first solve the simpler problems of lateral vibrations and buckling of a simply supported cylinder. Subsequently, straightforward application of our formulation to the axially loaded spinning cylinder problem gives results that compare well against Timoshenko theory based formulas in [22]. We find only slight differences between the results, negligible for rotor lengths exceeding about five diameters. We also rediscover Cowper's [2] definition of the Timoshenko shear coefficient K .

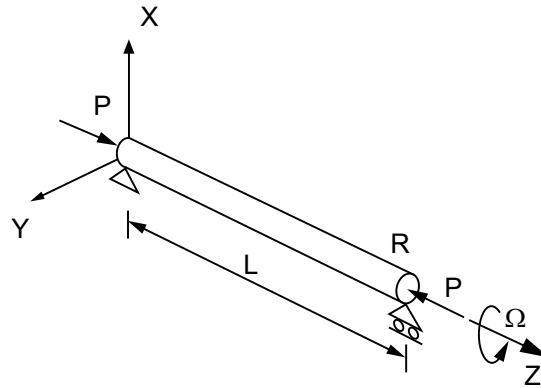


Figure 7.1: A solid circular rotor under axial load.

7.1 Nominal Timoshenko kinematics: no warping

In Timoshenko theory, plane sections remain plane after deformation. The deformation of the beam at each point is characterized by two variables: the lateral displacement u and the rotation ψ of the cross section. These are related as

$$\frac{du}{dz} = \chi + \psi, \quad (7.1)$$

where χ is the angle of shear of the cross section (see figure 7.2, where the material cross

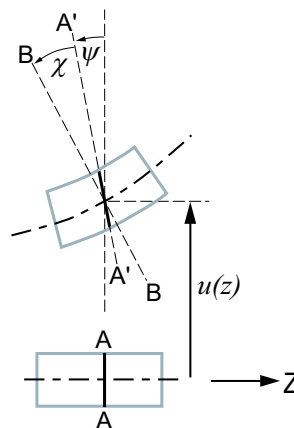


Figure 7.2: Nominal kinematics of a Timoshenko beam.

section AA rotates to A'A', and BB is the normal to the deformed centerline). Both u and ψ depend only on z . The displacement of a point located at a height x above the centroidal line, assuming bending in the X - Z plane, is given by

$$[u \quad 0 \quad -x\psi]^T. \quad (7.2)$$

The above non-warping kinematics, if used in our three dimensional formulation, gives significantly erroneous answers. We can obtain useful results if we do part of the calculation in three dimensions and the rest using Timoshenko beam-theory relations as was shown by us in [36]. Here, seeking a fully three dimensional calculation, we turn instead to a better choice of ϕ (with warping).

7.2 Kinematics from a 3D elasticity solution

7.2.1 Cylinder under a transverse end load

We first consider a solid cylindrical cantilever beam of length L and radius R , aligned with the Z direction, and with a net transverse centroidal end load W acting along the X direction. Assuming end conditions are consistent therewith, the displacements of a point (x, y, z) on the beam are given by [37]

$$\tilde{u} = \frac{W}{EI} \left(\frac{\nu}{2} (L-z) (x^2 - y^2) - \frac{z^3}{6} + \frac{Lz^2}{2} \right), \quad (7.3)$$

$$\tilde{v} = \frac{W}{EI} \nu (L-z) xy, \quad (7.4)$$

$$\tilde{w} = -\frac{W}{EI} \left(-\frac{3R^2x}{4} - \frac{\nu R^2x}{2} + \frac{xy^2}{4} + \frac{x^3}{4} + x \left(Lz - \frac{z^2}{2} \right) \right), \quad (7.5)$$

where E is Young's modulus, ν is Poisson's ratio, and I is $\pi R^4/4$.

7.2.2 3D kinematics for ϕ

The above solution applies for an end load only, while we need to write expressions for ϕ that will incorporate effects of, among other things, variable shear along the rotor. To this

end, let the lateral displacement averaged over the cross section be

$$U = \frac{W}{EI} \left(\frac{Lz^2}{2} - \frac{z^3}{6} \right) \quad (7.6)$$

and define

$$\psi = \frac{dU}{dz} - \frac{W}{AG}, \quad (7.7)$$

where $A = \pi R^2$ and G is the shear modulus. Observe here that, by direct computation using Eqs. 7.3 and 7.5, the average shear strain across the cross section is

$$\gamma = \frac{1}{A} \int_A \left(\frac{\partial \tilde{u}}{\partial z} + \frac{\partial \tilde{w}}{\partial x} \right) dA = \frac{W}{AG}, \quad (7.8)$$

whence ψ represents the cross section average of a quantity related to the rotation of the cross section (compare with the similar, but not identical, Eq. 7.1).

Now the right hand side of Eq. 7.3 contains a term with $W(L - z)$. Physically, in the 3D elasticity solution we are using, $W(L - z)$ is the bending moment at a cross section. Motivated by this, differentiation of Eq. 7.7 gives

$$\frac{W(L - z)}{EI} = \frac{d\psi}{dz}.$$

Using the above, the displacements 7.3, 7.4 and 7.5 can be rewritten in terms of U and ψ as

$$\tilde{u} = U + \frac{\nu}{2} (x^2 - y^2) \frac{d\psi}{dz}, \quad (7.9)$$

$$\tilde{v} = \nu xy \frac{d\psi}{dz}, \quad (7.10)$$

$$\tilde{w} = -x\psi + \frac{GA}{EI} \left(\frac{dU}{dz} - \psi \right) \left(\frac{R^2 x}{4} - \frac{xy^2}{4} - \frac{x^3}{4} \right). \quad (7.11)$$

The above three equations represent an exact solution from the theory of elasticity for constant W . However, if we *now* think of U and ψ therein as independent functions of z , then we have a three-dimensional kinematics in which each section has two degrees of freedom, and there is suitable (if not perfect) warping of cross sections. The difference between the set of Eqs. 7.9, 7.10 and 7.11 and the nominal Timoshenko kinematics given in Eq. 7.2 is crucial. We emphasize that U and ψ are now independent degrees of freedom at each z , and Eqs. 7.6 and 7.7 (which were used to motivate our choice of kinematics) no longer apply.

7.2.3 Connection with Cowper's shear factor K

Our three dimensional formulation has no need for the shear factor K used in Timoshenko beam theory, but we can make a connection with it here. In nominal Timoshenko kinematics plane sections remain plane without warping. Hence the displacement of a point along the Z direction is given by

$$u_z = -x\psi = -x \left(\frac{dU}{dz} - \chi \right), \quad (7.12)$$

where χ is the shear angle at a cross section.

From Eqs. 7.5 through 7.8,

$$\tilde{w} = -x \frac{dU}{dz} + \frac{\gamma}{2(1+\nu)R^2} (3R^2x + 2\nu R^2x - xy^2 - x^3), \quad (7.13)$$

where $\gamma = \left(\frac{dU}{dz} - \psi \right)$.

The best match between Eqs. 7.12 and 7.13 occurs when, in a suitably averaged sense,

$$\frac{\gamma}{2(1+\nu)R^2} (3R^2x + 2\nu R^2x - xy^2 - x^3) \approx x\chi.$$

Now in Timoshenko theory $\chi = \frac{W}{KAG}$, where K is the shear factor. By Eq. 7.8, we then have

$$\frac{\gamma}{2(1+\nu)R^2} (3R^2x + 2\nu R^2x - xy^2 - x^3) \approx x \frac{\gamma}{K},$$

which suggests that a best linear-in- x approximation of the left hand side is sought. Following the method of weighted residuals, multiplying both sides by x , integrating over the circular cross section, and equating both sides, we obtain

$$K = \frac{6 + 6\nu}{7 + 6\nu},$$

matching Cowper [2].

7.3 Results for lateral vibrations and buckling

Before studying the case of spin induced prestresses in whirling, we first see how Eqs. 7.9 through 7.11 work for lateral vibrations (no prestress) and buckling (no acceleration) as compared, for convenience, against Timoshenko theory.

7.3.1 Lateral vibrations

We use a straightforward assumed modes approach. In Eqs. 7.9 through 7.11 we substitute

$$U = a \sin\left(\frac{\pi z}{L}\right) \sin(\omega t) \quad \text{and} \quad \psi = b \cos\left(\frac{\pi z}{L}\right) \sin(\omega t), \quad (7.14)$$

where a and b are undetermined coefficients and ω is the natural frequency sought. This choice satisfies simply supported conditions.

Considering a laterally vibrating object. There is no prestress in this case. Hence the principle of virtual work applied to Eq. 4.5 with $\mathbf{S}_0 = 0$ gives

$$\int_V (\nabla \cdot \mathbf{S}_1 - \rho \mathbf{a}) \cdot \delta \mathbf{w} dV = 0, \quad (7.15)$$

where $\delta \mathbf{w}$ is an arbitrary virtual displacement. Using Eqs. 7.9 through 7.11, we take

$$\phi = \left\{ \begin{array}{c} U + \frac{\nu}{2} (x^2 - y^2) \frac{\partial \psi}{\partial z} \\ \nu xy \frac{\partial \psi}{\partial z} \\ -x\psi + \frac{GA}{EI} \left(\frac{R^2 x}{4} - \frac{xy^2}{4} - \frac{x^3}{4} \right) \left(\frac{\partial U}{\partial z} - \psi \right) \end{array} \right\} \quad (7.16)$$

and take $\delta \mathbf{w}$ as simply ϕ with U and ψ replaced by δU and $\delta \psi$ respectively. The acceleration is

$$\mathbf{a} = \left\{ \begin{array}{c} \frac{\partial^2 U}{\partial t^2} + \frac{\nu}{2} (x^2 - y^2) \frac{\partial^3 \psi}{\partial z \partial t^2} \\ \nu xy \frac{\partial^3 \psi}{\partial z \partial t^2} \\ -x \frac{\partial^2 \psi}{\partial t^2} + \frac{GA}{EI} \left(\frac{R^2 x}{4} - \frac{xy^2}{4} - \frac{x^3}{4} \right) \left(\frac{\partial^3 U}{\partial z \partial t^2} - \frac{\partial^2 \psi}{\partial t^2} \right) \end{array} \right\}. \quad (7.17)$$

Substituting Eq. 7.14 into Eqs. 7.16 and 7.17, and then using Eq. 7.15, we get a 2×2 eigenvalue problem for ω . The smaller frequency, nondimensionalized, is plotted in figure 7.3 against L/D (where $D = 2R$ is the diameter). Corresponding predictions of Timoshenko beam theory are plotted for comparison. The match is good¹.

¹This same virtual work calculation with nominal Timoshenko kinematics gives nonsensical results, independent of R . Useful results with nominal Timoshenko kinematics could be obtained *via* Lagrange's equations, but our interest here is in the prestress-based formulation of chapter 4

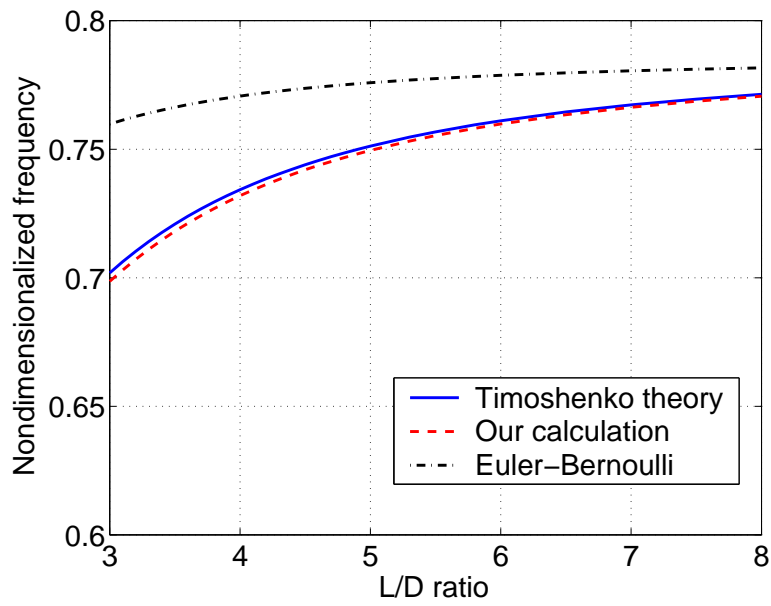


Figure 7.3: Nondimensionalized natural frequency ($\omega_n/\bar{\Omega}$) of a simply supported cylinder, plotted against L/D . Here $\bar{\Omega} = 2\pi\sqrt{ER^2/\rho L^4}$. For Timoshenko theory, we used $K = (6 + 6\nu)/(7 + 6\nu)$ [2]. For numerical calculation, we used $R = 0.25$ m, $E = 210$ GPa, $\nu = 0.25$ and $\rho = 7800$ Kg/m³.

7.3.2 Buckling load of a simply supported cylinder

As above, we will compare with Timoshenko theory. To this end, we note that there are two ways to estimate the buckling load of a Timoshenko beam [28]. In one method (we call this method 1) the shear force is resolved on a cross section perpendicular to the deformed centroidal line. The buckling load from this formulation is ([28], pp. 133, Eq. 2.57)

$$P_{cr} = \frac{P_e}{1 + P_e/KAG}, \quad (7.18)$$

where $P_e = \frac{\pi^2 EI}{L^2}$. In the other method (we call this method 2) the shear force is resolved along a physical or material cross section which was originally perpendicular to the undeformed centroidal line. The critical buckling load from this formulation is ([28], pp. 135, Eq. 2.59)

$$P_{cr} = \frac{\sqrt{1 + 4P_e/KAG} - 1}{2/KAG}. \quad (7.19)$$

We now calculate the buckling load using our three dimensional kinematics. Virtual work applied to Eq. 4.5 with acceleration set to zero gives

$$\int_V (\nabla \cdot \nabla \phi \mathbf{S}_0 + \nabla \cdot \mathbf{S}_1) \cdot \delta \mathbf{w} dV = 0. \quad (7.20)$$

The only nonzero component of prestress \mathbf{S}_0 in this case is $S_{0,zz} = -P/A$. Hence

$$\mathbf{S}_0 = \begin{bmatrix} 0 & 0 & 0 \\ 0 & 0 & 0 \\ 0 & 0 & -P/A \end{bmatrix}. \quad (7.21)$$

Using Eq. 7.16 for ϕ , and using Eq. 7.14 without the $\sin \omega t$ for U and ψ in the virtual work Eq. 7.20, we solve for the buckling load P . Figure 7.4 compares our results with Timoshenko methods 1 and 2. Although method 2 is expected to be more accurate as per the discussion in [28], our results are closer to those from method 1. However, for $L/D \geq 5$ all three results are close.

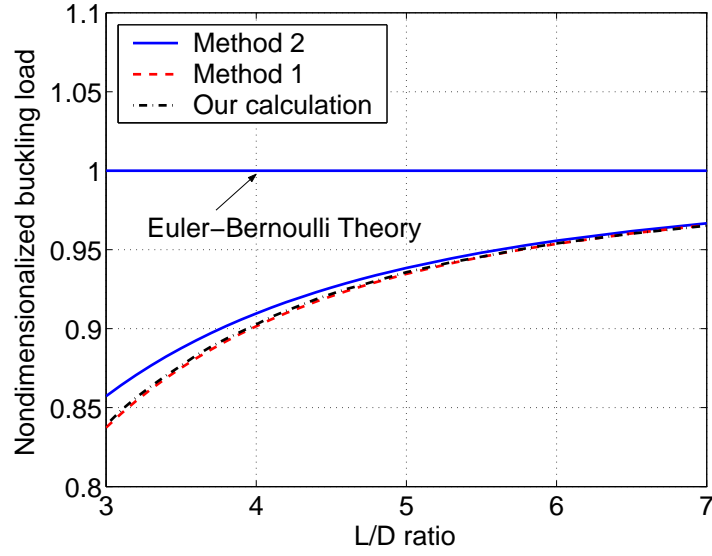


Figure 7.4: Nondimensionalized buckling load P/P_e of a cylinder plotted against L/D . Here $P_e = \frac{\pi^2 EI}{L^2}$. For Timoshenko theory we used $K = (6 + 6\nu)/(7 + 6\nu)$. For numerical calculations we used $R = 0.25$ m, $E = 210$ GPa, $\nu = 0.25$ and $\rho = 7800$ Kg/m³.

7.4 Critical speed of a simply supported, axially loaded, cylinder

We finally consider the problem of primary interest in this chapter, namely the first critical speed of a simply supported, axially loaded, cylinder. For synchronous whirl at the critical speed, the acceleration \mathbf{a} is equal to $\boldsymbol{\Omega} \times \boldsymbol{\Omega} \times (\mathbf{r} + \boldsymbol{\phi})$, where \mathbf{r} is the position vector of the point under consideration (with origin on the rotation axis). The prestress is composed of two parts: $\mathbf{S}_0 = \mathbf{S}_{0,spin} + \mathbf{S}_{0,axial}$. Noting that $\nabla \cdot \mathbf{S}_{0,axial} = 0$ since the axial load is constant and $\nabla \cdot \mathbf{S}_{0,spin} = \rho (\boldsymbol{\Omega} \times \boldsymbol{\Omega} \times \mathbf{r})$, virtual work gives

$$\int_V (\nabla \cdot \nabla \phi \mathbf{S}_0 + \nabla \cdot \mathbf{S}_1 - \rho (\boldsymbol{\Omega} \times \boldsymbol{\Omega} \times \boldsymbol{\phi})) \cdot \delta \mathbf{w} dV = 0. \quad (7.22)$$

The prestress $\mathbf{S}_{0,axial}$ is again given by Eq. 7.21, the same as in section 7.3.2. The prestress $\mathbf{S}_{0,spin}$ in this case is taken as the stress in a spinning cylinder under constant axial strain such that the average axial stress across the section is zero. The nonzero components of

$\mathbf{S}_{0,spin}$ are

$$S_{0,xx} = \frac{\rho\Omega^2 (y^2 + 2\nu y^2 - 3R^2 + 3x^2 + 2R^2\nu - 2\nu x^2)}{8(\nu - 1)},$$

$$S_{0,yy} = \frac{\rho\Omega^2 (3y^2 + 2\nu x^2 - 3R^2 + x^2 + 2R^2\nu - 2\nu y^2)}{8(\nu - 1)},$$

$$S_{0,xy} = \frac{-\rho\Omega^2 (2\nu - 1)xy}{4(\nu - 1)},$$

$$S_{0,zz} = \frac{\rho\Omega^2\nu (-3R^2 + 2R^2\nu + 2x^2 + 2y^2)}{4(\nu - 1)} - \frac{\nu\rho\Omega^2 R^2}{2}.$$

In the above, dropping the last term of the last equation gives the well known plane strain solution for a spinning cylinder.

We again use Eq. 7.16 for ϕ and Eq. 7.14 (without the $\sin\omega t$) for U and ψ . Substituting these into the virtual work equation (Eq. 7.22) we get an eigenvalue problem that can be solved for the critical speed. The results for several L/D ratios are compared with corresponding numerical solutions from Choi *et al.*'s formulation, which uses what we called method 2 above in figure 7.5. Also plotted are the critical speeds obtained using an alternative formulation based on what we called method 1 above. Our results are, again, closer to those from method 1.

7.5 Concluding remarks

In this chapter we have analytically demonstrated the applicability of our formulation to the case of a rotating cylinder under axial load. We have compared our answers with results obtained using Timoshenko theory, which accurately models the system considered.

An important aspect of this study is the key role played by the assumed underlying three dimensional kinematics in the present rotor formulation. Nominal (non-warping) Timoshenko kinematics used with our formulation leads to large errors and is unsuitable for this problem. Hence a better 3D kinematics with warping of cross sections was developed from a suitable elasticity solution for a cylinder under a transverse end load. This kinematics was shown to perform very well.

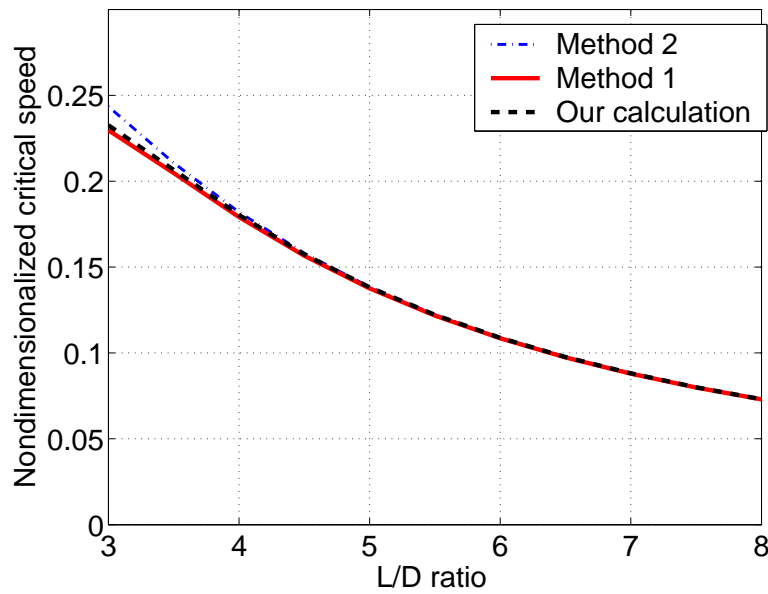


Figure 7.5: Nondimensionalized critical speed ($\Omega_c/\bar{\Omega}$) of a simply supported cylinder plotted against L/D . The axial load applied is $P = 0.7 \frac{\pi^2 EI}{L^2}$ in each case. $\bar{\Omega} = 2\pi \sqrt{ER^2/\rho L^4}$. $K = (6 + 6\nu)/(7 + 6\nu)$. For numerical calculations we used $R = 0.25$ m, $E = 210$ GPa, $\nu = 0.25$ and $\rho = 7800$ Kg/m³.

Another interesting aspect of our results is that they seem closer to the first method of studying buckling and whirling of Timoshenko rotors, while the second method is expected to be more accurate. Differences between results from these methods and ours are, however, negligible for $L/D \geq 5$. Better choice of kinematics may lead to a match with method 2.

Chapter 8

Numerical examples

In this chapter we demonstrate the numerical computation of critical speeds of arbitrary shaped rotors using our formulation and modal projection methods. We consider six axisymmetric and one asymmetric geometry. The results predicted by our method are compared against analytical results, when available, or against a detailed load-stepping based calculation using ANSYS (chapter 2) and a direct nonlinear finite element method (appendix A).

8.1 Results for axisymmetric geometries

We consider six different axisymmetric rotor geometries as shown in figure 8.1. The relevant geometrical dimensions are

- (a) Cylinder, $L = 2$ m, $D = 0.5$ m.
- (b) Truncated cone, $L = 2$ m, $D = 0.5$ m, $d = 0.2$ m.
- (c) Bottle, $L = 1.0$ m, $h = 0.3$ m, $D_1 = 0.5$ m, $D_2 = 0.45$ m, $d = 0.2$ m.
- (d) Beam-Cylinder, $L_1 = 0.1$ m, $d = 0.003$ m, $L_2 = 0.5$ m, $D = 1.0$ m.
- (e) Shell, $L_1 = 0.1$ m, $d = 0.003$ m, $L_2 = 0.3$ m, $D_1 = 1.6$ m, $D_2 = 0.8$ m, $D_3 = 0.8$ m, $t = 0.03$ m, $t_1 = 0.025$ m.

- (f) Bell, $L_1 = 0.1$ m, $d = 0.003$ m, $L_2 = 0.8$ m, $D_1 = 1.8666$ m, $D_3 = 0.8$ m, $t = 0.0416$ m, $t_1 = 0.025$ m.

The material properties specified are: Young's modulus = 210 GPa, Poisson's ratio = 0.25, density = 7,800 kg/m³. The first two rotors are modeled as having simply supported end faces, approximately implemented in the finite element model by restricting endface nodes to have axial displacements only; the last four have their left faces fully fixed, with no other restraints.

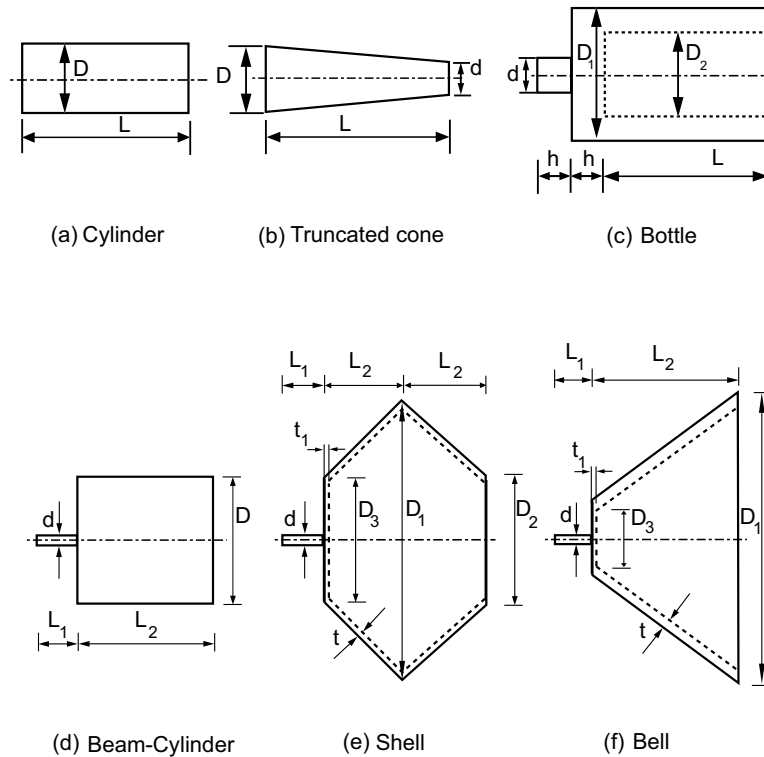


Figure 8.1: Rotor geometries considered.

From the first modal projection method, we recall the first integral in Eq. 5.2 (a surface term). A rough numerical estimate of this term, for the first rotor, worked out to only about 8% of the second term in Eq. 5.2, and so a more accurate integration was not carried out; and this surface term was dropped entirely for the second rotor. For the remaining four rotors, the surface term is zero¹.

¹Our implementation of simple supports for the first two rotors, through restricting endface displacements to be purely axial, causes artificial endface tractions when the rotor spins. An alternative modeling




Rotor	ω_f rad/s	Critical speed Ω_c				
		ANSYS (chap. 2)	Our code (appendix A)	Analytical (if known)	Method 1 (sec. 4.3)	Method 2 (sec. 5.3)
 Cylinder	1498.73	1548.9	1546.46	1545.38	1544.96 (1546.76)	1544.63
 Cone	969.13	990.70	991.48	–	990.38	990.20
 Bottle	362.97	381.18	380.05	–	380.18	380.12

Table 8.1: Comparison of critical speeds from various methods. All speeds in rad/s. Note that the difference between bending and whirling frequencies is relatively small (e.g., about 3% for the cylinder). Nevertheless, this small *difference* is captured to within about 4%.

Predicted whirling speeds from the two modal projections described above as well as from verifying calculations done using both ANSYS (see chapter 2) as well as our own nonlinear finite element code (see appendix A), for three of the six geometries, are given in table 8.1.

For the cylinder (simply supported), Timoshenko theory is applicable, and the formula of Zu and Han [38] with shear factor 0.9 gives a first mode bending frequency of 1497.52 rad/s; this matches our ω_f in the table (from ANSYS) very well. The critical speed of the cylinder from the analytical formula [38] is 1545.38 rad/s. This compares well with the critical speeds obtained from all the methods. Among these, the result from our code (1546.46) is here taken as the most accurate. The result from modal projection method 1, not including the boundary term of Eq. 5.2, is slightly lower and is close to the result from method 2, to which it is equivalent. Including the surface term in method 1, we obtain the value in parentheses (1546.76), more closely matching our nonlinear code.

For the truncated cone, too, there are similarly small boundary terms, which we have dropped; results obtained resemble those for the cylinder.

approach might be to allow the rotors to spin up without constraints, and to apply the simple support conditions only for subsequent bending. The surface terms would then be zero for the first two rotors as well.

For the bottle (as for the remaining 3 rotors), the boundary terms of Eq. 5.2 are known to be zero, because all points on the left faces of the rotors are held fixed in all three directions.

The laborious load-stepping calculations of ANSYS (as described in section 2.1) are slightly compromised due to the finite-sized imperfections used, and are presented here only to ensure that the results from other methods are good. These calculations were only carried out for the first three rotors. Also, only these same three rotors were studied using our own code, which retains *all* terms while our interest here has been to identify the key terms necessary so that simple modal projections will yield a good answer.

We now turn to the remaining three rotors. These extreme geometries involve dynamics where the bulk of the mass moves like a rigid body, and essentially all deformations are restricted to narrow neck regions of negligible mass. These narrow necks may, for analytical estimates, be thought of as massless beams, and the rest of the rotors thought of as rigid bodies. The corresponding rigid body dynamics analysis has already been presented in section 6.3. The final numerical results from those analyses are used here for cross-checking.

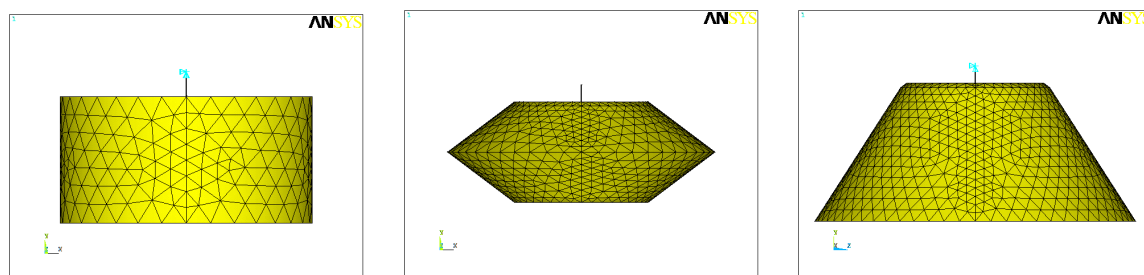


Figure 8.2: Meshes for beam-rigid-body models (10 noded tetrahedral elements).

The results obtained are given in table 8.2. All modal projections in this table were done with 2 modes (actually, 4 modes in ANSYS, with 2 modes for each frequency due to symmetry). Figure 8.2 shows the mesh used for analysing these geometries.

For each geometry, natural frequencies ω_f as obtained from ANSYS are given in the table, with the second beam-bending mode frequencies in parentheses. In each case,




Rotor	ω_f rad/s	Critical speeds Ω_c		
		Analytical (sec. 6.3) (Approximate)	Method 1 (sec. 4.3)	Method 2 (sec. 5.3)
 Beam Cyl.	0.125 (2.62)	0.234 $1.98i$	0.234 $1.96i$	0.234 –
 Shell	0.171 (4.06)	$0.477i$ 1.73	$0.462i$ 1.76	– 1.72
 Bell	0.109 (3.63)	0.330 $1.55i$	0.334 $1.51i$	0.330 –

Table 8.2: Comparison of critical speeds from various methods. All speeds in rad/s. Modal projections performed with two modes. The geometric properties of the rotor (mass moment of inertia matrix, center of mass), required for the analytical evaluation of the critical speed using the method discussed in section 6.3, were obtained using ANSYS.

there are two lateral vibration modes, but only one corresponding whirling mode. It is also interesting to note that the whirl speed is approximately two, ten, and three times the first bending frequencies for the three rotors, respectively; that is, the differences between the non-spinning vibration frequencies and the whirl frequencies are large. We note that analytical estimates and modal projections give comparable but not identical results, especially for the last two geometries; this is probably because one of them involves external calculation of deformation gradients and the other does not, and so the calculations differ in detail; and possibly because one involves mode shapes without prestress, and the other involves mode shapes with prestress. The prestress based calculations are limited to seeking real solutions only, and fail to capture the imaginary solutions (suppressed modes). Overall, agreement is good.

Finally, a note on the imaginary critical speeds that have been obtained in the case of beam rigid body models. These represent potential whirling modes that have been suppressed due to gyroscopic effects. For example, consider again Ewins's rotor of section

6.2. The critical speed for this rotor was calculated as

$$\Omega_c = \sqrt{\frac{k}{M(1 - R^2/4L^2)}}.$$

If the radius $R > 2L$, then the critical speed for this rotor becomes imaginary.

8.2 An asymmetric rotor example

We now calculate the critical speed of an asymmetric rotor using our modal projection method 1. The rotor is taken to have a uniform scalene triangle cross-section with the axis of spin passing through the centroid of the cross-section. The rotor is 4.0 m long and the length of the sides of the triangle are 1.0 m, 0.5385 m and 0.9434 m respectively. The Young's modulus is 210 GPa, Poisson's ratio is 0.25 and the density is 7800 Kg/m³. The rotor is simply supported at both the ends and this is again enforced by constraining the in-plane displacements of all the nodes on both end faces. One node on one of the faces is further fixed in the axial direction to avoid rigid body modes. Ten noded tetrahedral elements are again used for the mesh (see figure 8.3 left for details). The natural frequency of the fundamental mode is calculated using ANSYS as 341.89 rad/s. The fundamental bending mode is shown on the right of figure 8.3.

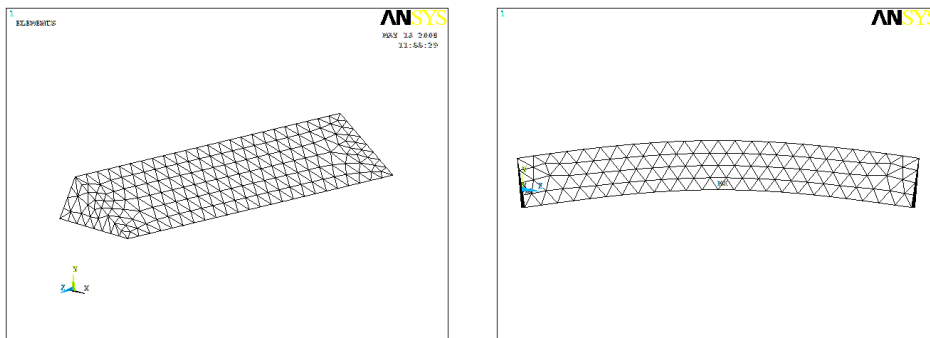


Figure 8.3: Left: mesh of the scalene triangular cylinder. Right: first mode shape.

The critical speed calculated using the two modal projections are compared with that obtained using the laborious calculation in ANSYS (chapter 2) as well as our in-house

Method	Critical Speed
Modal Projection 1	344.67
Modal Projection 2	344.65
ANSYS (Chapter 2)	345.10
ANSYS (run with four times smaller imperfection)	344.48
Our Code (Chapter 9)	344.42

Table 8.3: Triangular cross-sectioned rotor: comparison of critical speeds obtained using different methods. All speeds in rad/s.

code (Chapter 9). The results are given in table 8.3. Note that the surface term discussed in section 5.1 has again been dropped from our calculation.

8.3 Concluding remarks

In this chapter we have used our modal projection methods to numerically compute the critical speeds of seven different rotor geometries including an asymmetric geometry. The results obtained provide further support for the formulation and also indicate how the formulation can be done numerically.

Chapter 9

Nonlinear finite element calculation

In this chapter we describe a nonlinear finite element calculation based on isoparametric elements for finding the critical speed of arbitrary shaped rotors. This method, itself new for rotor applications, is developed primarily to check the results obtained using our modal projection method.

9.1 Isoparametric nonlinear finite element solution

Our direct nonlinear analysis follows the approach and notation of Jog and Kelkar [39] (except that they used hybrid elements; see appendix A). The strategy for this specific rotor whirl application is to write equations in a *rotating* coordinate system; to compute the nonlinear spin-induced expansion solution (in a 3-dimensional setting) as a function of rotation speed; and to identify the particular speed at which new solutions exist which also satisfy the governing equations. In other words, we seek the speed at which the whirling solution bifurcates from the straight solution.

We now briefly describe the strong form of the governing equations and the displacement based variational formulation that is used to derive the finite element equations. All the equations are written with respect to the reference configuration V whose boundary Γ is composed of two open, disjoint regions, $\Gamma = \overline{\Gamma_u \cup \Gamma_t}$. Γ_u is the region where the displacement is specified and Γ_t is the region where traction is specified. The spatial variables in the

reference and deformed configurations are denoted by \mathbf{X} and \mathbf{x} , respectively, and within the context of the static problems that we consider in this work, we assume a one-to-one mapping χ that takes \mathbf{X} to \mathbf{x} , i.e., $\mathbf{x} = \chi(\mathbf{X}) = \mathbf{X} + \mathbf{u}$, where \mathbf{u} is the displacement field. The deformation gradient is given by $\mathbf{F} := \nabla \chi = \mathbf{I} + \nabla \mathbf{u}$, where the gradient is with respect to the material coordinates \mathbf{X} .

We consider the following boundary value problem:

Find the displacements \mathbf{u} , second-Piola Kirchhoff stress \mathbf{S} , Green strain \mathbf{E} and tractions \mathbf{t}^0 , such that

$$\nabla \cdot (\mathbf{F}\mathbf{S}) + \rho_0 \mathbf{b}^0 = \mathbf{0} \quad \text{on } V, \quad (9.1)$$

$$\mathbf{E} = \hat{\mathbf{E}}(\mathbf{S}) \quad \text{on } V, \quad (9.2)$$

$$\mathbf{E} = \bar{\mathbf{E}}(\mathbf{u}) := \frac{1}{2}[(\nabla \mathbf{u}) + (\nabla \mathbf{u})^T + (\nabla \mathbf{u})^T(\nabla \mathbf{u})] \quad \text{on } V, \quad (9.3)$$

$$\mathbf{t}^0 = \mathbf{F}\mathbf{S}\mathbf{n}^0 \quad \text{on } \Gamma, \quad (9.4)$$

$$\mathbf{t}^0 = \bar{\mathbf{t}}^0, \quad \text{on } \Gamma_t \quad (9.5)$$

$$\mathbf{u} = \mathbf{0}, \quad \text{on } \Gamma_{\mathbf{u}}, \quad (9.6)$$

where $\rho_0 = (\det \mathbf{F})\rho$ is the density in the reference configuration in terms of the density ρ in the deformed configuration, \mathbf{n}^0 is the outward normal to Γ , $\mathbf{t}^0 := \|\mathbf{cof} \mathbf{F}\| \mathbf{t}$ are the tractions defined on the reference configuration in terms of the actual tractions \mathbf{t} on the deformed configuration, and $\mathbf{b}^0(\mathbf{X}) := \mathbf{b}(\chi(\mathbf{X})) = \rho \Omega^2(\tilde{\mathbf{X}} + \tilde{\mathbf{u}})$ is the body force field on the reference configuration, where $\tilde{\mathbf{X}}$ and $\tilde{\mathbf{u}}$ are obtained by excluding the angular velocity direction component from \mathbf{X} and \mathbf{u} , respectively (if the rotor nominally spins about the Z -axis, this means the Z -component of these vectors is set to zero). We emphasize that Eq. 9.2 does not imply that the stress-strain relation $\mathbf{S} = \hat{\mathbf{S}}(\mathbf{E})$ needs to be analytically inverted – numerical inversion is acceptable.

The displacement based variational principle on which our finite element formulation is based (here is where we depart from [39]) enforces Eqs. 9.1 and 9.5, and Eq. 9.3 in a weak sense. Thus, if

$$\mathcal{V}_u := \{\mathbf{u}_\delta : \mathbf{u}_\delta = \mathbf{0} \quad \text{on } \Gamma_{\mathbf{u}}\}$$

denotes the space of variations of the displacements, the variational formulation (after carrying out an appropriate integration by parts of the first variational statement) is given by

$$\int_V \mathbf{S} : \bar{\mathbf{E}}_\delta dV = \int_V \rho_0 \mathbf{u}_\delta \cdot \mathbf{b}^0 dV + \int_{\Gamma_t} \mathbf{u}_\delta \cdot \mathbf{t}^0 d\Gamma \quad \forall \mathbf{u}_\delta \in \mathcal{V}_u, \quad (9.7)$$

where $\bar{\mathbf{E}}$ is given by Eq. 9.3, and its variation $\bar{\mathbf{E}}_\delta$ is given by

$$\bar{\mathbf{E}}_\delta(\mathbf{u}, \mathbf{u}_\delta) = \frac{1}{2} [(\nabla \mathbf{u}_\delta) + (\nabla \mathbf{u}_\delta)^T + (\nabla \mathbf{u})^T (\nabla \mathbf{u}_\delta) + (\nabla \mathbf{u}_\delta)^T (\nabla \mathbf{u})].$$

To develop an iterative finite element scheme, we now linearize the variational statements in Eq. 9.7. The superscripts k and $k+1$ will now be used to denote the values of the field variables at the k and $k+1^{\text{th}}$ iterative steps, and let \mathbf{u}_Δ denote the increments in the displacement and stress fields.

$$\begin{aligned} (\mathbf{S} : \bar{\mathbf{E}}_\delta)^{k+1} &\approx (\mathbf{S} : \bar{\mathbf{E}}_\delta)^k + D_u (\mathbf{S} : \bar{\mathbf{E}}_\delta) (\mathbf{u}^k) [\mathbf{u}_\Delta] \\ &= (\mathbf{S} : \bar{\mathbf{E}}_\delta)^k + \frac{1}{2} \mathbf{S} : [(\nabla \mathbf{u}_\delta)^T (\nabla \mathbf{u}_\Delta) + (\nabla \mathbf{u}_\Delta)^T (\nabla \mathbf{u}_\delta)] \\ &= (\mathbf{S} : \bar{\mathbf{E}}_\delta)^k + \mathbf{S} : [(\nabla \mathbf{u}_\delta)^T (\nabla \mathbf{u}_\Delta)] \\ &= (\mathbf{S} : \bar{\mathbf{E}}_\delta)^k + [(\nabla \mathbf{u}_\delta) \mathbf{S}] : (\nabla \mathbf{u}_\Delta). \end{aligned}$$

For computer implementation, it is convenient to express second-order tensors as vectors and fourth order tensors as matrices. Hence we define

$$\mathbf{S}_c = \begin{bmatrix} S_{11} \\ S_{22} \\ S_{33} \\ S_{12} \\ S_{23} \\ S_{13} \end{bmatrix}; \quad (\nabla \mathbf{u}_\Delta)_c = \begin{bmatrix} (\nabla \mathbf{u}_\Delta)_{11} \\ (\nabla \mathbf{u}_\Delta)_{12} \\ (\nabla \mathbf{u}_\Delta)_{13} \\ (\nabla \mathbf{u}_\Delta)_{21} \\ (\nabla \mathbf{u}_\Delta)_{22} \\ (\nabla \mathbf{u}_\Delta)_{23} \\ (\nabla \mathbf{u}_\Delta)_{31} \\ (\nabla \mathbf{u}_\Delta)_{32} \\ (\nabla \mathbf{u}_\Delta)_{33} \end{bmatrix}.$$

Further we define

$$[\bar{\mathbf{E}}_\delta(\mathbf{u}^k)]_c = \left\{ D\bar{\mathbf{E}}(\mathbf{u}^k)[\mathbf{u}_\delta] \right\}_c = \begin{bmatrix} (\nabla \mathbf{u}_\delta)_{11} + (\nabla \mathbf{u}^k)_{i1} (\nabla \mathbf{u}_\delta)_{i1} \\ (\nabla \mathbf{u}_\delta)_{22} + (\nabla \mathbf{u}^k)_{i2} (\nabla \mathbf{u}_\delta)_{i2} \\ (\nabla \mathbf{u}_\delta)_{33} + (\nabla \mathbf{u}^k)_{i3} (\nabla \mathbf{u}_\delta)_{i3} \\ (\nabla \mathbf{u}_\delta)_{12} + (\nabla \mathbf{u}_\delta)_{21} + (\nabla \mathbf{u}^k)_{i1} (\nabla \mathbf{u}_\delta)_{i2} + (\nabla \mathbf{u}^k)_{i2} (\nabla \mathbf{u}_\delta)_{i1} \\ (\nabla \mathbf{u}_\delta)_{23} + (\nabla \mathbf{u}_\delta)_{32} + (\nabla \mathbf{u}^k)_{i2} (\nabla \mathbf{u}_\delta)_{i3} + (\nabla \mathbf{u}^k)_{i3} (\nabla \mathbf{u}_\delta)_{i2} \\ (\nabla \mathbf{u}_\delta)_{13} + (\nabla \mathbf{u}_\delta)_{31} + (\nabla \mathbf{u}^k)_{i1} (\nabla \mathbf{u}_\delta)_{i3} + (\nabla \mathbf{u}^k)_{i3} (\nabla \mathbf{u}_\delta)_{i1} \end{bmatrix},$$

with the summation over i implied. The stress matrix is defined as

$$\mathbf{S}_M = \begin{bmatrix} S_{11} & S_{12} & S_{13} & 0 & 0 & 0 & 0 & 0 & 0 \\ S_{12} & S_{22} & S_{23} & 0 & 0 & 0 & 0 & 0 & 0 \\ S_{13} & S_{23} & S_{33} & 0 & 0 & 0 & 0 & 0 & 0 \\ 0 & 0 & 0 & S_{11} & S_{12} & S_{13} & 0 & 0 & 0 \\ 0 & 0 & 0 & S_{12} & S_{22} & S_{23} & 0 & 0 & 0 \\ 0 & 0 & 0 & S_{13} & S_{23} & S_{33} & 0 & 0 & 0 \\ 0 & 0 & 0 & 0 & 0 & 0 & S_{11} & S_{12} & S_{13} \\ 0 & 0 & 0 & 0 & 0 & 0 & S_{12} & S_{22} & S_{23} \\ 0 & 0 & 0 & 0 & 0 & 0 & S_{13} & S_{23} & S_{33} \end{bmatrix},$$

and the engineering form of the material constitutive tensor as

$$\mathbf{C}_c = \begin{bmatrix} \mathbb{C}_{1111} & \mathbb{C}_{1122} & \mathbb{C}_{1133} & \mathbb{C}_{1112} & \mathbb{C}_{1123} & \mathbb{C}_{1113} \\ \mathbb{C}_{2211} & \mathbb{C}_{2222} & \mathbb{C}_{2233} & \mathbb{C}_{2212} & \mathbb{C}_{2223} & \mathbb{C}_{2213} \\ \mathbb{C}_{3311} & \mathbb{C}_{3322} & \mathbb{C}_{3333} & \mathbb{C}_{3312} & \mathbb{C}_{3323} & \mathbb{C}_{3313} \\ \mathbb{C}_{1211} & \mathbb{C}_{1222} & \mathbb{C}_{1233} & \mathbb{C}_{1212} & \mathbb{C}_{1223} & \mathbb{C}_{1213} \\ \mathbb{C}_{2311} & \mathbb{C}_{2322} & \mathbb{C}_{2333} & \mathbb{C}_{2312} & \mathbb{C}_{2323} & \mathbb{C}_{2313} \\ \mathbb{C}_{1311} & \mathbb{C}_{1322} & \mathbb{C}_{1333} & \mathbb{C}_{1312} & \mathbb{C}_{1323} & \mathbb{C}_{1313} \end{bmatrix}.$$

The incremental form of the variational statement is

$$\begin{aligned} \int_V (\nabla \mathbf{u}_\delta)_c^T \mathbf{S}_M^k (\nabla \mathbf{u}_\Delta)_c d\Omega &= \int_V \rho_0 \mathbf{u}_\delta^T \mathbf{b}^0 dV + \int_{\Gamma_t} \mathbf{u}_\delta^T \mathbf{t}^0 d\Gamma \\ &\quad - \int_V \{ D\bar{\mathbf{E}}(\mathbf{u}^k)[\mathbf{u}_\delta] \}_c^T \mathbf{S}_c^k dV \quad \forall \mathbf{u}_\delta \in \mathcal{V}_u. \end{aligned} \quad (9.8)$$

To obtain the finite element matrices, we introduce the discretizations

$$\mathbf{u} = \mathbf{N}\hat{\mathbf{u}}, \quad \mathbf{u}_\delta = \mathbf{N}\hat{\mathbf{u}}_\delta, \quad \mathbf{u}_\Delta = \mathbf{N}\hat{\mathbf{u}}_\Delta.$$

Using the above we have

$$\{D\bar{\mathbf{E}}(\mathbf{u}^k)[\mathbf{u}_\Delta]\}_c = \mathbf{B}_L \hat{\mathbf{u}}_\Delta, \quad \{D\bar{\mathbf{E}}(\mathbf{u}^k)[\mathbf{u}_\delta]\}_c = \mathbf{B}_L \hat{\mathbf{u}}_\delta,$$

$$(\nabla \mathbf{u}_\Delta)_c = \mathbf{B}_{NL} \hat{\mathbf{u}}_\Delta, \quad (\nabla \mathbf{u}_\delta)_c = \mathbf{B}_{NL} \hat{\mathbf{u}}_\delta,$$

where $\mathbf{B}_L = \mathbf{B}_{L1} + \mathbf{B}_{L2}$ and

$$\mathbf{B}_{L1} = \begin{bmatrix} N_{1,1} & 0 & 0 & N_{2,1} & 0 & 0 & \dots & \dots \\ 0 & N_{1,2} & 0 & 0 & N_{2,2} & 0 & \dots & \dots \\ 0 & 0 & N_{1,3} & 0 & 0 & N_{2,3} & \dots & \dots \\ N_{1,2} & N_{1,1} & 0 & N_{2,2} & N_{2,1} & 0 & \dots & \dots \\ 0 & N_{1,3} & N_{1,2} & 0 & N_{2,3} & N_{2,2} & \dots & \dots \\ N_{1,3} & 0 & N_{1,1} & N_{2,3} & 0 & N_{2,1} & \dots & \dots \end{bmatrix},$$

and $\mathbf{B}_{L2} =$

$$\begin{bmatrix} (\nabla \mathbf{u}^k)_{11} N_{1,1} & (\nabla \mathbf{u}^k)_{21} N_{1,1} & (\nabla \mathbf{u}^k)_{31} N_{1,1} & \dots \\ (\nabla \mathbf{u}^k)_{12} N_{1,2} & (\nabla \mathbf{u}^k)_{22} N_{1,2} & (\nabla \mathbf{u}^k)_{32} N_{1,2} & \dots \\ (\nabla \mathbf{u}^k)_{13} N_{1,3} & (\nabla \mathbf{u}^k)_{23} N_{1,3} & (\nabla \mathbf{u}^k)_{33} N_{1,3} & \dots \\ (\nabla \mathbf{u}^k)_{12} N_{1,1} + (\nabla \mathbf{u}^k)_{11} N_{1,2} & (\nabla \mathbf{u}^k)_{22} N_{1,1} + (\nabla \mathbf{u}^k)_{21} N_{1,2} & (\nabla \mathbf{u}^k)_{32} N_{1,1} + (\nabla \mathbf{u}^k)_{31} N_{1,2} & \dots \\ (\nabla \mathbf{u}^k)_{13} N_{1,2} + (\nabla \mathbf{u}^k)_{12} N_{1,3} & (\nabla \mathbf{u}^k)_{23} N_{1,2} + (\nabla \mathbf{u}^k)_{22} N_{1,3} & (\nabla \mathbf{u}^k)_{33} N_{1,2} + (\nabla \mathbf{u}^k)_{32} N_{1,3} & \dots \\ (\nabla \mathbf{u}^k)_{11} N_{1,3} + (\nabla \mathbf{u}^k)_{13} N_{1,1} & (\nabla \mathbf{u}^k)_{21} N_{1,3} + (\nabla \mathbf{u}^k)_{23} N_{1,1} & (\nabla \mathbf{u}^k)_{31} N_{1,3} + (\nabla \mathbf{u}^k)_{33} N_{1,1} & \dots \end{bmatrix},$$

$$\mathbf{B}_{NL} = \begin{bmatrix} N_{1,1} & 0 & 0 & N_{2,1} & 0 & 0 & \dots & \dots \\ N_{1,2} & 0 & 0 & N_{2,2} & 0 & 0 & \dots & \dots \\ N_{1,3} & 0 & 0 & N_{2,3} & 0 & 0 & \dots & \dots \\ 0 & N_{1,1} & 0 & 0 & N_{2,1} & 0 & \dots & \dots \\ 0 & N_{1,2} & 0 & 0 & N_{2,2} & 0 & \dots & \dots \\ 0 & N_{1,3} & 0 & 0 & N_{2,3} & 0 & \dots & \dots \\ 0 & 0 & N_{1,1} & 0 & 0 & N_{2,1} & \dots & \dots \\ 0 & 0 & N_{1,2} & 0 & 0 & N_{2,2} & \dots & \dots \\ 0 & 0 & N_{1,3} & 0 & 0 & N_{2,3} & \dots & \dots \end{bmatrix}.$$

Let

$$\mathbf{Q} = \int_V \mathbf{B}_{NL} \mathbf{S}_M^k \mathbf{B}_{NL} dV,$$

$$\mathbf{f}_\Delta = \Omega^2 \int_V \rho_0 \tilde{\mathbf{N}}^T (\tilde{\mathbf{X}} + \tilde{\mathbf{u}}^k) dV + \int_{\Gamma_t} \mathbf{N}^T \mathbf{t}^0 d\Gamma - \int_V \mathbf{B}_L^T \mathbf{S}_c^k dV, \quad (9.9)$$

where $\tilde{\mathbf{N}}$ is obtained by excluding the shape functions associated with the angular velocity direction from \mathbf{N} . Then the finite element equations are given by

$$(\mathbf{K} - \Omega^2 \mathbf{M}) \hat{\mathbf{u}}_\Delta = \mathbf{f}_\Delta, \quad (9.10)$$

where

$$\begin{aligned} \mathbf{K} &= \mathbf{Q} + \int_V \mathbf{B}_L^T \mathbf{C}_c \mathbf{B}_L dV, \\ \mathbf{M} &= \int_V \rho \tilde{\mathbf{N}}^T \tilde{\mathbf{N}} dV. \end{aligned} \quad (9.11)$$

Note that the matrix \mathbf{K} is itself a function of displacement $\tilde{\mathbf{u}}^k$ and hence a function of spin

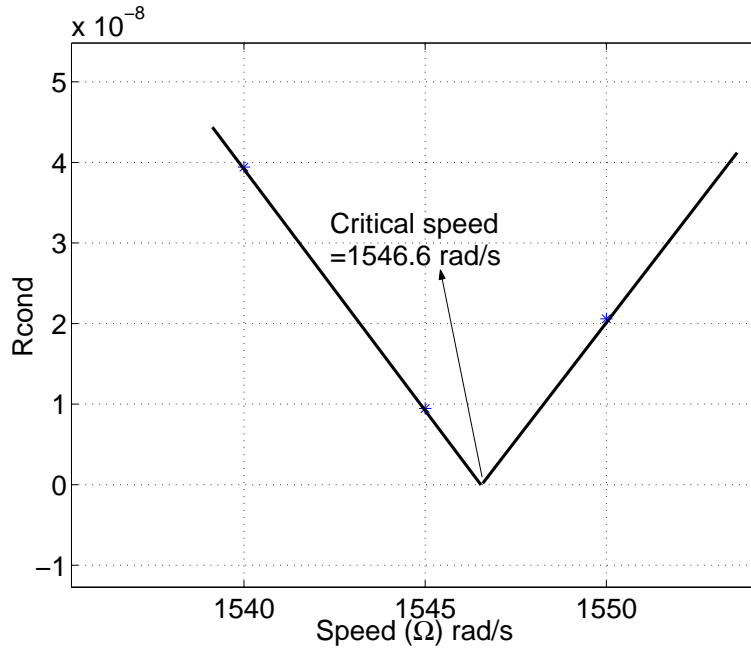


Figure 9.1: Zoomed plot of reciprocal of condition number (MATLAB's RCOND) against speed for the cylinder geometry of chapter 8.

speed Ω . Thus Eq. 9.10 is solved iteratively till the norm of the residual force vector \mathbf{f}_Δ is less than a prescribed tolerance. The critical speed of the rotor is the angular velocity Ω at which the matrix $(\mathbf{K} - \Omega^2 \mathbf{M})$ becomes singular. For actual computation we start with

an angular velocity Ω which is slightly less than the natural frequency of the fundamental mode of lateral vibration. Then Ω is increased slowly and the reciprocal of the condition number (MATLAB's RCOND) of the matrix $(\mathbf{K} - \Omega^2 \mathbf{M})$ is monitored. RCOND steadily decreases and then increases again. The spin speed at which it becomes zero is calculated by extrapolation from either side and this speed is the critical speed. Results for the cylinder geometry (length 2 m, radius 0.25 m) considered in chapter 8 are given in figure 9.1. Ten noded tetrahedral elements were used for the mesh. For the cylinder example considered the cylinder was meshed with 1164 elements with a total of 2030 nodes.

9.2 Concluding remarks

In this chapter we have presented a nonlinear finite element based solution for finding the critical speed of a rotor. The method, itself novel for rotor applications, can be used for rotors of any arbitrary shape (see section 8.2 of chapter 8). Having described this nonlinear formulation, we will now return to the modal projections of chapter 5 in the next chapter where we will describe the use of harmonic elements for axisymmetric rotors. This will result in a dramatic reduction in the computational effort.

Chapter 10

Harmonic elements

We have, in chapter 8, used a three dimensional finite element method to perform the modal projection of our formulation to find the critical speed of arbitrarily shaped rotors. In chapter 9 we implemented a nonlinear finite element technique, without the approximation of modal projections, to find the critical speed of arbitrary rotors. However, we now return to our modal projection methods. For the case of axisymmetric rotors, we can dramatically simplify the calculations involved by using harmonic elements instead of three dimensional elements. This reduces the dimension of the problem from three to two. We now describe the implementation of our modal projection method using harmonic elements

10.1 Introduction

Axisymmetric harmonic elements [34] are used when the geometry and material properties are axisymmetric but the loading and/or the response is not. Using a Fourier series representation for the loads and displacements, the model reduces to two dimensions with only radial and axial coordinates. Harmonic elements can be used, for example, to find symmetry breaking lateral vibration modes of an axisymmetric object. The use of axisymmetric harmonic elements for rotor problems is not new. Stephenson and Rouch [17] have used these elements in a formulation that uses an explicit gyroscopic matrix.

The main advantage of harmonic elements against full three dimensional finite ele-

ments is large savings in time in both modeling and analysis. Harmonic elements are widely used in industry for modal analysis of axisymmetric components. With the present work, such modal analysis can be extended to critical speeds of arbitrary axisymmetric rotors.

In what follows we briefly describe the use of axisymmetric harmonic elements for our calculation. We then present results for the six different axisymmetric rotors that were considered in chapter 8.

10.2 General formulation

The general formulation follows the derivation of section 4.3 of chapter 5. The governing equation for finding the critical speed of a rotor is, as given by Eq. 5.1 of chapter 5,

$$\int_V (\nabla \cdot (\nabla \phi \mathbf{S}_0)) \cdot \phi \, dV + \int_V (\nabla \cdot \mathbf{S}_1) \cdot \phi \, dV = \Omega_c^2 \int_V \rho_0 (\hat{\mathbf{n}} \times \hat{\mathbf{n}} \times \phi) \cdot \phi \, dV,$$

where Ω_c is the critical speed and $\hat{\mathbf{n}}$ is along the undeformed rotor axis.

10.3 Axisymmetric harmonic elements

We use a four noded quadrilateral harmonic element (PLANE25 element in ANSYS) for our analysis. Linear shape functions are used for interpolating the displacements as well as the geometry. The degree of freedom at each node consists of the radial displacement u , the tangential displacement v , and the axial displacement w . The variation of the displacement components along the circumferential direction are given by Fourier series,

$$u = \sum_n \bar{u}_n \cos n\theta + \sum_n \bar{\bar{u}}_n \sin n\theta, \quad (10.1)$$

$$v = \sum_n \bar{v}_n \sin n\theta - \sum_n \bar{\bar{v}}_n \cos n\theta, \quad (10.2)$$

$$w = \sum_n \bar{w}_n \cos n\theta + \sum_n \bar{\bar{w}}_n \sin n\theta, \quad (10.3)$$

where the single-barred series represents the symmetric component (displacement symmetric about the $\theta = 0$ plane) and the double-barred series represents the antisymmetric

component. Axisymmetric problems are represented by the $n = 0$ term of the single-barred series while pure torsion problems are represented by the $n = 0$ term of the double-barred series. For $n = 1$, the case of interest here, the single-barred term represents displacements of flexural modes in one plane while the double-barred term represents the same flexural modes bending in a perpendicular plane. For further details see, e.g., [34].

In our calculation we need ϕ and \mathbf{S}_0 to calculate the critical speed. To evaluate ϕ we perform modal analysis in ANSYS and extract the symmetric components of the displacement by setting $n = 1$ (n is called in ANSYS as MODE). Thus

$$\phi = \bar{\mathbf{u}}_1, \quad \text{and} \quad \bar{\mathbf{u}}_1 = [\bar{u}_1 \cos \theta \quad \bar{v}_1 \sin \theta \quad \bar{w}_1 \cos \theta]^T.$$

Note that the implementation in ANSYS requires a minor trick. Modal analysis for the symmetric option does not output the circumferential displacement v (because it happens to be zero on the $\theta = 0$ plane). So one needs to perform modal analysis for the antisymmetric option as well. The circumferential displacements obtained from the latter can then be incorporated into the original symmetric-option mode after multiplying by $\sin \theta$ as per Eq. 10.2.

Once ϕ is obtained we evaluate $\nabla \phi$ and \mathbf{S}_1 . The spin induced prestress \mathbf{S}_0 is obtained from an axisymmetric analysis (with $n = 0$). After $\nabla \phi$, \mathbf{S}_1 and \mathbf{S}_0 are evaluated, the critical speed of the rotor is found using Eq. 5.1.

The volume integrals appearing in Eq. 5.1 are evaluated using cylindrical coordinates. The expression for $\nabla \phi$ evaluated in cylindrical coordinates is given in appendix B.1. Also, the integration involving the θ coordinate is performed analytically over the circle from $\theta = 0$ to $\theta = 2\pi$ as described in the following section, while the integration in r and z directions is numerically performed using a three point Gauss quadrature scheme over each element.

10.4 Analytical integration with respect to θ in the volume integrals

We show here how the integration with respect to θ in the volume integrals is done analytically before the resulting surface integrals are numerically approximated using Gauss quadrature. We illustrate the calculations for a single mode. Calculations for multiple modes are similar.

10.4.1 $\int_V \mathbf{S}_0 : \nabla \phi^T \nabla \phi dV$

This integral evaluated over each element volume becomes

$$\int_{V_e} \mathbf{S}_0 : \nabla \phi^T \nabla \phi dV_e = \int_{A_e} \int_0^{2\pi} \mathbf{S}_0 : \nabla \phi^T \nabla \phi r d\theta dA_e.$$

The spin induces stress, obtained from an axisymmetric analysis, can be written as

$$\mathbf{S}_0 = \begin{bmatrix} S_{0,11} & 0 & S_{0,13} \\ 0 & S_{0,22} & 0 \\ S_{0,13} & 0 & S_{0,33} \end{bmatrix},$$

with ‘12’ (or $r\theta$) and ‘23’ (or θz) components of the stress being zero. The components of ϕ for the harmonic element can be written as

$$\phi = [\phi_r \cos \theta \quad \phi_\theta \sin \theta \quad \phi_z \cos \theta]^T,$$

where ϕ_r and ϕ_z are obtained from modal analysis corresponding to the symmetric-option-mode (i.e., $\phi_r = \bar{u}_1$ and $\phi_z = \bar{w}_1$) and ϕ_θ is obtained from the antisymmetric-option-mode ($\phi_\theta = \bar{v}_1$). Substituting for \mathbf{S}_0 and ϕ in the above integral we get

$$\int_{A_e} \int_0^{2\pi} \mathbf{S}_0 : \nabla \phi^T \nabla \phi r d\theta dA_e = \int_{A_e} f(\mathbf{S}_0, \phi_r, \phi_\theta, \phi_z, r, z) r dA_e,$$

where

$$\begin{aligned}
 f(\mathbf{S}_0, \phi_r, \phi_\theta, \phi_z, r, z) &= 2\pi S_{0,13} \left(\frac{\partial \phi_\theta}{\partial r} \frac{\partial \phi_\theta}{\partial z} + \frac{\partial \phi_r}{\partial r} \frac{\partial \phi_r}{\partial z} + \frac{\partial \phi_z}{\partial r} \frac{\partial \phi_z}{\partial z} \right) + 4\pi S_{0,22} \frac{\phi_\theta}{r} \frac{\phi_r}{r} \\
 &+ \pi S_{0,11} \left(\left(\frac{\partial \phi_z}{\partial r} \right)^2 + \left(\frac{\partial \phi_r}{\partial r} \right)^2 + \left(\frac{\partial \phi_\theta}{\partial r} \right)^2 \right) + \pi S_{0,22} \left(2 \left(\frac{\phi_\theta}{r} \right)^2 + 2 \left(\frac{\phi_r}{r} \right)^2 + \left(\frac{\phi_z}{r} \right)^2 \right) \\
 &+ \pi S_{0,33} \left(\left(\frac{\partial \phi_\theta}{\partial z} \right)^2 + \left(\frac{\partial \phi_r}{\partial z} \right)^2 + \left(\frac{\partial \phi_z}{\partial z} \right)^2 \right),
 \end{aligned}$$

and A_e is the area of the element under consideration. The above integral can be evaluated using Gauss quadrature after mapping it back to the parent element. Thus

$$\int_{A_e} f(\mathbf{S}_0, \phi_r, \phi_\theta, \phi_z, r, z) r dA_e = \int_{-1}^1 \int_{-1}^1 f(\mathbf{S}_0, \phi_r, \phi_\theta, \phi_z, \xi, \eta) r J d\xi d\eta,$$

where ξ and η are the natural coordinates of the parent element and J is the Jacobian of the transformation. We use a three point Gauss quadrature scheme to evaluate this integral. Note that in spite of apparent division by r in the integrand, there is actually no singularity at $r = 0$; and there are no Gauss points at $r = 0$ either; so the integrals converge satisfactorily and three point Gauss quadrature is good enough.

10.4.2 $\int_V \rho \phi \cdot \phi dV$

This integral is unity if the mode shapes are normalized with respect to the mass matrix. However, our extraction of mode shape from ANSYS involves a minor trick which results in a mode shape that is not mass-normalized. Hence, we directly evaluate this integral. Evaluated over each element, this becomes

$$\begin{aligned}
 \int_{V_e} \rho \phi \cdot \phi dV_e &= \int_{A_e} \int_0^{2\pi} \rho (\phi_r^2 \cos^2 \theta + \phi_\theta^2 \sin^2 \theta + \phi_z^2 \cos^2 \theta) r d\theta dA_e \\
 &= \pi \rho \int_{A_e} (\phi_r^2 + \phi_\theta^2 + \phi_z^2) r dA_e.
 \end{aligned}$$

10.4.3 $\int_V \rho (\hat{\mathbf{n}} \times \hat{\mathbf{n}} \times \boldsymbol{\phi}) \cdot \boldsymbol{\phi} dV$

Since the axis of spin is along the Z axis, $\hat{\mathbf{n}} = \hat{\mathbf{k}}$ and this integral becomes

$$\begin{aligned} \int_{V_e} \rho (\hat{\mathbf{n}} \times \hat{\mathbf{n}} \times \boldsymbol{\phi}) \cdot \boldsymbol{\phi} dV_e &= -\rho \int_{A_e} \int_0^{2\pi} (\phi_r^2 \cos^2 \theta + \phi_\theta^2 \sin^2 \theta) r d\theta dA_e \\ &= -\pi\rho \int_{A_e} (\phi_r^2 + \phi_\theta^2) r dA_e. \end{aligned}$$

In all the numerically evaluated integrals above, ϕ_r , ϕ_θ and ϕ_z are interpolated using standard bilinear shape functions from their nodal values. The derivatives of these displacement components are evaluated using routine finite element procedures as described, e.g., in [34]. This routine procedure is not discussed here in detail.

10.5 Results

We consider six axisymmetric geometries as shown in figure 10.1, identical to those in chapter 8 in geometry and material properties.

The first two rotors are modeled as having simply supported end faces, approximately implemented in the finite element model by restricting endface nodes to have axial displacements only; the last four have their left faces fully fixed, with no other restraints.

From Eq. 5.2 it is seen that the boundary conditions for the first two geometries involve surface terms that are not zero. However, for our calculation we have neglected these terms (an estimate of this term for the cylinder in chapter 8 showed that it is only about 8% of the volume term, which is itself only a part of the calculation). For the other four geometries the surface term is zero.

We use a single mode projection for the first three geometries while we use a two mode projection for the remaining three geometries. Table 10.1 compares the critical speeds obtained using our modal projection method with harmonic elements against critical speeds obtained using the load-stepping calculation in ANSYS (chapter 2) and our nonlinear finite element code (appendix A). It is seen that our modal projection method predicts the

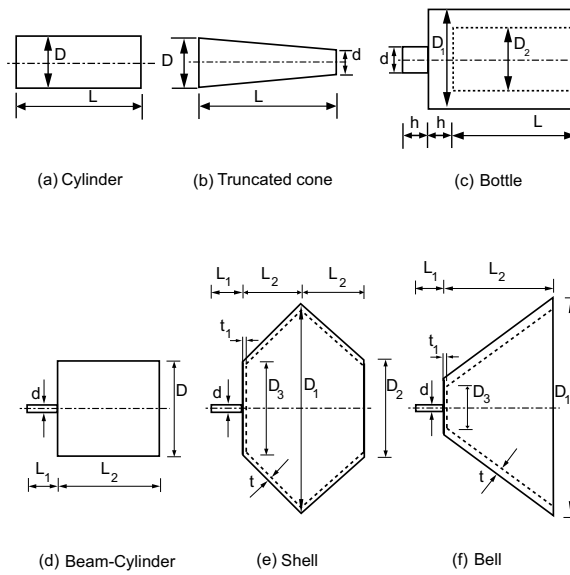


Figure 10.1: Rotor geometries considered.

critical speeds very well. The key point to note here is the match between the results obtained here using harmonic elements and the results obtained in chapter 8 using the more computationally demanding three dimensional formulation.

Next we consider the remaining three geometries. Table 10.2 compares the critical speeds as estimated by our modal projection method with the analytical estimates. It is seen that our method makes excellent prediction of the critical speeds. As noted earlier in chapter 8, we capture imaginary critical speeds, representing suppression of conceivable whirling modes due to gyroscopic effects. As mentioned above, the key point here is the match between the results obtained here using harmonic elements and the results obtained using the more computationally demanding three dimensional formulation.

10.6 Concluding remarks

We have computed the critical speeds of arbitrary axisymmetric rotors using two dimensional harmonic elements and a prestress based continuum level formulation with no need for explicitly added on gyroscopic terms. For simplicity, we have also used modal projec-




Rotor	ω_f (harmonic element)	Critical speed Ω_c			
		ANSYS (chap. 2)	Our code (appendix A)	3D modal projection (chap. 8)	Harmonic modal projection
 Cylinder	1499.48	1546.46	1545.38	1544.96	1546.00
 Cone	969.24	990.70	991.48	990.38	990.42
 Bottle	363.77	381.18	380.05	380.18	381.03

Table 10.1: Comparison of critical speeds from various methods. All speeds and frequencies in rad/s. Note that the difference between bending and whirling frequencies is relatively small (e.g., about 3% for the cylinder). Nevertheless, this small *difference* is captured to within about 1.4%.




Rotor	ω_f (harmonic element)	Critical speeds Ω_c		
		Analytical (Approximate) (chap. 6)	3D modal projection (chap. 8)	Harmonic modal projection
 Beam Cyl.	0.125 (2.59)	0.234 $1.98i$	0.234 $1.96i$	0.234 $1.95i$
 Shell	0.171 (4.02)	$0.477i$ 1.73	$0.462i$ 1.76	$0.474i$ 1.72
 Bell	0.109 (3.59)	0.330 $1.55i$	0.334 $1.51i$	0.330 $1.53i$

Table 10.2: Comparison of critical speeds from various methods. All speeds and frequencies in rad/s. Modal projections performed with two modes. The imaginary values represent conceivable whirling motions that are actually suppressed by gyroscopic terms.

tions, which allows the calculation to be done using routinely available commercial code along with some volume integrals on the side (the actual numerical integration is done over areas and not volumes).

The new harmonic element formulation was checked against the results of three dimensional modal projection described in chapter 8. The match is excellent: as discussed before, the *difference* between the lateral non-spinning bending frequencies and the synchronous whirl frequencies was captured accurately therein, and those results have now been well matched by the computationally much more efficient harmonic element formulation.

Chapter 11

Asynchronous whirl

In this chapter we use our formulation to study asynchronous whirl. We have already described asynchronous whirl through an analytical example in chapter 6 (see section 6.2.2.2). We now present numerical solutions for arbitrary shaped rotors.

11.1 Modal projections

We now derive the modal projection formulation for asynchronous whirl. The method developed is valid for both axisymmetric and non-axisymmetric rotors. We begin with the dynamic equilibrium equation,

$$\nabla \cdot (\mathbf{FS}) = \rho_0 \frac{\partial^2 \boldsymbol{\chi}}{\partial t^2}. \quad (11.1)$$

The difference between synchronous and asynchronous whirl is that in the latter case the shaft is no longer static when viewed in a frame rotating at the shaft spin speed. If we write our equations in such a rotating frame, the displacement of each point on the rotor is now a function of time. Hence, if

$$\mathbf{u} = \sum_k a_k \boldsymbol{\phi}_k$$

represents the displacements of points on the rotor expressed in the rotating coordinate system, the coefficients a_k are now functions of time. In the synchronous whirl case, a was constant. This will have consequences for the acceleration term.

We write our equations in a reference frame rotating about the bearing centerline at the spin speed of the shaft (see figure 11.1). We express the motion of the rotor as a linear combination of lateral vibration modes. Since in this case points on the rotor will in general not move in straight lines as seen in the rotating frame, we need at least two non-coplanar modes to describe the motion of the rotor. We will illustrate our calculation by choosing two modes, say ϕ_1 and ϕ_2 , corresponding to lateral vibrations in different planes. For an axisymmetric rotor, two modes with the same natural frequency will be used.

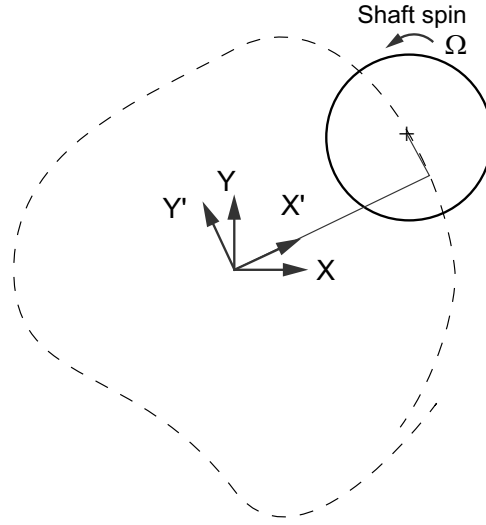


Figure 11.1: The frame $X'-Y'$ rotates about the bearing centerline at the rate Ω . A typical point on the centerline of the shaft moves along an arbitrary curve.

The displacement of any point on the rotor, as seen in the rotating frame, is

$$\mathbf{u} = \mathbf{u}_0 + a(t)\phi_1(\mathbf{X}) + b(t)\phi_2(\mathbf{X}),$$

where \mathbf{u}_0 is, as before, the spin-induced deformation and $a(t)$ and $b(t)$ are generalized coordinates describing the configuration of the rotor. Substituting into Eq. 11.1, using the St. Venant-Kirchhoff material relation and using approximations similar to those made in section 4.3, we get

$$\nabla \cdot \mathbf{S}_0 + a\nabla \cdot \mathbf{S}_1 + b\nabla \cdot \mathbf{S}_2 + a\nabla \cdot (\nabla\phi_1\mathbf{S}_0) + b\nabla \cdot (\nabla\phi_2\mathbf{S}_0) = \rho_0 \frac{\partial^2 \chi}{\partial t^2}, \quad (11.2)$$

where

$$\mathbf{S}_0 = \lambda(\text{tr}\mathbf{E}_0) \mathbf{I} + 2\mu \mathbf{E}_0 \quad \text{with} \quad \mathbf{E}_0 = \frac{1}{2} (\nabla\mathbf{u}_0 + \nabla\mathbf{u}_0^T),$$

$$\begin{aligned}\mathbf{S}_1 &= \lambda(\text{tr}\mathbf{E}_1) \mathbf{I} + 2\mu \mathbf{E}_1 \quad \text{with} \quad \mathbf{E}_1 = \frac{1}{2} (\nabla \phi_1 + \nabla \phi_1^T), \\ \mathbf{S}_2 &= \lambda(\text{tr}\mathbf{E}_2) \mathbf{I} + 2\mu \mathbf{E}_2 \quad \text{with} \quad \mathbf{E}_2 = \frac{1}{2} (\nabla \phi_2 + \nabla \phi_2^T).\end{aligned}$$

The acceleration of the point with position vector $\boldsymbol{\chi}$ is given by [31]

$$\frac{\partial^2 \boldsymbol{\chi}}{\partial t^2} = \frac{d^2 a}{dt^2} \phi_1 + \frac{d^2 b}{dt^2} \phi_2 + 2\boldsymbol{\Omega} \times \left(\frac{da}{dt} \phi_1 + \frac{db}{dt} \phi_2 \right) + \boldsymbol{\Omega} \times \boldsymbol{\Omega} \times (\mathbf{X} + a\phi_1 + b\phi_2).$$

where \mathbf{X} is the initial position vector of the point, i.e., before deformation.

Choosing two different virtual displacements, one for each of the two mode shapes, as

$$\begin{aligned}\delta \mathbf{w}_1 &= \delta a \phi_1, \\ \delta \mathbf{w}_2 &= \delta b \phi_2,\end{aligned}$$

virtual work gives:

$$\begin{aligned}\int_V (\nabla \cdot \mathbf{S}_0 + a \nabla \cdot \mathbf{S}_1 + b \nabla \cdot \mathbf{S}_2 + a \nabla \cdot (\nabla \phi_1 \mathbf{S}_0) \\ + b \nabla \cdot (\nabla \phi_2 \mathbf{S}_0)) \cdot \delta \mathbf{w}_k dV = \int_V \rho_0 \frac{\partial^2 \boldsymbol{\chi}}{\partial t^2} \cdot \delta \mathbf{w}_k dV, \quad k = 1, 2.\end{aligned} \quad (11.3)$$

Since ϕ_1 and ϕ_2 are chosen as mass normalized mode shapes of the rotor, we obtain some simplifications in the virtual work calculation. In particular we have, as described in section 5.2,

$$\int_V (\nabla \cdot \mathbf{S}_m) \cdot \phi_n dV = -\rho_0 \omega_m^2 \int_V \phi_m \cdot \phi_n dV = -\rho_0 \omega_m^2 \delta_{mn},$$

where $\delta_{mn} = 1$ if $m = n$ and 0 otherwise. Also the term $\nabla \cdot \mathbf{S}_0$ on the left side of Eq. 11.3 is balanced by the body force that causes it, the $\rho(\boldsymbol{\Omega} \times \boldsymbol{\Omega} \times \mathbf{X})$ term on the right side, and these terms drop out of the equation.

Substituting the virtual displacements into Eq. 11.3, we get

$$\begin{aligned}-a\omega_1^2 + a \int_V (\nabla \cdot (\nabla \phi_1 \mathbf{S}_0)) \cdot \phi_1 dV + b \int_V (\nabla \cdot (\nabla \phi_2 \mathbf{S}_0)) \cdot \phi_1 dV = \ddot{a} + \rho \dot{a} \int_V (2\boldsymbol{\Omega} \times \phi_1) \cdot \phi_1 dV \\ + \rho \dot{b} \int_V (2\boldsymbol{\Omega} \times \phi_2) \cdot \phi_1 dV + a\rho \int_V (\boldsymbol{\Omega} \times \boldsymbol{\Omega} \times \phi_1) \cdot \phi_1 dV + b\rho \int_V (\boldsymbol{\Omega} \times \boldsymbol{\Omega} \times \phi_2) \cdot \phi_1 dV,\end{aligned} \quad (11.4)$$

and

$$\begin{aligned}
 & -b\omega_2^2 + a \int_V (\nabla \cdot (\nabla \phi_1 \mathbf{S}_0)) \cdot \phi_2 dV + b \int_V (\nabla \cdot (\nabla \phi_2 \mathbf{S}_0)) \cdot \phi_2 dV = \ddot{b} + \rho \dot{a} \int_V (2 \boldsymbol{\Omega} \times \phi_1) \cdot \phi_2 dV \\
 & + \rho \dot{b} \int_V (2 \boldsymbol{\Omega} \times \phi_2) \cdot \phi_2 dV + a \rho \int_V (\boldsymbol{\Omega} \times \boldsymbol{\Omega} \times \phi_1) \cdot \phi_2 dV + b \rho \int_V (\boldsymbol{\Omega} \times \boldsymbol{\Omega} \times \phi_2) \cdot \phi_2 dV,
 \end{aligned} \tag{11.5}$$

where the dots above a and b denote time derivatives. These equations, written in matrix notation, appear as

$$\begin{bmatrix} 1 & 0 \\ 0 & 1 \end{bmatrix} \begin{Bmatrix} \ddot{a} \\ \ddot{b} \end{Bmatrix} + \begin{bmatrix} 0 & G_{1,2} \\ -G_{1,2} & 0 \end{bmatrix} \begin{Bmatrix} \dot{a} \\ \dot{b} \end{Bmatrix} + \begin{bmatrix} K_{1,1} & K_{1,2} \\ K_{1,2} & K_{2,2} \end{bmatrix} \begin{Bmatrix} a \\ b \end{Bmatrix} = 0. \tag{11.6}$$

The above governs motion of the rotor written in a rotating coordinate system that spins at the shaft speed Ω , as projected onto two modes. This equation is identical in structure to similarly motivated but differently derived equations in the literature [16]. For

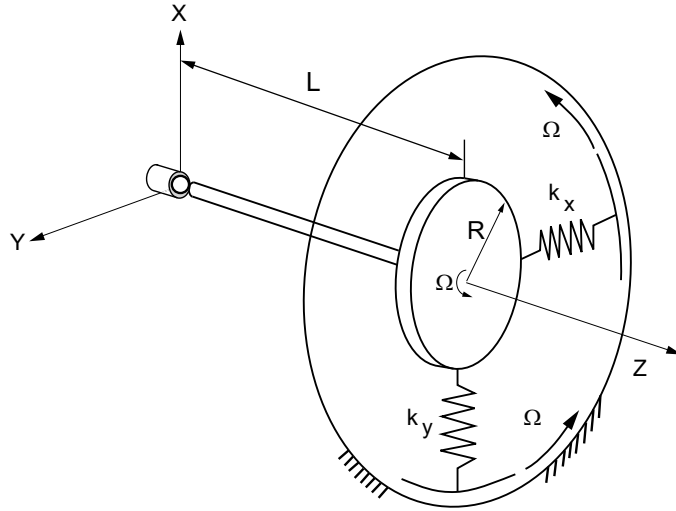


Figure 11.2: Ewins's rotor with asymmetric springs on supports that rotate with the disc.

example, consider Ewins's rotor of chapter 6. The springs now have different stiffnesses k_x and k_y and rotate with the disc as shown in figure 11.2. The governing equation of motion

of this rotor is (Eq. 2.118 pg. 97 of [25] with k replaced by k_x or k_y)

$$\begin{aligned} \begin{bmatrix} \frac{I_0}{L^2} & 0 \\ 0 & \frac{I_0}{L^2} \end{bmatrix} \begin{Bmatrix} \ddot{x}_R \\ \ddot{y}_R \end{Bmatrix} + \begin{bmatrix} 0 & -\frac{2\Omega I_0}{L^2} + \frac{J\Omega}{L^2} \\ \frac{2\Omega I_0}{L^2} - \frac{J\Omega}{L^2} & 0 \end{bmatrix} \begin{Bmatrix} \dot{x}_R \\ \dot{y}_R \end{Bmatrix} + \\ \begin{bmatrix} -\frac{I_0\Omega^2}{L^2} + \frac{J\Omega^2}{L^2} + k_x & 0 \\ 0 & -\frac{I_0\Omega^2}{L^2} + \frac{J\Omega^2}{L^2} + k_y \end{bmatrix} \begin{Bmatrix} x_R \\ y_R \end{Bmatrix} = \{0\}, \quad (11.7) \end{aligned}$$

where x_R and y_R are the coordinates in the rotating frame and the remaining parameters are as defined in section 6.2. As can be seen, Eq. 11.6 and Eq. 11.7 are identical in structure. However, Eq. 11.6 uses modal generalized coordinates that are different from Cartesian coordinates, and can be transferred to the inertial coordinate system by multiplication with a rotation matrix only after a and b are suitably reinterpreted as components of a vector. We will now consider some examples.

11.2 Axisymmetric rotor example

We now present the results for the cylinder example considered in chapter 8. This is an axisymmetric geometry and consequently the two modes chosen, as per the above discussion, have the same natural frequency ($\omega_f = 1498.73$ rad/s). The cylinder spins about its axis (the Z direction).

We start with Eq. 11.6, substitute

$$a = Ae^{\lambda t} \quad \text{and} \quad b = Be^{\lambda t}$$

and solve for λ . We get two pairs of complex conjugate eigenvalues with corresponding complex conjugate eigenvectors. The synchronous whirl speed is that speed at which the rotor is stationary as seen in the rotating frame. This happens when $\lambda = 0$. For other values of λ the actual motion, as seen in an inertial frame, can be obtained as follows. After deformation, the coordinates of a point P on the rotor, with reference position (x_P, y_P, z_P) , in the rotating coordinate system, are

$$\begin{Bmatrix} x_R \\ y_R \\ z_R \end{Bmatrix} = \begin{Bmatrix} x_P \\ y_P \\ z_P \end{Bmatrix} + Ae^{\lambda t} \begin{Bmatrix} \phi_{1,P}^x \\ \phi_{1,P}^y \\ \phi_{1,P}^z \end{Bmatrix} + Be^{\lambda t} \begin{Bmatrix} \phi_{2,P}^x \\ \phi_{2,P}^y \\ \phi_{2,P}^z \end{Bmatrix}, \quad (11.8)$$

where $(\phi_{1,P}^x, \phi_{1,P}^y, \phi_{1,P}^z)$ and $(\phi_{2,P}^x, \phi_{2,P}^y, \phi_{2,P}^z)$ are the components of mode 1 and 2 respectively for the point P. This can be transformed to the inertial coordinate system using

$$\begin{Bmatrix} x_I \\ y_I \\ z_I \end{Bmatrix} = \begin{bmatrix} \cos(\Omega t) & -\sin(\Omega t) & 0 \\ \sin(\Omega t) & \cos(\Omega t) & 0 \\ 0 & 0 & 1 \end{bmatrix} \begin{Bmatrix} x_R \\ y_R \\ z_R \end{Bmatrix}, \quad (11.9)$$

where Ω is the spin speed of the shaft. One can determine the path of point P on the

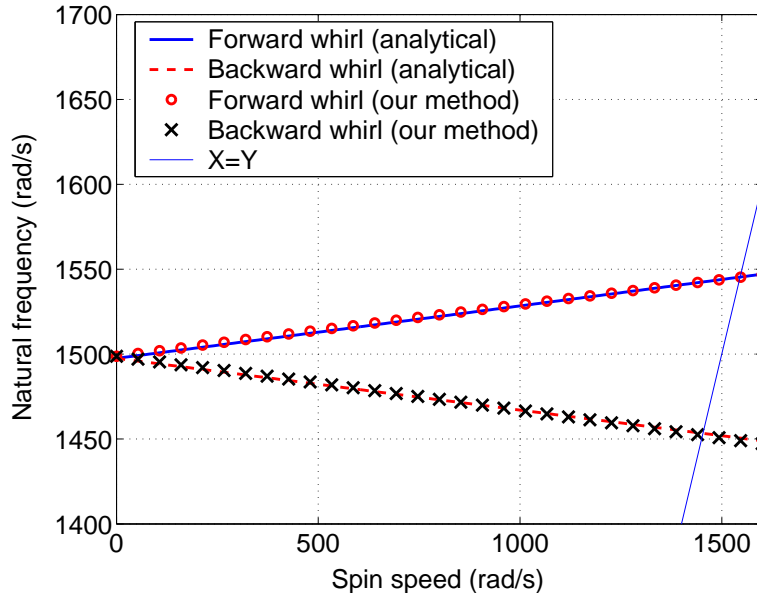


Figure 11.3: Campbell diagram of the cylindrical rotor. The eigenvalue plotted is $\lambda + i\Omega$ which is purely imaginary at all speeds for this rotor geometry. Note that the horizontal and vertical scales are unequal.

rotor using Eq. 11.9. If one of the possible paths is a circle, then a steady circular whirling solution exists and one can determine the natural frequency of the spinning rotor using the relation

$$\omega_f = \lambda + i\Omega,$$

where we note that λ is purely imaginary. For the cylinder geometry, as is well known, such a whirling solution does exist and we can determine the natural frequency as a function of the spin speed. Such a plot, called a Campbell diagram [16], is shown in figure 11.3 where our results are compared with analytical results given in [38]. Our results match well with the analytical results.

There are two branches shown in the plot above. The upper one with positive slope corresponds to forward whirl and the lower one with negative slope corresponds to backward whirl. The thin line shown in the plot is the $x = y$ line and the intersection of this with the forward whirl line corresponds to the critical speed of the shaft.

Next, we consider the orbit of the rotating cylinder at a *non-critical* speed. First, the eigenvalue problem arising from Eq. 11.6 is solved for some non-critical speed Ω . The solution yields two pairs of complex conjugate eigenvalues: $\lambda_1, \bar{\lambda}_1, \lambda_2$ and $\bar{\lambda}_2$. The eigenvalues along with the eigenvectors yield the path of the rotor as seen in a rotating coordinate system through Eq. 11.8. For example, for one complex conjugate pair of eigenvalues, say $\lambda_R + i\lambda_I$ and $\lambda_R - i\lambda_I$, with complex conjugate eigenvectors $u + iv$ and $u - iv$, we have the solution

$$\begin{Bmatrix} a_1 \\ b_1 \end{Bmatrix} = \alpha(u + iv)e^{\lambda_R t + i\lambda_I t} + \bar{\alpha}(u - iv)e^{\lambda_R t - i\lambda_I t}$$

for any α such that a_1 and b_1 are real. Similarly for the second pair of complex conjugate eigenvalues we would have another solution

$$\begin{Bmatrix} a_2 \\ b_2 \end{Bmatrix}$$

of a similar form. And finally, the general solution is of the form

$$\begin{Bmatrix} a \\ b \end{Bmatrix} = \begin{Bmatrix} a_1 \\ b_1 \end{Bmatrix} + \begin{Bmatrix} a_2 \\ b_2 \end{Bmatrix}.$$

The path in the rotating coordinate system of a typical point P on the rotor is then given by

$$\begin{Bmatrix} x_R \\ y_R \\ z_R \end{Bmatrix} = \begin{Bmatrix} x_P \\ y_P \\ z_P \end{Bmatrix} + a \begin{Bmatrix} \phi_{1,P}^x \\ \phi_{1,P}^y \\ \phi_{1,P}^z \end{Bmatrix} + b \begin{Bmatrix} \phi_{2,P}^x \\ \phi_{2,P}^y \\ \phi_{2,P}^z \end{Bmatrix}, \quad (11.10)$$

The path in the inertial frame can then be computed using Eq. 11.9.

Figure 11.4 shows the orbits in the X-Y plane for a point P located on the axis of the cylinder near the center of the rotor span. The governing equations, from Eq. 11.6, in the rotating coordinate system at a speed Ω are

$$\begin{bmatrix} 1 & 0 \\ 0 & 1 \end{bmatrix} \begin{Bmatrix} \ddot{a} \\ \ddot{b} \end{Bmatrix} + \begin{bmatrix} 0 & 1.938\Omega \\ -1.938\Omega & 0 \end{bmatrix} \begin{Bmatrix} \dot{a} \\ \dot{b} \end{Bmatrix} + \begin{bmatrix} \omega_f^2 - 0.941\Omega^2 & 0 \\ 0 & \omega_f^2 - 0.941\Omega^2 \end{bmatrix} \begin{Bmatrix} a \\ b \end{Bmatrix} = 0,$$

where $\omega_f = 1498.7$ rad/s is the natural frequency of the rotor. For the computation we choose $\Omega = 900$ rad/s, which is less than the critical speed of 1546.4 rad/s. For $\Omega = 900$ rad/s, the four eigenvalues are obtained as

$$\lambda_1 = 626.18i, \quad \bar{\lambda}_1 = -626.18i, \quad \lambda_2 = 2370.17i \quad \text{and} \quad \bar{\lambda}_2 = -2370.17i,$$

and the corresponding four eigenvectors are

$$v_1 = \begin{Bmatrix} -3.78i \\ 3.78 \end{Bmatrix}, \quad v_2 = \begin{Bmatrix} 3.78i \\ 3.78 \end{Bmatrix}, \quad v_3 = \begin{Bmatrix} 1 \\ -i \end{Bmatrix} \quad \text{and} \quad v_4 = \begin{Bmatrix} 1 \\ i \end{Bmatrix},$$

where in the above, all elements have been arbitrarily normalized with respect to the first element of v_3 as returned by MATLAB. Note that the first entry of the eigenvector corresponds to the modal coordinate a and the second to the modal coordinate b .

Figure 11.4 (a) shows the path corresponding to the eigenvalue pair λ_1 and $\bar{\lambda}_1$ as seen in the rotating frame. The position (x_R, y_R, z_R) of the point P (chosen to be on the centerline of the cylinder) tracing this path at any time t is obtained by first calculating the modal coordinates using the solution

$$\begin{Bmatrix} a \\ b \end{Bmatrix} = v_1 e^{\lambda_1 t} + v_2 e^{\bar{\lambda}_1 t}$$

and then using Eq. 11.10. The path as seen in an inertial frame can now be computed using Eq. 11.9 and is shown in figure 11.4 (b). The paths are seen to be perfect circles representing steady circular whirling motion.

The same is true for the path corresponding to eigenvalue pair λ_2 and $\bar{\lambda}_2$ shown in figures 11.4 (c) (rotating frame) and 11.4 (d) (inertial frame). The position of the point P for this path (in the rotating frame) is calculated using the solution

$$\begin{Bmatrix} a \\ b \end{Bmatrix} = v_3 e^{\lambda_2 t} + v_4 e^{\bar{\lambda}_2 t}$$

followed by Eq. 11.10. The path as seen in the inertial frame can then be computed using Eq. 11.9.

Figures 11.4 (e) and (f) show one possible solution obtained as a combination of all eigenvectors. The path is no longer a circle. Here

$$\begin{Bmatrix} a \\ b \end{Bmatrix} = v_1 e^{\lambda_1 t} + v_2 e^{\bar{\lambda}_1 t} + v_3 e^{\lambda_2 t} + v_4 e^{\bar{\lambda}_2 t},$$

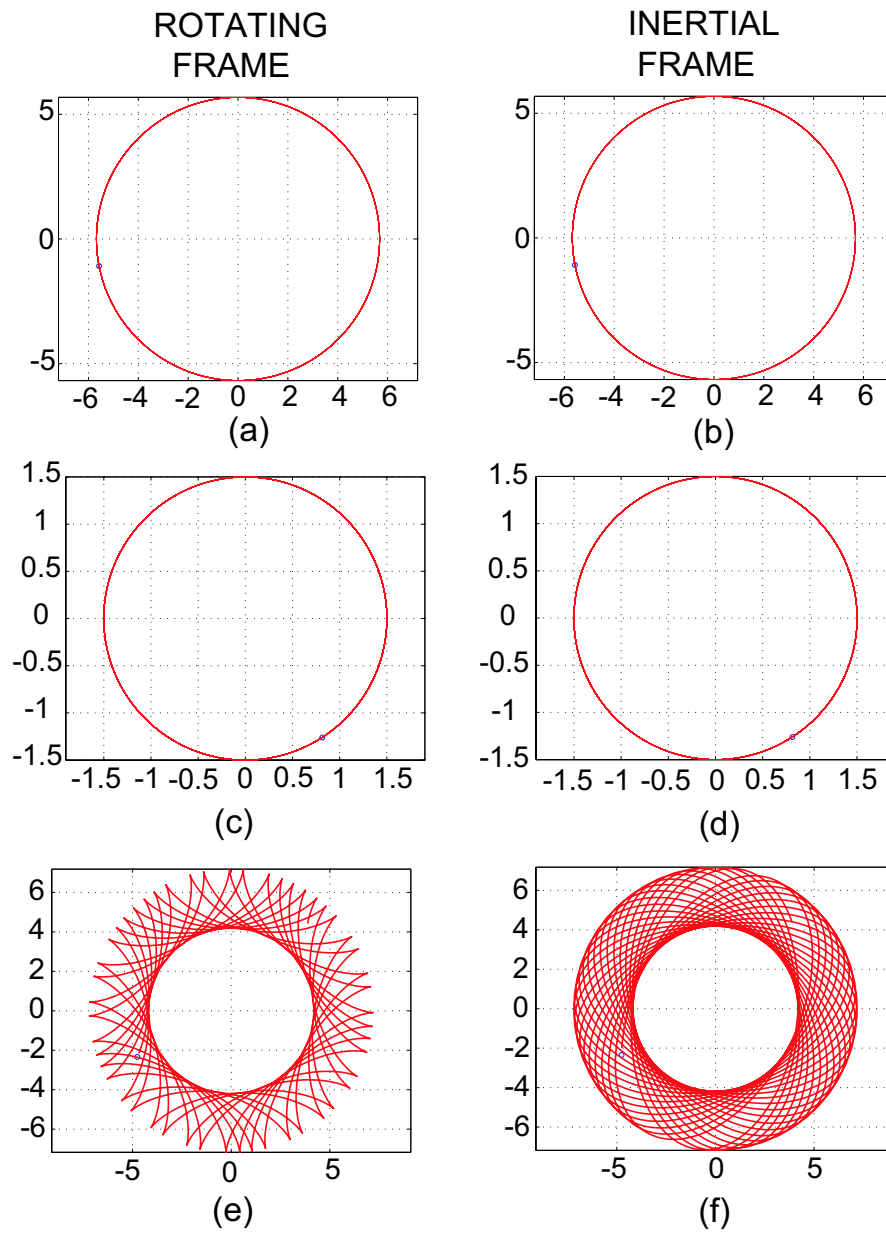


Figure 11.4: Orbital paths of a point on the axis of the cylinder for $\Omega = 900$ rad/s. There are four eigenvalues ($\lambda = \pm 626.18i$ and $\lambda = \pm 2370.17i$) describing the motion in the rotating coordinate system. Figures (a), (c) and (e) are the paths seen in the rotating frame while (b), (d) and (f) correspond to those in the inertial frame. Displacements are arbitrarily scaled.

and the positions of the point P at time t as seen in the inertial and rotating frame are calculated using Eq. 11.9 and Eq. 11.10 respectively.

11.3 A non-axisymmetric rotor example

Now we consider a non-axisymmetric rotor where the two principal area moments of inertia of the cross-section are different. There is a difference in the stiffness in the two principal directions. The behavior of such rotors is qualitatively different from that of an axisymmetric rotor in that these rotors have a nonzero region of instability, where the real part of an eigenvalue is positive.

Consider a shaft of rectangular cross-section. The rotor is 2 m long and the cross-section is 0.5 m \times 0.1 m. The mesh used for the computation is shown in figure 11.5. It has 5135 elements (10 noded tetrahedral) and 9254 nodes.

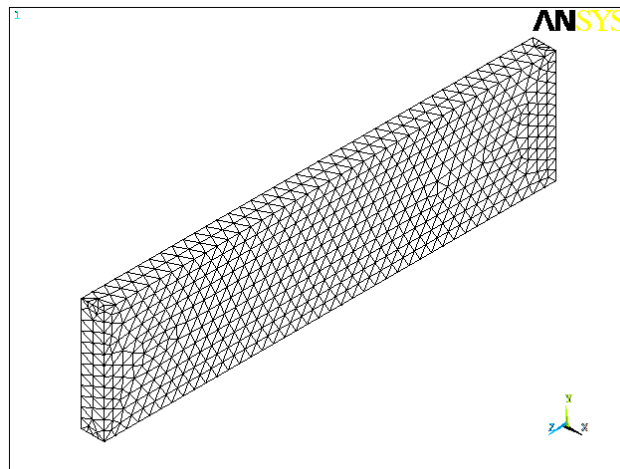


Figure 11.5: The mesh of the non-axisymmetric rotor geometry considered.

The procedure for setting up the eigenvalue problem in the rotating coordinate system is as described before in section 11.2. In this case we use the first lateral bending mode in each of the two principal planes, i.e., for a rotor with its axis along the Z direction, the

first mode in the X - Z plane and the first mode in the Y - Z plane are used. The corresponding natural frequencies are $\omega_{f1} = 368.73$ rad/s and $\omega_{f2} = 1691.24$ rad/s respectively. The eigenvalues are then determined as a function of the spin speed. The speed at which the eigenvalue becomes zero corresponds to the critical speed or synchronous whirl speed. At this speed the rotor performs synchronous whirl. For the two mode approximation considered, two such speeds exist: 369.48 rad/s and 1755.25 rad/s. Between these speeds the real part of one eigenvalue is positive and the rotor is unstable. A plot of variation of the real part of that eigenvalue with spin speed is shown in figure 11.6.

We mention that since stiffnesses in the two principal directions are quite different, two lateral modes in the X - Z plane have natural frequencies less than that of the first lateral mode in the Y - Z plane. However, the plot in figure 11.6 is made using only one mode in each principal plane. It is possible that the region of instability corresponding to the second mode might overlap the present instability zone. However, the onset of instability at a speed of 369.48 rad/s is beyond doubt.

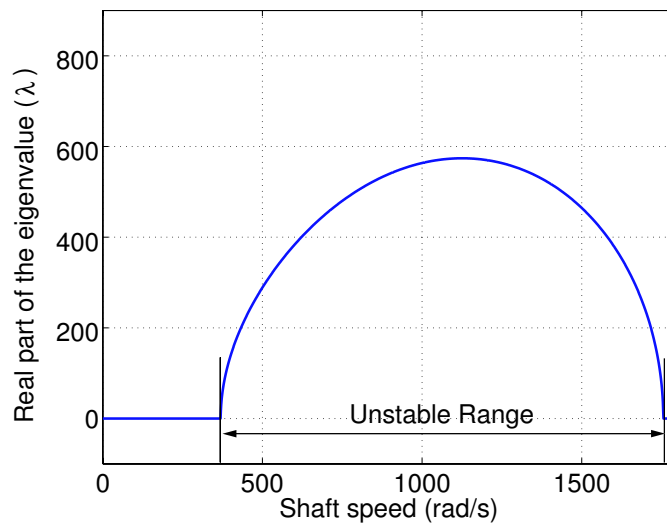


Figure 11.6: Real part of the instability causing eigenvalue λ as a function of spin speed. The region where this is positive is the instability region. The edges of the instability region are the synchronous whirl speeds.

The governing equations, from Eq. 11.6, in the rotating coordinate system at a speed

Ω are (correct to 2 decimal places)

$$\begin{bmatrix} 1 & 0 \\ 0 & 1 \end{bmatrix} \begin{Bmatrix} \ddot{a} \\ \ddot{b} \end{Bmatrix} + \begin{bmatrix} 0 & -1.96\Omega \\ 1.96\Omega & 0 \end{bmatrix} \begin{Bmatrix} \dot{a} \\ \dot{b} \end{Bmatrix} + \begin{bmatrix} \omega_{f1}^2 - 1.00\Omega^2 & 0 \\ 0 & \omega_{f2}^2 - 0.93\Omega^2 \end{bmatrix} \begin{Bmatrix} a \\ b \end{Bmatrix} = 0. \quad (11.11)$$

Now we discuss the motion of this rotor at a speed less than the first critical speed, say 300 rad/s. The solution of the eigenvalue problem for this speed again yields two pairs of complex conjugate eigenvalues and corresponding complex conjugate eigenvectors. They are

$$\lambda_1 = 202.80i, \quad \bar{\lambda}_1 = -202.80i, \quad \lambda_2 = 1768.51i \quad \text{and} \quad \bar{\lambda}_2 = -1768.51i,$$

and

$$v_1 = \begin{Bmatrix} -27.25i \\ -1.19 \end{Bmatrix}, \quad v_2 = \begin{Bmatrix} 27.25i \\ -1.19 \end{Bmatrix}, \quad v_3 = \begin{Bmatrix} 1 \\ 2.96i \end{Bmatrix} \quad \text{and} \quad v_4 = \begin{Bmatrix} 1 \\ -2.96i \end{Bmatrix}.$$

Using these eigenvalues and eigenvectors, the path of a point on the rotor can again be generated using procedures similar to that described in section 11.2. Figure 11.7 shows a few possible paths traced by a point P on the rotor centerline. To obtain these paths, $\{a \ b\}^T$ is first calculated as: $v_1e^{\lambda_1 t} + v_2e^{\bar{\lambda}_1 t}$ for the path shown in figure 11.7 (a), $v_3e^{\lambda_2 t} + v_4e^{\bar{\lambda}_2 t}$ for figure 11.7 (c) and $v_1e^{\lambda_1 t} + v_2e^{\bar{\lambda}_1 t} + v_3e^{\lambda_2 t} + v_4e^{\bar{\lambda}_2 t}$ for figure 11.7 (e). Then the path in the rotating frame is calculated using Eq. 11.10. Finally, the path in the inertial frame is calculated using Eq. 11.9.

In this case, the orbits are no longer a circle when viewed in the rotating frame that spins at the rotor speed. Instead, they are now ellipses as shown in figures 11.7 (a) and (c). Consequently, the orbits as viewed in the inertial frame are complicated as shown in figures 11.7 (b) and (d). Any motion of the rotor at this speed can be expressed as a linear combination of the orbits corresponding to the four eigenvalues. This again will be a complicated orbit as shown in figures 11.7 (e) and (f).

Unlike the axisymmetric rotor, a non-axisymmetric rotor in general cannot perform steady circular whirling at any speed (see appendix D). Hence it is not possible to define a natural frequency for these rotors at a general speed. The above is not always clearly stated in the rotor literature. It is not uncommon to see the eigenvalue problem (from Eq. 11.6) supposedly transformed back into the inertial coordinates by multiplying $Ae^{\lambda t}$ with $e^{i\Omega t}$ to get $Ae^{i(\lambda_0 + \Omega)t}$ (see, e.g., section 8.4 of [40]), where $i\lambda_0 = \lambda$. However, the term $(\lambda_0 + \Omega)$ has

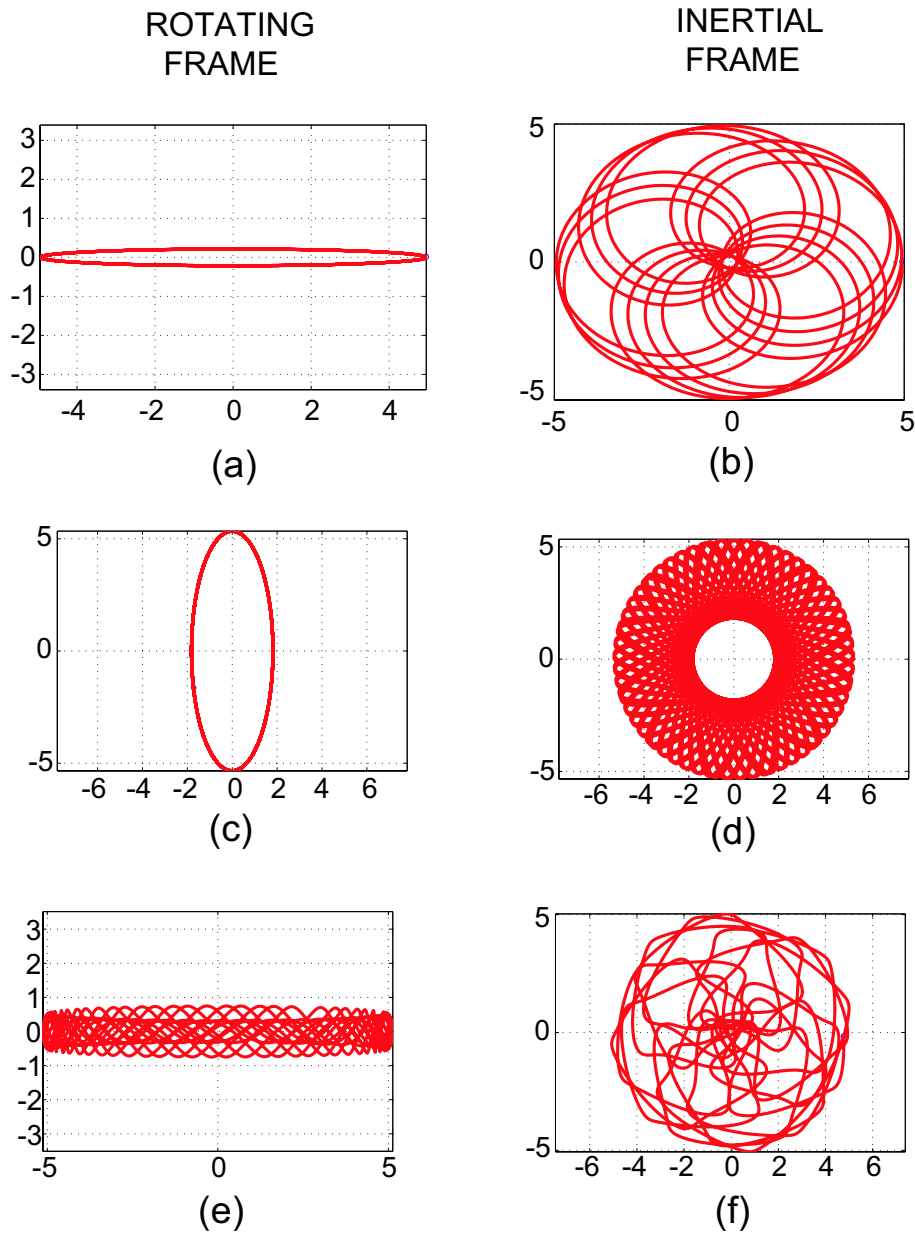


Figure 11.7: Orbital path of a point on the axis of the rotor for $\Omega = 300$ rad/s. There are four eigenvalues ($\lambda = \pm 202.80 i$ and $\lambda = \pm 1768.51 i$) describing the motion in the rotating coordinate system. Figures (a), (c) and (e) are the paths seen in the rotating frame while (b), (d) and (f) correspond to those in the inertial frame. Displacements are arbitrarily scaled.

no physical meaning for non-axisymmetric rotors and is *not* the natural frequency of the rotor. A plot of $(\lambda_0 + \Omega)$ against the spin speed Ω only serves to indicate the instability regions and the critical speeds.

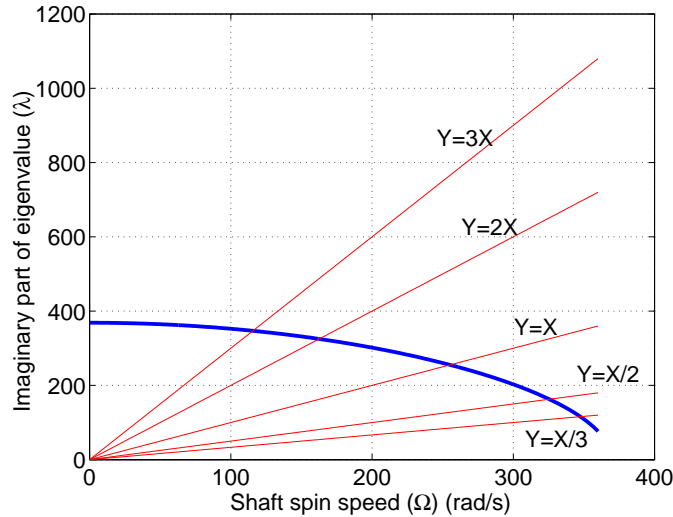


Figure 11.8: Variation of imaginary part of λ_1 with shaft spin speed Ω .

Finally, we consider the following question. Are there spin speeds for which periodic solutions exist for this rotor? The orbit corresponding to even one of the eigenvalues (λ_1 or λ_2), as seen in the inertial frame, is not typically periodic in that the path never closes (see figures 11.7 (a) and (c)). However, if the spin speed Ω and the imaginary part of the eigenvalue are rational multiples, then the orbit will close and periodic motions exist. Figure 11.8 plots the variation of imaginary part of λ_1 with Ω . The intersections of the above curve with curves of the form $nX - mY = 0$ for integer values of m and n correspond to speeds where a periodic solution exists. Figure 11.9 illustrates four such periodic orbits corresponding to $\lambda = \Omega/2$, Ω , 2Ω and 3Ω . The most intriguing is figure 11.9 (b) which shows a perfect circle that is off-center. Perhaps such a whirling motion might be excited by self weight of a horizontal non-axisymmetric rotor.

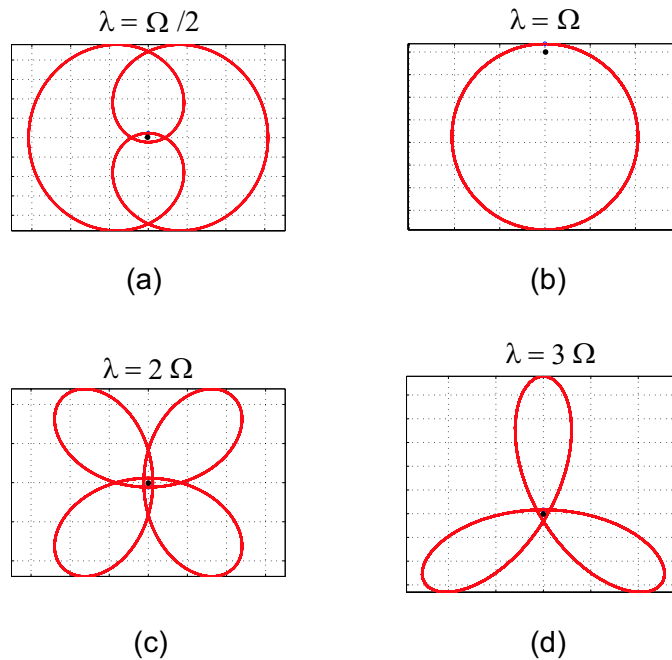


Figure 11.9: Periodic orbits in the inertial frame. Black dot indicates the bearing centerline.

11.4 Concluding remarks

In this chapter we have extended our prestress based formulation to study asynchronous whirl. We have done this for both an axisymmetric and a non-axisymmetric rotor. For the axisymmetric rotor, we found that steady circular whirling solutions exist at all speeds and one can define a natural frequency of the spinning rotor at all speeds. For the non-axisymmetric rotor, synchronous whirling occurs at critical speeds. There is also a region of instability between the two critical speeds. An important finding, not always clearly recognized in the literature, is that a non-axisymmetric rotor in general cannot perform steady circular whirling at speeds other than critical speeds. At a typical speed (not in the instability region) the orbit of the rotor is a complex path as seen in the inertial frame. Periodic solutions, where the orbit of the rotor is closed, can exist at special speeds. A few such periodic solutions were also plotted for the non-axisymmetric example considered.

Chapter 12

Internal viscous damping

In this chapter we extend our formulation to include the effect of internal viscous damping.

12.1 Formulation

The internal damping of rotors is frequently modeled by including a term proportional to the strain rate in the expression for stress. For example, Bolotin [26] uses the following constitutive relation to account for internal damping:

$$\sigma = E \left(\epsilon + C_{iv} \frac{d\epsilon}{dt} \right),$$

where σ is the stress at the point of interest, ϵ is the corresponding strain, E is the Young's modulus and C_{iv} is a damping coefficient. Motivated by this, we will include the effect of damping in our formulation by adding a term proportional to the strain rate in the expression for stress:

$$\mathbf{S} = \lambda \operatorname{tr}(\mathbf{E} + C_{iv} \dot{\mathbf{E}}) \mathbf{I} + 2\mu \left(\mathbf{E} + C_{iv} \dot{\mathbf{E}} \right), \quad (12.1)$$

where

$$\mathbf{E} = \frac{1}{2} (\nabla \mathbf{u} + \nabla \mathbf{u}^T) \quad \text{and} \quad \dot{\mathbf{E}} = \frac{1}{2} (\nabla \dot{\mathbf{u}} + \nabla \dot{\mathbf{u}}^T). \quad (12.2)$$

As is done everywhere in this thesis, we write the displacement of a point on the rotor as

$$\mathbf{u} = \mathbf{u}_0 + a\phi_1 + b\phi_2,$$

where only the modal generalized coordinates a and b are functions of time; the spin-induced deformation \mathbf{u}_0 and non-coplanar mode shapes ϕ_1 and ϕ_2 are functions of position only. Thus

$$\dot{\mathbf{u}} = \dot{a}\phi_1 + \dot{b}\phi_2,$$

where the derivative of the vector is in the rotating frame, for use in Eqs. 12.1 and 12.2. Substituting the above relations into the equilibrium equation (Eq. 4.1) and proceeding as in section 4.3 we get

$$\nabla \cdot \mathbf{S}_0 + (a + C_{iv}\dot{a})\nabla \cdot \mathbf{S}_1 + (b + C_{iv}\dot{b})\nabla \cdot \mathbf{S}_2 + a\nabla \cdot (\nabla\phi_1\mathbf{S}_0) + b\nabla \cdot (\nabla\phi_2\mathbf{S}_0) = \rho\frac{\partial^2\chi}{\partial t^2},$$

where

$$\mathbf{S}_k = \lambda \text{tr}(\mathbf{E}_k)\mathbf{I} + 2\mu\mathbf{E}_k \quad \text{with} \quad \mathbf{E}_k = \frac{1}{2}(\nabla\phi_k + \nabla\phi_k^T) \quad k = 1, 2.$$

Choosing virtual displacements $\delta\mathbf{w}_1 = \delta a_1\phi_1$ and $\delta\mathbf{w}_2 = \delta a_2\phi_2$, virtual work gives

$$\int_V \left(\nabla \cdot \mathbf{S}_0 + (a + C_{iv}\dot{a})\nabla \cdot \mathbf{S}_1 + (b + C_{iv}\dot{b})\nabla \cdot \mathbf{S}_2 + a\nabla \cdot (\nabla\phi_1\mathbf{S}_0) + b\nabla \cdot (\nabla\phi_2\mathbf{S}_0) \right) \cdot \delta\mathbf{w}_k dV = \int_V \rho\frac{\partial^2\chi}{\partial t^2} \cdot \delta\mathbf{w}_k dV, \quad k = 1, 2. \quad (12.3)$$

The acceleration of the point with position vector χ is given by [31]

$$\frac{\partial^2\chi}{\partial t^2} = \frac{d^2a}{dt^2}\phi_1 + \frac{d^2b}{dt^2}\phi_2 + 2\boldsymbol{\Omega} \times \left(\frac{da}{dt}\phi_1 + \frac{db}{dt}\phi_2 \right) + \boldsymbol{\Omega} \times \boldsymbol{\Omega} \times (\mathbf{X} + a\phi_1 + b\phi_2),$$

where \mathbf{X} is the initial position vector of the point, i.e., before deformation.

As discussed in section 5.2,

$$\int_V (\nabla \cdot \mathbf{S}_m) \cdot \phi_n dV = -\rho\omega_m^2 \int_V \phi_m \cdot \phi_n dV = -\rho\omega_m^2 \delta_{mn},$$

where $\delta_{mn} = 1$ if $m = n$ and 0 otherwise. Again the term $\nabla \cdot \mathbf{S}_0$ is balanced by $\rho(\boldsymbol{\Omega} \times \boldsymbol{\Omega} \times \mathbf{X})$ and these terms drop out of the equation.

Substituting the virtual displacements into Eq. 12.3, we get

$$\begin{aligned} & - (a + C_{iv}\dot{a})\omega_1^2 + a \int_V (\nabla \cdot (\nabla\phi_1\mathbf{S}_0)) \cdot \phi_1 dV + b \int_V (\nabla \cdot (\nabla\phi_2\mathbf{S}_0)) \cdot \phi_1 dV \\ & = \ddot{a} + \dot{a}\rho \int_V (2\boldsymbol{\Omega} \times \phi_1) \cdot \phi_1 dV + \dot{b}\rho \int_V (2\boldsymbol{\Omega} \times \phi_2) \cdot \phi_1 dV \\ & \quad + a\rho \int_V (\boldsymbol{\Omega} \times \boldsymbol{\Omega} \times \phi_1) \cdot \phi_1 dV + b\rho \int_V (\boldsymbol{\Omega} \times \boldsymbol{\Omega} \times \phi_2) \cdot \phi_1 dV, \quad (12.4) \end{aligned}$$

and

$$\begin{aligned}
& - (b + C_{iv}\dot{b})\omega_2^2 + a \int_V (\nabla \cdot (\nabla \phi_1 \mathbf{S}_0)) \cdot \phi_2 dV + b \int_V (\nabla \cdot (\nabla \phi_2 \mathbf{S}_0)) \cdot \phi_2 dV = \\
& \quad \ddot{b} + \dot{a}\rho \int_V (2\boldsymbol{\Omega} \times \phi_1) \cdot \phi_2 dV + \dot{b}\rho \int_V (2\boldsymbol{\Omega} \times \phi_2) \cdot \phi_2 dV \\
& \quad + a\rho \int_V (\boldsymbol{\Omega} \times \boldsymbol{\Omega} \times \phi_1) \cdot \phi_2 dV + b\rho \int_V (\boldsymbol{\Omega} \times \boldsymbol{\Omega} \times \phi_2) \cdot \phi_2 dV, \quad (12.5)
\end{aligned}$$

where the dots above a and b denote time derivatives.

These equations, written in matrix notation, appear as

$$\begin{bmatrix} 1 & 0 \\ 0 & 1 \end{bmatrix} \begin{Bmatrix} \ddot{a} \\ \ddot{b} \end{Bmatrix} + \begin{bmatrix} G_{1,1} & G_{1,2} \\ G_{2,1} & G_{2,2} \end{bmatrix} \begin{Bmatrix} \dot{a} \\ \dot{b} \end{Bmatrix} + \begin{bmatrix} K_{1,1} & K_{1,2} \\ K_{2,1} & K_{2,2} \end{bmatrix} \begin{Bmatrix} a \\ b \end{Bmatrix} = 0. \quad (12.6)$$

The above set of equations can be set up as an eigenvalue problem in the rotating coordinate system. Further, we will only consider an axisymmetric geometry for simplicity and greater relevance. We set

$$a = Ae^{\lambda t} \quad \text{and} \quad b = Be^{\lambda t}$$

in Eq. 12.6 and solve for the eigenvalue λ . Since we have damping, the eigenvalue λ will be complex.

12.2 Results for a cylindrical rotor

We again consider the cylinder geometry of chapter 8. The governing equations at any speed Ω for this rotor are

$$\begin{bmatrix} 1 & 0 \\ 0 & 1 \end{bmatrix} \begin{Bmatrix} \ddot{a} \\ \ddot{b} \end{Bmatrix} + \begin{bmatrix} C_{iv}\omega_f^2 & 1.938\Omega \\ -1.938\Omega & C_{iv}\omega_f^2 \end{bmatrix} \begin{Bmatrix} \dot{a} \\ \dot{b} \end{Bmatrix} + \begin{bmatrix} \omega_f^2 - 0.941\Omega^2 & 0 \\ 0 & \omega_f^2 - 0.941\Omega^2 \end{bmatrix} \begin{Bmatrix} a \\ b \end{Bmatrix} = 0,$$

where $\omega_f = 1498.7$ rad/s is the natural frequency of the rotor. We use three different values for C_{iv} : 4×10^{-6} s, 5×10^{-6} s and 6×10^{-6} s. A plot of the imaginary part of the eigenvalue against the spin speed Ω is shown in figure 12.1 (left). Figure 12.1 (right) shows the variation of the real part with Ω . It is seen that the real part of λ is negative

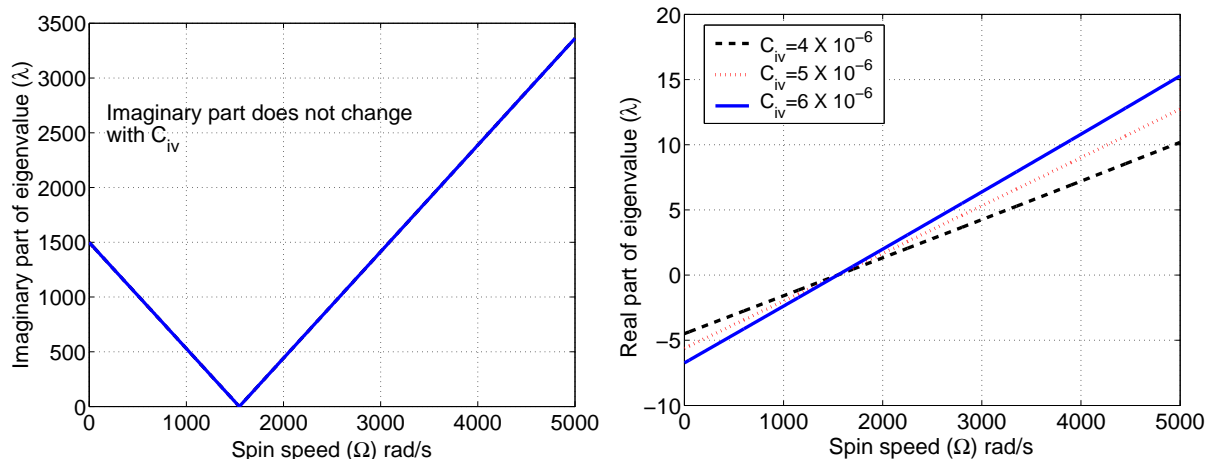


Figure 12.1: Left: plot of imaginary part of λ against spin speed Ω . Right: plot of real part of λ against spin speed Ω .

at speeds below the critical speed (1546.4 rad/s for this geometry) and the rotor is stable at these speeds. At the critical speed the real part is zero. This can be intuitively seen in that, at the critical speed, the shaft performs synchronous whirl and is static when viewed in a rotating frame spinning with the shaft. Hence \dot{a} and \dot{b} are zero and internal viscous damping plays no role at this speed. Beyond the critical speed the real part of λ is positive and the rotor is unstable. In practice, the rotor may be stabilized by *external* damping [40] not included here.

Chapter 13

Conclusions

In this thesis we have approached rotordynamics from a fresh perspective. The central insight of this thesis is that gyroscopic terms used in conventional formulations arise from the spin-induced prestress in the rotor.

With this insight we have developed a new continuum level three dimensional formulation for describing rotordynamics in chapter 4. Two modal projection methods were then developed in chapter 5 as an approximate implementation of our formulation. The first method is non-iterative and involves computation of two volume integrals in addition to the standard modal analysis. The second method is iterative and involves computation of one volume integral in addition to a prestressed modal analysis. The prestress based formulation along with the two modal projection methods form the main contribution of this thesis.

The validity of our formulation was analytically checked with several examples in chapter 6. In this chapter we first used our formulation to solve a few classical buckling problems. In particular, we were able to derive the equation governing buckling of Euler-Bernoulli beams. This approach, while not new to buckling, showed the fundamental similarity between buckling and rotor whirl. Both involve a state of prestress that offers a non-negligible restoring force upon infinitesimal disturbances. We then considered a detailed analytical rotor example from Ewins [25]. The validity of our formulation was established by matching the equations of motion at a general speed. Two more examples were considered: a spinning torque free rigid cylinder and the foreshortening of a rod

rotating like a helicopter blade. Analytical matches with known solutions showed the versatility of our formulation.

A semi-analytical application of our formulation to the problem of a spinning cylinder under axial loads was taken up in chapter 7. There were two key aspects to the study. One, it provided further evidence to the correctness of our formulation. Second, it illustrated the fundamental role played by the assumed kinematics in the virtual work method. The nominal Timoshenko kinematics (without warping) was seen to be unsuitable for use in our formulation. We then resorted to a kinematics obtained from a three dimensional elasticity solution. This kinematics was found to perform very well and a good match was obtained with results from Timoshenko theory, for $L/D \geq 4$.

The real strength of our approach was demonstrated in chapter 8. Here we showed the numerical implementation of our formulation using three dimensional finite element method. Seven different rotor geometries including an asymmetric one were chosen. Three of these were beam-plus-rigid-body models where an analytical solution (procedure described in chapter 6) was available for comparison. One was a cylinder for which analytical answers were available. For the remaining three geometries, two different techniques were used to provide a reliable answer for comparison: a laborious load-stepping method (described in chapter 2) using ANSYS and a direct implementation using our own nonlinear finite element code (described in appendix A using hybrid elements and chapter 9 using isoparametric elements). The comparison showed that the modal projection based approximation of our formulation gave excellent results.

The implementation of our formulation using harmonic elements for axisymmetric rotors was shown in chapter 10. Harmonic elements reduce the dimension of the problem from three to two resulting in large savings in computational time. This offers perhaps the quickest way for accurate computation of critical speeds of arbitrary axisymmetric rotors.

In chapter 11 we used our formulation to study asynchronous whirl. Two examples were considered; a cylinder and a rotor with rectangular cross-section. We showed that steady circular whirling is possible for the cylinder at all speeds. Hence, a Campbell diagram plotting the natural frequency as a function of the spin speed is meaningful. However, it was found that the non-axisymmetric rotor considered cannot execute steady circular whirling at all speeds. In fact the orbit of a typical point on the rotor does not even

close except at some special speeds. It is then not possible to associate a natural frequency with this rotor at a general speed. The rotor can nevertheless execute periodic motion at some special speeds.

Finally, in chapter 12 we used our formulation to study the effect of internal viscous damping. We incorporated this damping by adding a term proportional to the strain rate in the expression for stress. It was found that such damping destabilizes the rotor at all speeds above the critical speed. In practice the rotor may be stabilized by external damping not considered here.

Appendix A

Direct nonlinear finite element analysis

This description of nonlinear finite element analysis of rotors using hybrid elements is taken from [19].

Our direct nonlinear analysis follows the approach and notation of Jog and Kelkar [39]. The strategy for this specific rotor whirl application, as was also discussed in chapter 9, is to write equations in a *rotating* coordinate system; to compute the nonlinear axisymmetric spin-induced deformation solution (in a 3-dimensional setting) as a function of rotation speed; and to identify the particular speed at which infinitesimal displacements (which we expect to be non-axisymmetric from physical intuition) exist which also satisfy the governing equations. In other words, we seek the speed at which the whirling solution bifurcates from the straight solution. We used isoparametric elements in chapter 9; here we use hybrid elements. Note that this formulation retains all terms that were dropped from our formulation in chapter 4.

We now briefly describe the strong form of the governing equations and the two-field variational formulation that is used to derive the finite element equations. All the equations are written with respect to the reference configuration V whose boundary Γ is composed of two open, disjoint regions, $\Gamma = \overline{\Gamma_u} \cup \overline{\Gamma_t}$. The spatial variables in the reference and deformed configurations are denoted by \mathbf{X} and \mathbf{x} , respectively, and within the context of the static problems that we consider in this work, we assume a one-to-one mapping χ

that takes \mathbf{X} to \mathbf{x} , i.e., $\mathbf{x} = \boldsymbol{\chi}(\mathbf{X}) = \mathbf{X} + \mathbf{u}$, where \mathbf{u} is the displacement field. The deformation gradient is given by $\mathbf{F} := \nabla \boldsymbol{\chi} = \mathbf{I} + \nabla \mathbf{u}$, where the gradient is with respect to the material coordinates \mathbf{X} .

We consider the following boundary value problem:

Find the displacements \mathbf{u} , second-Piola Kirchhoff stress \mathbf{S} , Green strain \mathbf{E} and tractions \mathbf{t}^0 , such that

$$\nabla \cdot (\mathbf{F}\mathbf{S}) + \rho_0 \mathbf{b}^0 = \mathbf{0} \quad \text{on } \mathbf{V}, \quad (\text{A.1})$$

$$\mathbf{E} = \hat{\mathbf{E}}(\mathbf{S}) \quad \text{on } V, \quad (\text{A.2})$$

$$\mathbf{E} = \bar{\mathbf{E}}(\mathbf{u}) := \frac{1}{2}[(\nabla \mathbf{u}) + (\nabla \mathbf{u})^T + (\nabla \mathbf{u})^T(\nabla \mathbf{u})] \quad \text{on } V, \quad (\text{A.3})$$

$$\mathbf{t}^0 = \mathbf{F}\mathbf{S}\mathbf{n}^0 \quad \text{on } \Gamma, \quad (\text{A.4})$$

$$\mathbf{t}^0 = \bar{\mathbf{t}}^0, \quad \text{on } \Gamma_t \quad (\text{A.5})$$

$$\mathbf{u} = \mathbf{0}, \quad \text{on } \Gamma_{\mathbf{u}}, \quad (\text{A.6})$$

where $\rho_0 = (\det \mathbf{F})\rho$ is the density in the reference configuration in terms of the density ρ in the deformed configuration, \mathbf{n}^0 is the outward normal to Γ , $\mathbf{t}^0 := \|\mathbf{cof} \mathbf{F}\| \mathbf{t}$ are the tractions defined on the reference configuration in terms of the actual tractions \mathbf{t} on the deformed configuration, and $\mathbf{b}^0(\mathbf{X}) := \mathbf{b}(\boldsymbol{\chi}(\mathbf{X})) = \rho \Omega^2(\tilde{\mathbf{X}} + \tilde{\mathbf{u}})$ is the body force field on the reference configuration, where $\tilde{\mathbf{X}}$ and $\tilde{\mathbf{u}}$ are obtained by excluding the angular velocity direction component from \mathbf{X} and \mathbf{u} , respectively (if the rotor nominally spins about the Z -axis, this means the Z -component of these vectors is set to zero). We emphasize that Eq. (A.2) does not imply that the stress-strain relation $\mathbf{S} = \hat{\mathbf{S}}(\mathbf{E})$ needs to be analytically inverted – numerical inversion is acceptable.

The two field variational principle on which our finite element formulation is based [39] enforces Eqs. (A.1) and (A.5), and Eq. (A.3) in a weak sense. Thus, if

$$\mathcal{V}_u := \{\mathbf{u}_\delta : \mathbf{u}_\delta = \mathbf{0} \quad \text{on } \Gamma_{\mathbf{u}}\}$$

$$\mathcal{V}_S := \{\mathbf{S}_\delta : \mathbf{S}_\delta^T = \mathbf{S}_\delta \quad \text{on } V\}$$

denote the space of variations of the displacements and second Piola-Kirchhoff stress, the two-field variational formulation (after carrying out an appropriate integration by parts of

the first variational statement) is given by

$$\int_V \mathbf{S} : \bar{\mathbf{E}}_\delta dV = \int_V \rho_0 \mathbf{u}_\delta \cdot \mathbf{b}^0 dV + \int_{\Gamma_t} \mathbf{u}_\delta \cdot \mathbf{t}^0 d\Gamma \quad \forall \mathbf{u}_\delta \in \mathcal{V}_u, \quad (\text{A.7})$$

$$\int_V \mathbf{S}_\delta : [\bar{\mathbf{E}}(\mathbf{u}) - \hat{\mathbf{E}}(\mathbf{S})] dV = 0 \quad \forall \mathbf{S}_\delta \in \mathcal{V}_S, \quad (\text{A.8})$$

where $\bar{\mathbf{E}}$ is given by Eq. (A.3), and its variation $\delta \bar{\mathbf{E}}$ is given by

$$\bar{\mathbf{E}}_\delta(\mathbf{u}, \mathbf{u}_\delta) = \frac{1}{2} [(\nabla \mathbf{u}_\delta) + (\nabla \mathbf{u}_\delta)^T + (\nabla \mathbf{u})^T (\nabla \mathbf{u}_\delta) + (\nabla \mathbf{u}_\delta)^T (\nabla \mathbf{u})].$$

To obtain the finite element matrices, we introduce the discretizations

$$\begin{aligned} \mathbf{u} &= \mathbf{N} \hat{\mathbf{u}}, & \mathbf{S}_c &= \mathbf{P} \boldsymbol{\beta}, \\ \mathbf{u}_\delta &= \mathbf{N} \hat{\mathbf{u}}_\delta, & (\mathbf{S}_\delta)_c &= \mathbf{P} \boldsymbol{\beta}_\delta, \\ \mathbf{u}_\Delta &= \mathbf{N} \hat{\mathbf{u}}_\Delta, & (\mathbf{S}_\Delta)_c &= \mathbf{P} \boldsymbol{\beta}_\Delta. \end{aligned}$$

Let the ‘‘strain-displacement’’ matrices \mathbf{B}_L and \mathbf{B}_{NL} , and the stress matrix \mathbf{S}_M be the same as in a conventional (nonlinear) finite element formulation (see, e.g., [41]), and let

$$\begin{aligned} \mathbf{Q} &= \int_V \mathbf{B}_{NL} \mathbf{S}_M^k \mathbf{B}_{NL} dV, \\ \mathbf{A} &= \int_V \mathbf{P}^T \mathbf{B}_L dV, \\ \mathbf{H} &= \int_V \mathbf{P}^T \mathbb{C}_c^{-1} \mathbf{P} dV, \\ \mathbf{f}_1 &= \Omega^2 \int_V \rho_0 \tilde{\mathbf{N}}^T (\tilde{\mathbf{X}} + \tilde{\mathbf{u}}^k) dV + \int_{\Gamma_t} \mathbf{N}^T \mathbf{t}^0 d\Gamma - \int_V \mathbf{B}_L^T \mathbf{S}_c^k dV, \\ \mathbf{f}_2 &= \int_V \mathbf{P}^T [\hat{\mathbf{E}}_c(\mathbf{S}^k) - \bar{\mathbf{E}}_c(\mathbf{u}^k)] dV, \end{aligned} \quad (\text{A.9})$$

where $\tilde{\mathbf{N}}$ is obtained by excluding the shape functions associated with the angular velocity direction from \mathbf{N} . Then the finite element equations are given by

$$(\mathbf{K} - \Omega^2 \mathbf{M}) \hat{\mathbf{u}}_\Delta = \mathbf{f}_\Delta, \quad (\text{A.10})$$

where

$$\begin{aligned} \mathbf{K} &= \mathbf{Q} + \mathbf{A}^T \mathbf{H}^{-1} \mathbf{A}, \\ \mathbf{M} &= \int_V \rho \tilde{\mathbf{N}}^T \tilde{\mathbf{N}} dV, \\ \mathbf{f}_\Delta &= \mathbf{f}_1 + \mathbf{A}^T \mathbf{H}^{-1} \mathbf{f}_2. \end{aligned} \quad (\text{A.11})$$

The critical speed of the rotor is the angular velocity Ω at which the matrix $(\mathbf{K} - \Omega^2 \mathbf{M})$ becomes singular. For actual computation we start with an angular velocity Ω which is slightly less than the natural frequency of the fundamental mode of lateral vibration. Then Ω is increased slowly and the reciprocal of the condition number (RCOND) of the matrix $(\mathbf{K} - \Omega^2 \mathbf{M})$ is monitored. RCOND steadily decreases and then increases again. The spin speed at which it becomes zero is calculated by extrapolation from either side and this speed is the critical speed. Results for the Timoshenko rotor are given below in figure A.1. Two other geometries were also studied, and similar consistency with other results was obtained.

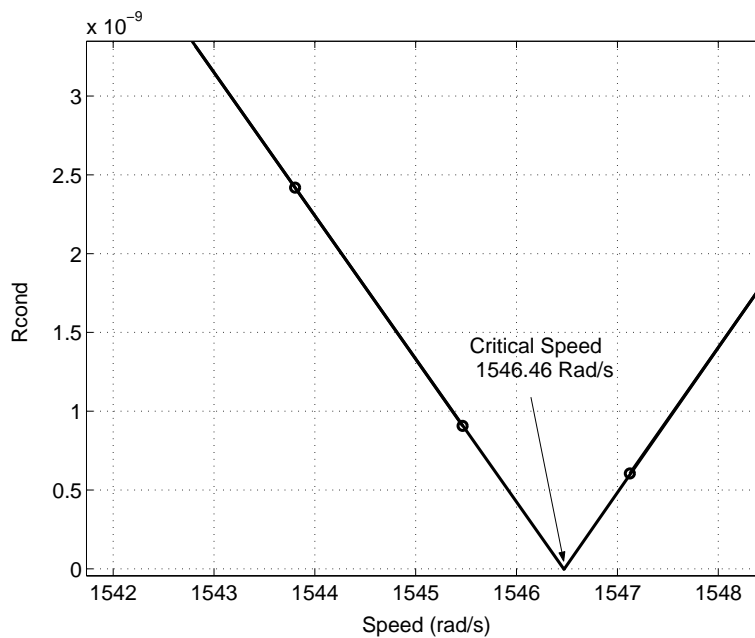


Figure A.1: Zoomed plot of reciprocal of condition number (RCOND) against speed.

Appendix B

Some relevant formulae

B.1 Grad and Div in Cylindrical Coordinates

Let ϕ be a vector with cylindrical components ϕ_r , ϕ_θ and ϕ_z . Then

$$\nabla\phi = \begin{bmatrix} \frac{\partial\phi_r}{\partial r} & \frac{1}{r} \left(\frac{\partial\phi_r}{\partial\theta} - \phi_\theta \right) & \frac{\partial\phi_r}{\partial z} \\ \frac{\partial\phi_\theta}{\partial r} & \frac{1}{r} \left(\frac{\partial\phi_\theta}{\partial\theta} + \phi_r \right) & \frac{\partial\phi_\theta}{\partial z} \\ \frac{\partial\phi_z}{\partial r} & \frac{1}{r} \frac{\partial\phi_z}{\partial\theta} & \frac{\partial\phi_z}{\partial z} \end{bmatrix}.$$

For a second order tensor \mathbf{T} ,

$$\nabla \cdot \mathbf{T} = \left\{ \begin{array}{l} \frac{\partial T_{rr}}{\partial r} + \frac{1}{r} \frac{\partial T_{r\theta}}{\partial\theta} + \frac{T_{rr} - T_{\theta\theta}}{r} + \frac{\partial T_{rz}}{\partial z} \\ \frac{\partial T_{\theta r}}{\partial r} + \frac{1}{r} \frac{\partial T_{\theta\theta}}{\partial\theta} + \frac{T_{r\theta} + T_{\theta r}}{r} + \frac{\partial T_{\theta z}}{\partial z} \\ \frac{\partial T_{zr}}{\partial r} + \frac{1}{r} \frac{\partial T_{z\theta}}{\partial\theta} + \frac{T_{zr}}{r} + \frac{\partial T_{zz}}{\partial z} \end{array} \right\}.$$

B.2 The Function g in Eq. (6.10)

$$g(R, q, E, \theta, r) = \frac{1}{2rAR^3} (40qR^3r \cos(4\theta) - 24qR^3r$$

$$\begin{aligned} & -15 qR^4 \cos(4\theta) + 9 qR^4 - 27 Er^2 AR \cos(4\theta) \\ & + 21 Er^2 AR + 15 Er AR^2 \cos(4\theta) - 9 Er AR^2 \\ & + 20 qR^2 r^2 - 20 qR^2 r^2 \cos(4\theta) - 12 Er^3 A + 12 Er^3 A \cos(4\theta)). \end{aligned}$$

Appendix C

Numerical integration in MATLAB

In this section we describe the details of the numerical integration to evaluate the integrals involved in computing the critical speed.

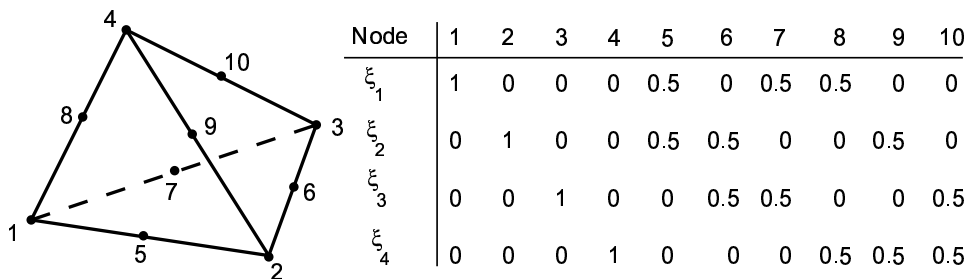


Figure C.1: Ten noded tetrahedral element. ξ_1 , ξ_2 , ξ_3 and ξ_4 are the local volume coordinates.

Figure C.1 shows the 10 noded tetrahedral element. ξ_1 , ξ_2 , ξ_3 and ξ_4 are the local volume coordinates. Only three of these are independent since $\xi_1 + \xi_2 + \xi_3 + \xi_4 = 1$. The shape functions for this element are [34]

$$\begin{aligned}
N_i &= \xi_i (2\xi_i - 1) \quad \text{for } i = 1, 2, 3, 4. \\
N_5 &= 4\xi_1\xi_2 \quad N_6 = 4\xi_2\xi_3 \quad N_7 = 4\xi_3\xi_1 \\
N_8 &= 4\xi_1\xi_4 \quad N_9 = 4\xi_2\xi_4 \quad N_{10} = 4\xi_3\xi_4
\end{aligned}$$

The integrals to be evaluated numerically are of the form

$$\int_V f(u) dV,$$

where the domain V is the volume of the rotor, f is a scalar function of vector u defined on the mapped element whose values at the nodes are known. For a finite element mesh with N_e elements this integral becomes

$$\sum_{k=1}^{N_e} \int_{V_e} f(u) dV_e,$$

where V_e is the volume of the k^{th} element. Using routine isoparametric mapping these integrals are evaluated over the parent element. The integral over the domain V_p of a parent element is

$$\int_{V_p} f(U) J dV_p, \quad (\text{C.1})$$

where J is the determinant of the Jacobian [34] and

$$u = [N]_{3 \times 30} \{U\},$$

where $\{U\}_{30 \times 1}$ is the nodal values of vector u arranged component-wise as

$$\{U\} = \{u_x^1 \ u_y^1 \ u_z^1 \ u_x^2 \ \dots \ u_z^{10}\}.$$

and

$$[N]_{3 \times 30} = \begin{bmatrix} N_1 & 0 & 0 & N_2 & 0 & 0 & \dots & N_{10} & 0 & 0 \\ 0 & N_1 & 0 & 0 & N_2 & 0 & \dots & 0 & N_{10} & 0 \\ 0 & 0 & N_1 & 0 & 0 & N_2 & \dots & 0 & 0 & N_{10} \end{bmatrix}$$

The integration in Eq. C.1 is evaluated numerically using a five point Gauss quadrature scheme (see table C.1 for details). Thus

$$\int_{V_p} f(U) J dV_p = \sum_{k=1}^5 w_k f_k J_k, \quad (\text{C.2})$$

Gauss Pt.	ξ_1	ξ_2	ξ_3	ξ_4	weight
1	$\frac{1}{4}$	$\frac{1}{4}$	$\frac{1}{4}$	$\frac{1}{4}$	$-\frac{4}{30}$
2	$\frac{1}{2}$	$\frac{1}{6}$	$\frac{1}{6}$	$\frac{1}{6}$	$\frac{9}{120}$
3	$\frac{1}{6}$	$\frac{1}{2}$	$\frac{1}{6}$	$\frac{1}{6}$	$\frac{9}{120}$
4	$\frac{1}{6}$	$\frac{1}{6}$	$\frac{1}{2}$	$\frac{1}{6}$	$\frac{9}{120}$
5	$\frac{1}{6}$	$\frac{1}{6}$	$\frac{1}{6}$	$\frac{1}{2}$	$\frac{9}{120}$

Table C.1: Gauss points and weights.

where f_k and J_k are respectively the values of the function f and the Jacobian J at the k^{th} Gauss point. There are two different integrals that are calculated separately in Matlab. The first one is

$$\int_V (\hat{n} \times \hat{n} \times \phi) \cdot \phi dV,$$

where n is the column vector corresponding to the unit vector along the axis of the rotor. Thus for this case the vector function f in Eq. C.1 is

$$f = (\hat{n} \times \hat{n} \times \phi) \cdot \phi.$$

Now

$$\phi = [N]_{3 \times 30} \{\Phi\},$$

where $\{\Phi\}_{30 \times 1}$ is the nodal values of vector ϕ arranged component-wise as

$$\{\Phi\} = \{\phi_x^1 \phi_y^1 \phi_z^1 \phi_x^2 \dots \phi_z^{10}\}.$$

To evaluate the integral, the function f is evaluated at each of the Gauss points and summed using Eq. C.2.

The second integral to be evaluated is

$$\int_V \nabla \phi S_0 : \nabla \phi dV,$$

and hence

$$f = \nabla \phi S_0 : \nabla \phi = \text{tr} (S_0 \nabla \phi^T \nabla \phi).$$

Also

$$S_0 = \lambda \text{tr} \left(\frac{\nabla u_0 + \nabla u_0^T}{2} \right) I + 2\mu \left(\frac{\nabla u_0 + \nabla u_0^T}{2} \right).$$

The integral can be evaluated once $\nabla\phi$ and ∇u_0 are known. The procedure for evaluating $\nabla\phi$ and ∇u_0 is identical. We will illustrate it for $\nabla\phi$. Now

$$\nabla\phi = \begin{bmatrix} \frac{\partial\phi_x}{\partial x} & \frac{\partial\phi_x}{\partial y} & \frac{\partial\phi_x}{\partial z} \\ \frac{\partial\phi_y}{\partial x} & \frac{\partial\phi_y}{\partial y} & \frac{\partial\phi_y}{\partial z} \\ \frac{\partial\phi_z}{\partial x} & \frac{\partial\phi_z}{\partial y} & \frac{\partial\phi_z}{\partial z} \end{bmatrix}, \quad \text{where } \phi_x, \phi_y \text{ and } \phi_z \text{ are components of } \phi.$$

Again, the procedure for evaluation of each of the entries of the above matrix is similar. We evaluate $\frac{\partial\phi_x}{\partial x}$:

$$\frac{\partial\phi_x}{\partial x} = \frac{\partial}{\partial x} \sum_{k=1}^{10} N_k \phi_x^k = \sum_{k=1}^{10} \frac{\partial N_k}{\partial x} \phi_x^k = \sum_{k=1}^{10} \sum_{j=1}^3 \frac{\partial N_k}{\partial \xi_j} \frac{\partial \xi_j}{\partial x} \phi_x^k,$$

where ϕ_x^k is the value of ϕ_x at node k and the summation over j runs only till 3 since ξ_4 is not independent and can be expressed in terms of ξ_1, ξ_2 and ξ_3 . The above double summation can be easily evaluated at Gauss point locations. Once each component of $\nabla\phi$ and ∇u_0 is known, the integral is easily evaluated using Eq. C.2.

Appendix D

Circular motion of non-axisymmetric rotors

It was stated in chapter 11 that it is not possible for a general non-axisymmetric rotor to perform steady circular whirling at a non-critical speed. We now prove it for the rectangular cross-sectioned rotor considered in section 11.3. The governing equations for this rotor at a speed Ω are (correct to 2 decimal places)

$$\begin{bmatrix} 1 & 0 \\ 0 & 1 \end{bmatrix} \begin{Bmatrix} \ddot{a} \\ \ddot{b} \end{Bmatrix} + \begin{bmatrix} 0 & -1.96\Omega \\ 1.96\Omega & 0 \end{bmatrix} \begin{Bmatrix} \dot{a} \\ \dot{b} \end{Bmatrix} + \begin{bmatrix} \omega_{f1}^2 - 1.00\Omega^2 & 0 \\ 0 & \omega_{f2}^2 - 0.93\Omega^2 \end{bmatrix} \begin{Bmatrix} a \\ b \end{Bmatrix} = 0. \quad (\text{D.1})$$

For the rotor to perform steady circular whirling (circular motion in the inertial frame) it should follow a circular path when viewed in the rotating frame as well. For the non-axisymmetric rotor considered, with eigenvalues $\lambda_1, \bar{\lambda}_1, \lambda_2, \bar{\lambda}_2$, $|\lambda_1| \neq |\lambda_2|$ and hence any motion obtained as a combination of eigenvectors corresponding to λ_1 and λ_2 will not be circular. It remains to check if the motion involving one pair (say, λ_1 and $\bar{\lambda}_1$) can be circular. The eigenvalues of the system represented by Eq. D.1 can be verified to be purely imaginary at all speeds outside the instability region. So we take $\lambda_1 = i\lambda$. The eigenvectors corresponding to $i\lambda$ and $-i\lambda$ at any speed are then of the form (see, e.g., [42])

$$e_1 = \begin{Bmatrix} iG \\ H \end{Bmatrix} \quad \text{and} \quad e_2 = \begin{Bmatrix} -iG \\ H \end{Bmatrix},$$

for some real values of G and H . A general real solution for the modal coordinates can then be written as

$$\begin{Bmatrix} a \\ b \end{Bmatrix} = (\alpha + i\beta)e^{i\lambda t} \begin{Bmatrix} iG \\ H \end{Bmatrix} + (\alpha - i\beta)e^{-i\lambda t} \begin{Bmatrix} -iG \\ H \end{Bmatrix},$$

for some real α and β . We can choose the phase such that $\beta = 0$. Using this and Eq. 11.10, the position of a typical point P on the centerline of the rotor can be calculated as (assuming the reference position of P to be (0, 0))

$$\begin{aligned} x_R &= -2G\alpha \sin(\lambda t)\phi_{1,P}^x + 2H\alpha \cos(\lambda t)\phi_{2,P}^x, \\ y_R &= -2G\alpha \sin(\lambda t)\phi_{1,P}^y + 2H\alpha \cos(\lambda t)\phi_{2,P}^y. \end{aligned}$$

We note that for the rectangular cross-sectioned rotor considered, the mass-normalized mode shapes are physically orthogonal to one another. Thus

$$\phi_{1,P}^x \phi_{2,P}^x + \phi_{1,P}^y \phi_{2,P}^y = 0. \quad (\text{D.2})$$

Also, we can choose a coordinate system where $\phi_{2,P}^x = 0$. This with Eq. D.2 implies $\phi_{1,P}^y = 0$.

Now if the path of P is to be a circle of some constant radius R , we have

$$x_R^2 + y_R^2 = R^2.$$

On combining trigonometric terms, the above becomes an equation involving $\sin 2\lambda t$ and $\cos 2\lambda t$. Since the equation is true for all t , we get two equations by setting the coefficient of $\sin 2\lambda t$ and $\cos 2\lambda t$ to zero. The first equation is just the orthogonality condition Eq. D.2. The second equation is

$$\alpha^2(G\phi_{1,P}^x - H\phi_{2,P}^y)(G\phi_{1,P}^x + H\phi_{2,P}^y) = 0. \quad (\text{D.3})$$

For a general rotor (including the rectangular cross-sectioned rotor considered) neither $G\phi_{1,P}^x - H\phi_{2,P}^y = 0$ nor $G\phi_{1,P}^x + H\phi_{2,P}^y = 0$. The only possibility is

$$\alpha = 0,$$

which means that $x_R \equiv y_R \equiv 0$ for all t . The rotor cannot perform steady circular whirling in a circle of nonzero radius at a non-critical speed outside the instability region. For speeds

in the instability region the rotor orbit spirals out, again precluding circular orbits. Thus, barring rotor geometries for which Eq. D.3 is satisfied (e.g., a square cross-sectioned rotor) there are in general no purely circular orbits.

For an axisymmetric rotor, on the other hand, the chosen mass-normalized modes have a further property due to symmetry:

$$\phi_{1,P}^x = \phi_{2,P}^y \quad \text{and} \quad \phi_{1,P}^y = -\phi_{2,P}^x.$$

Also the eigenvectors are such that $G = \pm H$. Using the above relations, Eq. D.3 is identically zero for any α . Thus steady circular whirling exists at all speeds for an axisymmetric rotor.

It is emphasized that, since steady circular whirling does not exist for a general non-axisymmetric rotor, one cannot define a ‘natural frequency’ for these rotors at non-critical speeds. This constitutes a fundamental difference between axisymmetric and non-axisymmetric rotors.

References

- [1] Swanson E., Powell C. D., and Weissman S. A practical review of rotating machinery critical speeds and modes. *Shock and Vibration*, May 2005.
- [2] Cowper G. R. The shear coefficient in Timoshenko's beam theory. *Journal of Applied Mechanics*, 33:335–340, 1966.
- [3] Nelson F. C. A brief history of early rotor dynamics. *Sound and Vibration*, June 2003.
- [4] Nelson H. D. Rotordynamic modeling and analysis procedures: a review. *JSME International Journal C*, 41:1–12, 1998.
- [5] Prohl M. A. A general method for calculating critical speeds of flexible rotors. *ASME Journal of Applied Mechanics*, 12:A142–A148, 1945.
- [6] Flack R. D. and Rooke J. H. A theoretical-experimental comparison of the synchronous response of a bowed rotor in five different sets of fluid film bearings. *Journal of Sound and Vibration*, 73:505–517, 1980.
- [7] Sakate M., Endo M., Kishimoto K., and Hayashi N. Secondary critical speed of flexible rotors with inertia slots. *Journal of Sound and Vibration*, 87:61–70, 1983.
- [8] Hsieh S., Chen J., and Lee A. A modified transfer matrix method for the coupling lateral and torsional vibrations of symmetric rotor-bearing systems. *Journal of Sound and Vibration*, 289:294–333, 2006.
- [9] Rouch K. E. and Kao J. S. A tapered beam finite element for rotor dynamics analysis. *Journal of Sound and Vibration*, 66:119–140, 1979.

-
- [10] Nelson H. D. A finite rotating shaft element using Timoshenko beam theory. *ASME Journal of Mechanical Design*, 102:793–803, 1980.
- [11] Greenhill L. M., Bickford W. B., and Nelson H. D. A conical beam finite element for rotor dynamics analysis. *ASME Journal of Vibration, Acoustics, Stress and Reliability in Design*, 107:421–430, 1985.
- [12] Genta G. Consistent matrices in rotor dynamics. *Meccanica*, 20:235–248, 1985.
- [13] Genta G. and Gugliotta A. A conical element for finite element rotor dynamics. *Journal of Sound and Vibration*, 120:175–182, 1988.
- [14] Edney S. L., Fox C. H. J., and Williams E. J. Tapered Timoshenko finite elements for rotor dynamics analysis. *Journal of Sound and Vibration*, 137:463–481, 1990.
- [15] Gmür T. C. and Rodrigues J. D. Shaft finite elements for rotor dynamics analysis. *ASME Journal of Vibration and Acoustics*, 113:482–493, 1991.
- [16] Genta G. *Dynamics of Rotating Systems*. Springer, New York, 2005.
- [17] Stephenson R. W. and Rouch K. E. Modelling rotating shaft using axisymmetric solid finite elements with reduction. *ASME Journal of Vibration and Acoustics*, 115:484–489, 1993.
- [18] Nandi A. and Neogy S. Modelling of rotors with three-dimensional solid finite elements. *Journal of Strain Analysis*, 36(4):359–371, 2001.
- [19] Mahadevan P., Jog C. S., and Chatterjee A. Modal projections for synchronous rotor whirl. *Proceedings of the Royal Society London Series A.*, 464:1739–1760, 2008.
- [20] Mahadevan P. and Chatterjee A. Some classical buckling problems revisited from a continuum approach. *13th National Conference on Mechanisms and Machines (NaCoMM07)*, 2007.
- [21] Timoshenko S. and Young D. H. *Elements of Strength of Materials*. Van Nostrand Co, New Delhi, 1935.
- [22] Choi S. H., Pierre C., and Ulsoy A. G. Consistent modelling of rotating Timoshenko shafts subject to axial loads. *ASME Journal of Vibration and Acoustics*, 114:249–259, 1992.

- [23] Gurtin M. E. *An Introduction to Continuum Mechanics*. Academic Press, San Diego, 1981.
- [24] Jog C. S. *Foundations and Applications of Mechanics Vol. I: Continuum Mechanics*. Narosa Publishing House, New Delhi, 2002.
- [25] Ewins D. J. *Modal Testing: Theory, Practice and Application*. Research Studies Press, Baldock, 2000.
- [26] Bolotin V. V. *Nonconservative problems of the theory of elastic stability*. Pergamon press, London, 1963.
- [27] Stephenson R. W. and Rouch K. E. Modelling of rotors with axisymmetric solid harmonic elements. *Journal of Sound and Vibration*, 131:431–443, 1989.
- [28] Timoshenko S. P. and Gere J. M. *Theory of Elastic Stability*. McGraw-Hill, New York, 1961.
- [29] Den Hartog J. P. *Advanced Strength of Materials*. Dover publications, New York, 1952.
- [30] Timoshenko S. P. and Goodier J. N. *Theory of Elasticity*. McGraw-Hill, Singapore, 1970.
- [31] Shames I. H. *Engineering Mechanics: statics and dynamics*. Prentice-Hall, New Delhi, 1963.
- [32] H. Goldstein. *Classical Mechanics*. Addison-Wesley, California, 1950.
- [33] Basu-Mandal P., Chatterjee A., and Papadopoulos J. M. Hands-free circular motions of a benchmark bicycle. *Proceedings of the Royal Society A*, 463:1983–2003, 2007.
- [34] Cook D. R., Malkus D. S., and Plesha M. E. *Concepts and Applications of Finite Element Analysis*. John Wiley & Sons, Singapore, 1989.
- [35] Hodges D. H. An approximate formula for the fundamental frequency of a uniform rotating beam clamped off the axis of rotation. *Journal of Sound and Vibration*, 77: 11–18, 1981.
- [36] Mahadevan P. and Chatterjee A. Axially loaded Timoshenko rotors from a prestressed continuum approach. *Proceedings of the 9th biennial ASME conference on engineering system design and analysis*, 2008.

-
- [37] Sokolnikoff I. S. *Mathematical theory of elasticity*. Tata McGraw-Hill, New Delhi, 1971.
- [38] Zu Jean Wu-Zheng and Han Ray P. S. Natural frequencies and normal modes of a spinning Timoshenko beam with general boundary conditions. *Journal of Applied Mechanics*, 59:S197–S204, 1992.
- [39] Jog C. S. and Kelkar P. Non-linear analysis of structures using high performance hybrid elements. *International Journal for Numerical Methods in Engineering*, 68: 473–501, 2006.
- [40] Dimentberg F. M. *Flexural Vibrations of Rotating Shafts*. Butterworths, London, 1961.
- [41] Bathe K. J. *Finite Element Procedures*. Prentice-Hall, Englewood Cliffs, 1995.
- [42] Wang W. and Kirkhope J. New eigensolutions and modal analysis for gyroscopic/rotor systems, part1: undamped systems. *Journal of Sound and Vibration*, 175:159–170, 1994.